

Fundamental understanding of cobalt Fischer-Tropsch synthesis catalyst deactivation

Citation for published version (APA):

Kistamurthy, D. (2015). *Fundamental understanding of cobalt Fischer-Tropsch synthesis catalyst deactivation*. [Phd Thesis 1 (Research TU/e / Graduation TU/e), Chemical Engineering and Chemistry]. Technische Universiteit Eindhoven.

Document status and date:

Published: 01/01/2015

Document Version:

Publisher's PDF, also known as Version of Record (includes final page, issue and volume numbers)

Please check the document version of this publication:

- A submitted manuscript is the version of the article upon submission and before peer-review. There can be important differences between the submitted version and the official published version of record. People interested in the research are advised to contact the author for the final version of the publication, or visit the DOI to the publisher's website.
- The final author version and the galley proof are versions of the publication after peer review.
- The final published version features the final layout of the paper including the volume, issue and page numbers.

[Link to publication](#)

General rights

Copyright and moral rights for the publications made accessible in the public portal are retained by the authors and/or other copyright owners and it is a condition of accessing publications that users recognise and abide by the legal requirements associated with these rights.

- Users may download and print one copy of any publication from the public portal for the purpose of private study or research.
- You may not further distribute the material or use it for any profit-making activity or commercial gain
- You may freely distribute the URL identifying the publication in the public portal.

If the publication is distributed under the terms of Article 25fa of the Dutch Copyright Act, indicated by the "Taverne" license above, please follow below link for the End User Agreement:

www.tue.nl/taverne

Take down policy

If you believe that this document breaches copyright please contact us at:

openaccess@tue.nl

providing details and we will investigate your claim.

Fundamental understanding of cobalt Fischer-Tropsch synthesis catalyst deactivation

PROEFSCHRIFT

ter verkrijging van de graad van doctor aan de Technische
Universiteit Eindhoven, op gezag van de rector magnificus
prof.dr.ir. F.P.T. Baaijens, voor een commissie
aangewezen door het College voor Promoties, in het
openbaar te verdedigen op dinsdag 2 juni 2015
om 16:00 uur

door

Deshen Kistamurthy

geboren te Durban, Zuid-Afrika

Dit proefschrift is goedgekeurd door de promotor en de samenstelling van de promotiecommissie is als volgt:

Voorzitter: prof.dr.ir. J.C. Schouten
Promotor: prof.dr. J.W. Niemantsverdriet
Copromotor: dr. C.J. Weststrate
Leden: prof.dr. A.K. Datye (University of New Mexico)
prof.dr. A.O.I. Krause (Aalto University)
prof.dr.ir. E.J.M. Hensen
Adviseur: dr. J. van de Loosdrecht (Sasol Technology)

Fundamental understanding of cobalt Fischer-Tropsch synthesis catalyst deactivation

Deshen Kistamurthy

Eindhoven University of Technology, The Netherlands, 2015

Copyright © 2015

The research described in this thesis was carried out in the Laboratory for Physical Chemistry of Surfaces, Eindhoven University of Technology, The Netherlands. Financial support was provided by Sasol Technology (Pty) Ltd., South Africa.

A catalogue record is available from the Eindhoven University of Technology Library. ISBN: 978-90-386-3853-9

Cover design: Paul Verspaget and Deshen Kistamurthy

Printed by: Gildeprint Drukkerijen, Enschede

Cover photograph: courtesy of Sasol Limited.

Table of contents

Chapters

1.	Introduction and scope	1
2.	Experimental techniques and methods	19
3.	Ostwald ripening on a planar Co/SiO ₂ catalyst exposed to model Fischer-Tropsch synthesis conditions	47
4.	The role of carboxylic acids in cobalt Fischer-Tropsch synthesis catalyst deactivation	95
5.	Acetic acid adsorption on γ -Al ₂ O ₃ (110) & (100) surfaces: A Density Functional Theory & Infrared Spectroscopy study	153
6.	Conclusions and outlook	187
	Summary	208
	Acknowledgements	214
	List of publications	216
	Curriculum vitae	218

1

Introduction and scope

1.1. Fischer-Tropsch synthesis

The term Fischer-Tropsch synthesis (FTS) describes the process that can be used to transform synthesis gas, a mixture of CO and H₂, into longer hydrocarbon chains. The process was named after Franz Fischer and Hans Tropsch, who showed in the early 1920s that a mixture of H₂ and CO gas can be converted to higher hydrocarbons to provide petrol or diesel [1,2]. Fischer and Tropsch showed that these fuels could be produced over iron and cobalt catalysts at relatively low temperatures and pressures [3]. Their discovery was timely since Germany and Japan used the synthetic fuel during the Second World War.

FTS plants were first commercialized in 1936 in Germany and then later through 1940 to 1960 in Japan and China, which utilized mainly Co catalysts [4]. Later, toward the 1950s, a few relatively small plants were constructed in the U.S, but were later shut down [5]. South Africa was in need of its own supply of liquid fuel and this led to large-scale operation of FTS around 1955 [6].

Today, there are a number of operating FTS plants across the world (Table 1.1) [7]. Sasol is involved in large-scale applications of FTS, including two FTS plants in South Africa which have a combined capacity of ~165 000 barrels per day (1 barrel petroleum is ~159 liters) and the ORYX GTL plant in Qatar which is a joint venture between Qatar Petroleum and Sasol (Figure 1.1). The ORYX GTL plant has a capacity of ~34 000 barrels per day. Shell is also involved in large-scale FTS plants, one located in Qatar with a capacity of ~140 000 barrels per day and another located in Malaysia producing ~14 500 barrels per day [7].

Table 1.1: Fischer-Tropsch synthesis large-scale commercial plants [7].

Company	Location	Carbon feedstock	Catalyst utilized	Capacity (~barrels per day)
Sasol	Sasolburg, South Africa	Natural gas	Fe/K	5000
	Secunda, South Africa	Coal & natural gas	Fe/K	160 000
ORYX GTL	Ras Laffan, Qatar	Natural gas	Co/Al ₂ O ₃	34 000
EGTL*	Escravos, Nigeria	Natural gas	Co/Al ₂ O ₃	34 000
Shell	Bintulu, Malaysia	Natural gas	Co/SiO ₂ , Co/TiO ₂	14 500
Shell	Ras Laffan, Qatar	Natural gas	Co/TiO ₂	140 000
PetroSA	Mosselbay, South Africa	Natural gas	Fe/K	22 000

*EGTL is a collaboration between Chevron, the Nigerian National Petroleum Corporation and Sasol.



Figure 1.1: ORYX GTL plant in Qatar, a joint venture between Qatar Petroleum and Sasol. Adapted from Ref [8].

Chapter 1

FTS plants are expensive to build, start-up and maintain, however they can also be very profitable. ORYX GTL was built at a cost of \$1 billion, while a yearly profit can be around \$500 million [9]. The Shell FTS plant in Qatar cost \$20 billion to build and yearly profit can reach \$4 billion [10].

The feedstock for FTS is synthesis gas, a gaseous mixture of H_2 and CO . The carbon resource converted to synthesis gas can be coal, natural gas or biomass. The overall processes to fuels are called ‘coal-to-liquids’ (CTL), ‘gas-to-liquids’ (GTL) or ‘biomass-to-liquids’ (BTL). The conversion to syngas can be achieved by gasification for solid feedstocks or by autothermal reforming in the case of natural gas. Figure 1.2 shows a schematic representation of the GTL process employed by Sasol, the Sasol slurry phase distillate™ process.

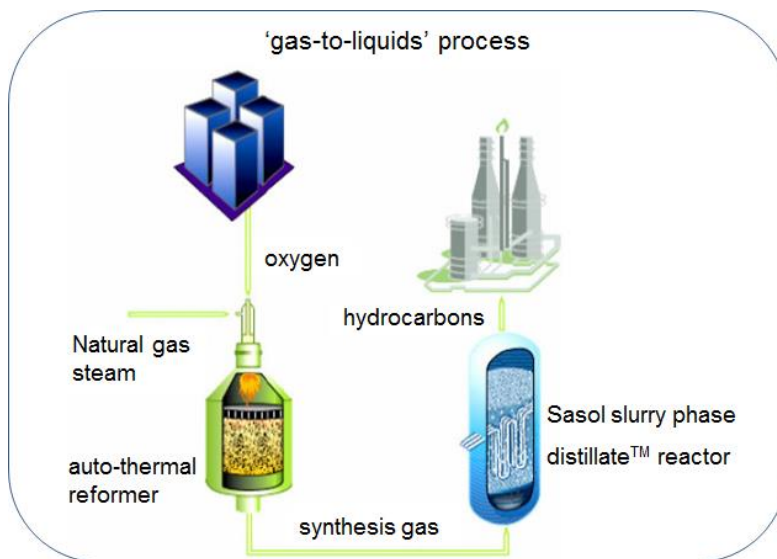
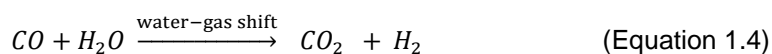
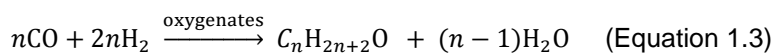
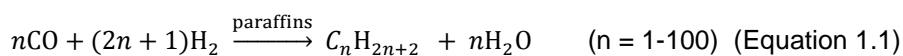


Figure 1.2: Schematic representation of the process steps in the Sasol slurry phase distillate™ process. Adapted from Ref [11].

FTS reactors are typically two or three-phase and either moving or stationary bed reactors [12-14]. Both slurry and fixed bed reactors are currently in use in commercial processes. High-temperature FTS (~320-350°C) produces gasoline and a number of valuable chemicals including ethylene, propylene, 1-hexene, 1-octene and valuable solvents [15]. Low-temperature FTS (200-250°C) produces mainly waxes and some lighter hydrocarbons. In addition to liquid petroleum gas and naphtha that is derived from the low-temperature process, downstream hydrocracking of waxes produces high-quality diesel.

1.2. Cobalt-catalysed Fischer-Tropsch synthesis

The chemistry of FTS is complex, however a few generalized reactions can describe (i) the main reactions of paraffin and olefin formation (Equations 1.1 & 1.2), (ii) the side reactions for oxygenate (e.g. alcohols and acids) formation (Equation 1.3) and (iii) the water-gas shift reaction (Equation 1.4) [16]. Cobalt, iron, ruthenium and nickel can all be used as catalysts in the FTS reaction [17]. Ruthenium is rare and relatively expensive, while nickel favors methanation and poses the problem of nickel-carbonyl formation. Current commercial FTS applications typically employ iron or cobalt-based FTS catalysts.



Chapter 1

Cobalt is the preferred metal for GTL application because the usage ratio is comparable to the H_2/CO ratio derived from natural gas (value of ~ 2). Co has a low propensity for the water-gas shift reaction [1,2], therefore, the usage ratio is determined mostly by the main FTS reactions. The usage ratio is important for the gas loop design in an FTS process, making cobalt the preferred metal of choice in a process with a natural gas feed.

Cobalt catalysts are currently employed in the large-scale GTL plants such as ORYX GTL in Qatar (Co/ Al_2O_3 catalyst) and by Shell in both the Qatar and Malaysia plants (Co/ TiO_2) (Table 1.1). The cobalt FTS catalyst typically consists of the active metal (often 10-30 wt%) and an oxidic support. Often, the catalyst contains promoters that aid structural integrity (e.g. Zr or Si) (1-10 wt%) and reduction (e.g. Pt or Ru) (0.05-0.1wt%) of the cobalt to the active metallic state [7].

The support is an integral component of the FTS catalyst. The support provides the surface onto which the active metal is dispersed. In order to keep costs of catalyst production low, the expensive metal must be used efficiently. This can be achieved by using a high surface area support, which allows a high and stable dispersion of the active metal, thereby maximizing the ratio of active surface to volume used. Therefore, the support provides a means to keep the nanoparticles of the active phase separate and prevent metal agglomeration (which causes a loss of metal surface area). The support morphology as well as its physical and chemical properties are critical to achieve the desired metal loading and optimum crystallite size. Under FTS conditions, the support must have sufficient hydrothermal stability to withstand several bars of high-pressure steam, which is an important requirement when using either fixed bed or slurry

reactors. In addition, sufficient attrition resistance is required to withstand catalyst break-up or fines generation during FTS in a slurry reactor. The attrition resistance of Co FTS catalyst support follows the order $\text{Co}/\text{Al}_2\text{O}_3 > \text{Co}/\text{SiO}_2 > \text{Co}/\text{TiO}_2$ [18].

1.3. Deactivation of Co-based Fischer-Tropsch synthesis catalysts

Cobalt is active for FTS in the metallic state [19] and, as is the challenge with many catalysts, deactivates with time. Stable catalyst performance is vital to the economics of a GTL process, making catalyst deactivation an important research topic in industrial catalyst development. Figure 1.3 illustrates the typical behavior of a $\text{Co}/\text{Pt}/\text{Al}_2\text{O}_3$ catalyst during FTS. In this example, FTS activity was tested for an extended period under realistic conditions (230°C, 20 bar H_2/CO) in a slurry bubble column reactor at fixed CO conversion using a clean synthesis gas feed (Figure 1.3) [20]. The catalyst demonstrated a loss of ~40% activity within the initial 40 days of FTS. The factors that contribute to Co FTS catalyst deactivation have been extensively reviewed in the literature [20,21]. The following deactivation mechanisms have been postulated [22]:

- (i) poisoning by sulphur and/or nitrogen compounds
- (ii) oxidation of the active cobalt metal
- (iii) cobalt-support compound formation
- (iv) surface reconstruction
- (v) sintering of cobalt crystallites
- (vi) carbon formation

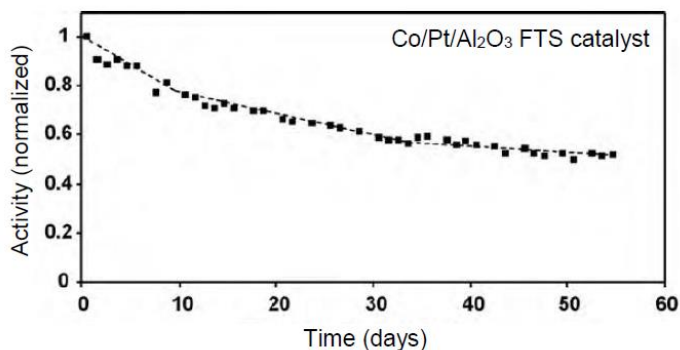


Figure 1.3: Normalized activity for a Co/Pt/Al₂O₃ catalyst during realistic FTS in a 100-barrel/day slurry bubble column reactor (230°C, 20 bar, H₂ + CO conversion of 50-70%, feed gas composition of 50-60 vol.% H₂ and 30-40 vol.% CO). Adapted from Saib *et al.* [20].

1.3.1. Poisoning by sulphur and/or nitrogen compounds

Poisoning is well known to be an issue for Co FTS catalysts, especially in reactions using coal as a feedstock [20]. Poisons can block the metal sites active for FTS and consequently contribute to catalyst deactivation. Synthesis gas feeds containing sulphur are a problem because sulphur compounds are strongly absorbed and are difficult to remove [20,23,24]. In fact, even low levels of sulphur (20 ppbv) in the gas feed have been shown to impact FTS activity [25]. One method to prevent this is the cleaning of the synthesis gas feed using guard beds. Nitrogen compounds have also been identified as poisons [26,27], albeit with relatively less impact compared to sulphur, and the poisoning can be reversed using a mild hydrogen treatment.

1.3.2. Oxidation of the active cobalt metal

Co is active for FTS in its metallic form [19]. Therefore, oxidation of the active metal to inactive oxidic forms can contribute to catalyst deactivation. Water is always present in FTS because adsorbed oxygen, formed *via* CO dissociation on the metal surface, is removed primarily by hydrogen (in the case of Co catalysts). The water partial pressure created depends on the reactor, catalyst and operating conditions [28]. FTS using a Co/Pt/Al₂O₃ catalyst in a slurry bubble column reactor operated at 230°C, 20 bar, H₂ + CO conversion of 50-70% and feed gas composition of 50-60 vol.% H₂ and 30-40 vol.% CO results in ~4-6 bar of water partial pressure [29].

To test the hypothesis of oxidation during FTS, x-ray absorption near edge spectroscopy (XANES) measurements were carried out on a series of spent Co FTS catalysts (fresh crystallite size ~6nm) [29] as well as a series of reference compounds. No surface or bulk oxidation was detected. In fact, the calculated amount of metal in the spent samples was found to increase with time on line. In addition, thermodynamic calculations excluded the formation of bulk cobalt oxides for the typical Co particle sizes on the catalyst tested [30]. The findings indicated that the FTS reaction environment was more reducing than oxidizing. Furthermore, a model catalyst approach, using Co crystallites (4-5 nm) on a SiO₂/Si(100) substrate, was utilized to study cobalt surface oxidation [31]. *In-situ* near edge x-ray absorption fine structure (NEXAFS) showed that surface oxidation did not occur at model FTS conditions (0.4 mbar, PH₂O/PH₂: 1, 150–400°C). After reconciliation of thermodynamic calculations and experimental evidence, it was deduced that surface oxidation was not a

deactivation mechanism of Co FT catalysts for crystallites larger than 2nm [20,32-34].

1.3.3. Cobalt-support compound formation

The formation of metal-support compounds has been considered as a catalyst deactivation mechanism [35,36]. Metal-support compounds can form at the expense of active cobalt metal during FTS and consequently contribute to catalyst deactivation.

Moodley *et al.* investigated the formation of cobalt-aluminate compounds during extended FTS runs [37]. XANES analyses on a series of spent Co FTS catalysts showed that the FTS environment is more reducing than oxidizing which implied that any cobalt-aluminate compounds formed must be due to unreduced cobalt in the fresh catalyst interacting with the support. XANES showed that upon increasing the water partial pressure (from 4.5 to 10 bar) the quantity of CoAl_2O_4 increased and this occurred at the expense of CoO [37]. TPR-MS showed a high temperature peak which provided further evidence that a hard-to-reduce species (indicative of CoAl_2O_4) is produced during FTS at high water partial pressure (i.e. 10 bar). The findings led to the conclusion that cobalt-aluminate formation is not significant at typical Co FTS conditions [37]. The small amounts of cobalt-aluminates formed during FTS were postulated to be formed from unreduced CoO particles (2-3 nm) in the fresh catalyst. As these small oxidic particles do not contribute to FTS, their loss is not expected to impact FTS performance.

1.3.4. Surface reconstruction

Reconstruction refers to the thermodynamic process where relatively more stable surfaces are formed with a structure that is different from the bulk-terminated surface structure. Direct observations of surface reconstruction on the industrial catalyst under working conditions is not possible with techniques currently available, thus theoretical or surface science studies are required to obtain fundamental understanding. Reconstruction can cause a change in atomic configuration of the active metal site and change the shape of the cobalt particle, resulting in deactivation [38,43]. However, changes to the shape of the cobalt particle can also result in formation of active metal sites, therefore at this point in time it remains unclear whether (i) surface reconstruction indeed happens under realistic FTS conditions and (ii) whether it is activating or deactivating the FTS catalyst.

Ciobîcă *et al.* showed using theoretical calculations that both fcc-Co(100) and fcc-Co(111) surfaces, the most abundant surfaces on an ideal fcc particle, undergo a clock-type reconstruction when atomic carbon is adsorbed [39]. This carbon-induced reconstruction was also observed experimentally on a Co(0001) surface [40]. However, the carbon coverage required for this reconstruction (0.5 ML) is deduced not to be reached during FTS [41], since cobalt carbide formation is negligible [42] and hydrogen is available on the metal surface. Wilson *et al.* observed that an initially flat, close-packed Co surface undergoes significant roughening under synthesis gas treatment (4 bar H₂/CO:2/1 at 250°C) and envisaged that mobile cobalt subcarbonyls can be pinned down by surface carbon [43]. Weststrate *et al.* deduced from theoretical calculations and surface science experiments, that surface roughening under FTS conditions could

indeed be induced by a combination of molecular CO and carbon [41]. CO induces surface atom mobility at FTS temperature, while atomic carbon adsorbs on the surface and provides the thermodynamic driving force for roughening. The mobile cobalt species are pinned down by the surface carbon (if present in significant amounts) and defects in graphitic carbon (if present), causing surface roughness.

1.3.5. Sintering of cobalt crystallites

Sintering, in the context of heterogeneous catalysis, is generally referred to as (thermally induced) catalyst deactivation caused by a loss of active metal surface area [44]. The loss of catalyst active surface area is a result of loss and/or growth of the nanoparticles into which the active metal phase is dispersed. The thermodynamic driving force for the process originates from the higher chemical potential of the metal atoms in smaller particles compared to larger ones [45]. Therefore, a particle system consisting of both smaller and larger sizes is unstable and the drive to reduce the overall surface free energy (i.e. by atoms migrating from smaller to larger particles) results in a loss of metal surface area. A literature review on sintering during Co-Catalyzed FTS is described in the introduction section of Chapter 3 of this thesis.

1.3.6. Carbon formation

Build-up of carbonaceous species on the catalyst during Fischer-Tropsch synthesis (FTS) can negatively influence activity over an extended reaction

time. The possible effects of such detrimental carbon species could be blocking of active sites and pore blockage resulting in mass transfer limitations. Moodley *et al.* concluded that polymeric carbon on spent catalyst (i.e. carbon resistant to a H₂ treatment at 350°C) could contribute to longer term deactivation in extended runs of FTS [46]. A literature review on carbon deposition during Co-Catalyzed FTS is described in the introduction section of Chapter 4 of this thesis.

1.4. Scope of the thesis

Co is the preferred metal for the gas-to-liquids process in large-scale commercial Fischer-Tropsch synthesis plants. The economics of the gas-to-liquids process is strongly dependent on the stability of the catalyst. Thus, understanding the mechanisms which cause catalyst deactivation is crucially important. The insight gained can be used to improve catalyst stability and inspire rational design of future catalysts.

There are a number of postulated deactivation mechanisms of Co FTS catalysts including (i) poisoning (which can be minimized by using a clean gas feed), (ii) oxidation (which can be prevented by tuning of particle size and reaction conditions), (iii) cobalt-support compound formation (which does not impact particle sizes optimum for FTS) and (iv) carbon-induced surface reconstruction (which requires a high carbon coverage that is not expected during FTS). This thesis provides fundamental understanding on specifically two deactivation mechanisms of Co FTS catalysts i.e. sintering and carbon formation.

Chapter 1

The principal mechanisms of sintering on supported catalysts are (i) particle migration and coalescence [47] and (ii) atomic migration also referred to as Ostwald ripening [48]. To our knowledge, direct evidence of the sintering mechanism during Co FTS has not been reported in the literature. In the present study (Chapter 3), a Co/SiO₂ planar model catalyst is exposed to realistic FTS conditions, in terms of pressure and temperature, to uncover the sintering mechanism at the single-particle level.

Oxygenated compounds are side-products in low-temperature Co-catalyzed FTS. Oxygenates could be potential precursors for polymeric carbon deposited on Co FTS catalyst due to decomposition over the metal or support surface. Carboxylic acids comprise a very small quantity of the FTS liquid products of which acetic acid is found to be the most abundant [49,50]. In the present study (Chapter 4), the deposition of polymeric carbon from carboxylic acids is investigated. Furthermore, the location (Co metal and/or γ -Al₂O₃ support) of adsorbed oxygenated species on spent catalyst is identified. Ultimately, the impact of carboxylic acids on Co FTS catalyst deactivation is assessed.

1.5. Outline of the thesis

- **Chapter 2** provides a detailed explanation on the materials and methods used to obtain the results presented in this thesis.
- **Chapter 3** deals with a study to determine the dominant sintering mechanism during Co-catalyzed FTS. This is achieved using a model

catalyst approach whereby a planar Co/SiO₂ catalyst is exposed to realistic FTS conditions and characterized using transmission electron microscopy (TEM), x-ray photoelectron spectroscopy (XPS) and Rutherford backscattering spectrometry (RBS).

- **Chapter 4** deals with an investigation into the role of carboxylic acids in Co FTS catalyst deactivation. Carbon formation from carboxylic acids is investigated by exposing real Co/Al₂O₃ catalyst to model FTS conditions followed by characterization using temperature-programmed hydrogenation coupled with mass spectrometry (TPH-MS). The location of adsorbed carboxylates on spent Co FTS catalyst is determined by studying the interaction of (i) acetic and octanoic acid with pure γ -Al₂O₃ and (ii) acetic acid with a Co metal surface, in isolation. Characterization techniques employed include attenuated total reflectance infrared spectroscopy (ATR-IR), XPS and TP-MS.
- The results of a Density Functional Theory (DFT) study to understand the adsorption of acetic acid on two representative alumina surfaces (i.e. the γ -Al₂O₃ (100) and (110) surfaces) are discussed in **Chapter 5**. Vibrational analyses on DFT optimized configurations are correlated to IR measured vibrations to determine the adsorption structure of adsorbed acetic acid on alumina.
- **Chapter 6** provides an evaluation of the results presented in this thesis in the context of Co FTS catalyst deactivation. Future work to progress the understanding on the respective research topics is proposed.

1.6. References

- [1] F. Fischer, H. Tropsch, *Brennst. Chem.* 4 (1923) 276–285.
- [2] F. Fischer, H. Tropsch, *Brennst. Chem.* 7 (1926) 97–104.
- [3] F. Fischer, H. Tropsch, patent DE 484 337, 1925.
- [4] Z. Liu, S. Shi, Y. Li, *Chem. Eng. Sci.* 65 (2010) 12–17.
- [5] H. Storch, N. Golombic, R. B. Anderson, *The Fischer–Tropsch and Related Syntheses*, Wiley, New York, 1951.
- [6] M. E. Dry, *Catal. Today* 71 (2002) 227–241.
- [7] J. van de Loosdrecht, F. G. Botes, I. M. Ciobica, A. Ferreira, P. Gibson, D. J. Moodley, A. M. Saib, J. L. Visagie, C. J. Weststrate, J. W. Niemantsverdriet, Fischer-Tropsch synthesis: catalysts and chemistry, In J. Reedijk & K. Poepelmeier (Eds.), *Comprehensive Inorganic Chemistry II (Second Edition): from elements to applications* Elsevier, Amsterdam, 2013, 525-557.
- [8] http://www.sasol.com/sites/default/files/content/files/Sasol_Fuels_technology_brochure_V18.pdf, Sasol Technology Brochure.
- [9] <http://www.sasol.com>, Sasol Financial Report July–December 2010.
- [10] A. Brown, Pearl GTL Presentation, XTL Summit, June 2011.
- [11] http://www.sasolsdr.investoreports.com/sasol_sr_2006/html/sasol_sr_2006_15.php, Sasol slurry phase distillate™ process.
- [12] A. P. Steynberg, M. E. Dry, M. E. Davis, B. H. Davis, B. B. Breman, *Stud. Surf. Sci. Catal.* 152 (2004) 64–195.
- [13] P. J. van Berge, J. van de Loosdrecht, E. A. Caricato, S. Barradas, Patent WO 9942214A1, 1999.
- [14] B. H. Davis, *Catal. Today* 71 (2002) 249–300.
- [15] A. P. Steynberg, R. L. Espinoza, B. Jager, A. C. Vosloo, *Appl. Catal. A: Gen.* 186 (1999) 41–54.
- [16] A. A Adesina, *Appl. Catal. A*, 138 (1996) 345-367.
- [17] M. E. Dry, J. C. Hoogendoorn, *Catal. Rev.* 23 (1981) 265–278.
- [18] D. G. Wei, J. G. Goodwin, R. Oukaci, A. H. Singleton, *Appl. Catal. A: Gen.* 210 (2001) 137–150.

- [19] A. Y. Khodakov, W. Chu, P. Fongarland, *Chem. Rev.* 107 (2007) 1692–1744.
- [20] A. M. Saib, D. J. Moodley, I. M. Ciobîcă, M. M. Hauman, B. H. Sigwebela, C. J. Weststrate, J. W. Niemantsverdriet, J. van de Loosdrecht, *Catal. Today* 154 (2010) 271-282.
- [21] N. E. Tsakoumis, M. Rønning, Ø. Borg, E. Rytter, A. Holmen, *Catal. Today*, 154 (2010) 162-182.
- [22] J. van de Loosdrecht, B. Balzhinimaev, J. -A. Dalmon, J. W. Niemantsverdriet, S. V. Tsybulya, A. M. Saib, P. J. van Berge, J. L. Visagie, *Catal. Today* 123 (2007) 293-302.
- [23] C.H. Bartholomew, *Appl. Catal. A: Gen.* 212 (2001) 17–60.
- [24] C.H. Bartholomew, R.M. Bowman, *Appl. Catal.* 15 (1985) 59–67.
- [25] C.G. Visconti, L. Lietti, P. Forzatti, R. Zennaro, *Appl. Catal. A: Gen.* 330 (2007) 49–56.
- [26] S. C. Leviness, C. J. Mart, W. C. Behrmann, S. J. Hsia, D. R. Neskora, US Patent 6,284,807 B1 (2001).
- [27] J. Inga, P. Kennedy, S. Leviness, WO 2005/071044 (2005).
- [28] R. B. Anderson, in P.H. Emmet (Ed), *Catalysis*, Vol 4, Reinhold, New York, 1956
- [29] A. M. Saib, A. Borgna, J. van de Loosdrecht, P. J. van Berge, J. W. Niemantsverdriet, *Appl. Catal. A: Gen.* 312 (2006) 12-19.
- [30] P. J. van Berge, J. van de Loosdrecht, S. Barradas, A.M. van der Kraan, *Catal. Today* 58 (2000) 321-334.
- [31] A. M. Saib, A. Borgna, J. van de Loosdrecht, P. J. van Berge, J. W. Niemantsverdriet, *J. Phys. Chem. B* 110 (2006) 8657-8664.
- [32] E. van Steen, M. Claeys, M. E. Dry, J. van de Loosdrecht, E. L. Viljoen, J. L. Visagie, *J. Phys. Chem. B.* 109 (2005) 3577–3757.
- [33] G. L. Bezemer, J. H. Bitter, H. P. C. E. Kuipers, H. Oosterbeek, J. E. Holewijn, X. Xu, F. Kapteijn, A. J. van Dillen, K. P. de Jong, *J. Am. Chem. Soc.* 128 (2006) 3956-3964.

Chapter 1

- [34] N. O. Elbashir, P. Dutta, A. Manivannan, M. S. Seehra, C. B. Roberts, *Appl. Catal. A: Gen.* 285 (2005) 169–180.
- [35] G. Kiss, C. E. Kliewer, G. J. DeMartin, C. C. Culross, J. E. Baumgartner, *J. Catal.* 217 (2003) 127-140.
- [36] J. L. Li, X. Zhan, Y.Q. Zhang, G. Jacobs, T. Das, B.H. Davis, *Appl. Catal. A* 228 (2002) 203-212.
- [37] D. J. Moodley, A. M. Saib, J. van de Loosdrecht, C. Welker-Nieuwoudt, B. H. Sigwebela, J. W. Niemantsverdriet, *Catal. Today* 171 (2011) 192-200.
- [38] I. M. Ciobica, R. A. van Santen, *J. Chem. Phys. B* 107 (2003) 3808–3812.
- [39] I. M. Ciobica, R. A. van Santen, P. J. van Berge, J. van de Loosdrecht, *Surf. Sci.* 602 (2008) 17-27.
- [40] C. J. Weststrate, A. C. Kizilkaya, E. T. R. Rossen, M. W. G. M. Verhoeven, I.M. Ciobica, A. M. Saib, J. W. Niemantsverdriet, *J. Phys. Chem. C* 116 (2012) 11575–11583.
- [41] C. J. Weststrate, I. M. Ciobica, A. M. Saib, D. J. Moodley, J. W. Niemantsverdriet, *Catal. Today* 228 (2014) 106–112
- [42] M. Claeys, M. E. Dry, E. van Steen, E. du Plessis, P. J. van Berge, A. M. Saib, D. J. Moodley, *J. Catal.*, 318 (2014) 193-202.
- [43] J. Wilson, C. de Groot, *J. Phys. Chem. B* 99 (1995) 7860-7866.
- [44] C. H. Bartholomew, *Appl. Catal. A* 212 (2001) 17–60.
- [45] C. T. Campbell, S. C. Parker, D. E. Starr, *Science*, 298 (2002) 811-814.
- [46] D.J. Moodley, J. van de Loosdrecht, A. M. Saib, M. J. Overett, A. K. Datye, J. W. Niemantsverdriet, *Appl. Catal. A.* 354 (2009) 102-110.
- [47] E. Ruckenstein, B. Pulvermacher, *J. Catal.*, 29 (1973) 224.
- [48] B. K. Chakraverty, *J. Phys. Chem. Solids* 28 (1967) 2401-2412.
- [49] R. R. Anderson, C. M. White, *J. High Resol. Chromatogr.* 17 (1994) 245–250.
- [50] R. J. J. Nel A. de Klerk, *Ind. Eng. Chem. Res.* 46 (2007) 3558–3565.

2

Experimental techniques and methods

2.1. Objective of this chapter

The objective of this chapter is to describe the techniques and methods used to obtain the results presented in this thesis. These include preparation of a planar model catalyst (e.g. Co/SiO₂/Si(100)) as well as background information on the spectroscopic techniques, microscopic techniques and theoretical studies.

2.2. The planar model catalyst approach

Crystallites of the active metal in a heterogeneous catalyst are typically nano-sized, implying that 'atomic level' structural, morphological and compositional detail is required to understand the catalytic process. The industrial catalyst is often too complex to obtain this information (Figure 2.1). Thus, well-defined, controllable and convenient representations of catalysts, i.e. model catalysts, are needed to achieve atomic level understanding. One particularly suitable option for surface science and transmission electron microscopy consists of a planar support with thin windows onto which nanoparticles can be deposited by spin-coating followed by calcination (described in the next section 2.3).

Model catalyst approaches have successfully been applied in a wide range of studies including olefin polymerization [1], hydrogenation [2] and hydrodesulfurization [3-5]. A model catalyst approach is used in the present study (results discussed in Chapter 3) to determine the mechanism of Co sintering during Fischer-Tropsch synthesis (FTS).

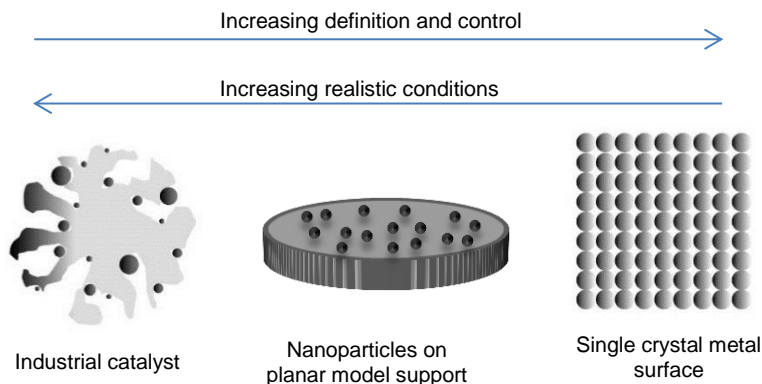


Figure 2.1: Schematic representations of industrial catalyst with a porous support, the planar model catalyst and a single crystal surface. Adapted from Ref [6].

2.3. The planar Co/SiO₂ model catalyst

Silicon wafers, which consist of a semi-conducting silicon single crystal, provide a convenient, well defined and conducting model support. These silicon crystals are terminated by a few nm thick polycrystalline SiO₂ layer, which is grown thicker (~20 nm) by calcination in air (750°C for 24h) to produce a flat silica support, i.e. SiO₂/Si(100), with only nanoscale variations in height (Figure 2.2) [7]. The model support can be modified for TEM analysis by covering it with a thin silicon nitride layer (15-20 nm thick) followed by an etching step in which a small part of the underlying silicon is etched away to create a 'membrane window' (100x100 μm²), thin enough for high energy electrons to pass through (Figure 2.2). When this TEM 'window' undergoes a calcination (750°C for 24h in air), an outer layer of amorphous silica (~3 nm thick) is formed. This model support enables

Chapter 2

morphological studies of nanoparticles deposited on the surface using TEM [8,9].

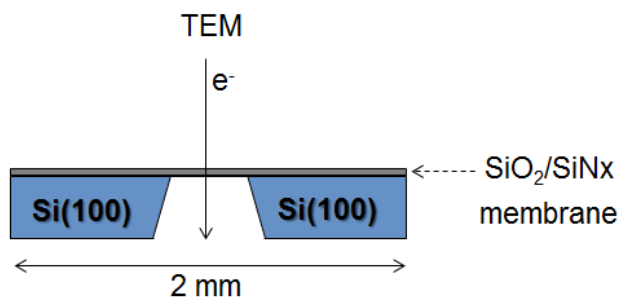


Figure 2.2: Schematic representation of a SiO₂/Si(100) substrate (well-suited to x-ray photoelectron spectroscopy) and the SiO₂/SiN_x membrane for TEM analyses. Adapted from Thüne *et al.* [7].

A range of highly informative techniques are often not easily applied to high surface area catalysts, but work particularly well on flat model systems. Planar model catalysts are well-suited to surface science techniques which typically require flat surfaces with nanoscale variations in height [10]. The support surface is sufficiently conductive to prevent charging in x-ray photoelectron spectroscopy (XPS) [11], resulting in higher resolution of photoemission spectra. The benefits of using the model catalyst for TEM studies is the fact that all nanoparticles present are exposed at the surface and can be imaged with excellent contrast. This means that small particles cannot be hidden away from view, as is the case with porous industrial supports. Most importantly for the present study (Chapter 3), the TEM ‘membrane window’ exposes an area on the model catalyst which can be conveniently found back and imaged again after a treatment. This enables a comparison of single particles before and after the treatment.

The active metal phase can be deposited onto the flat model support by a range of techniques. The technique employed in the present study is spin-coating deposition, a method that mimics the industrial practice of wet chemical impregnation [12]. In the present study (Chapter 3), a cobalt nitrate solution is spin-coated onto the substrate ($\text{SiO}_2/\text{Si}(100)$ or $\text{SiO}_2/\text{SiN}_x$). The spin-coating solution contains a polymer which is added to increase the viscosity of the solution. After spin-coating, the sample is calcined (at 350°C , $5^\circ\text{C}/\text{min}$, 5h in 20% O_2/Ar) to produce the cobalt oxide (Co_3O_4) nanoparticles on the support. The polymer is burnt off during the calcination (confirmed using XPS).

In spin-coating, a solution containing the desired material (i.e. the cobalt precursor in the present study) is deposited onto a disk (i.e. a holder containing the $\text{SiO}_2/\text{Si}(100)$ or $\text{SiO}_2/\text{SiN}_x$ substrate) and accelerated (at a spinning speed of 3000 rpm for 1 min) (Figure 2.3). During the spin-coating, solution is ejected from the spinning disk by radial flow, but a thin film remains on the substrate. Centrifugal and shear forces maintain the uniformity of the coating film while the solvent evaporates and is removed by flowing gas (N_2) [11]. The amount of material deposited varies depending on the concentration and viscosity of the spin-coating solution, the spinning speed and the evaporation time. Van Hardeveld *et al.* showed that spin-coating of dilute solutions of inorganic salts produces a predictable quantity of deposited material on the flat model substrate [12]. In their study, calculated amounts of deposited material varied by a maximum of 20% from values measured using Rutherford backscattering spectrometry (RBS) and inductively coupled plasma optical emission spectrometry (ICP-OES) [12].

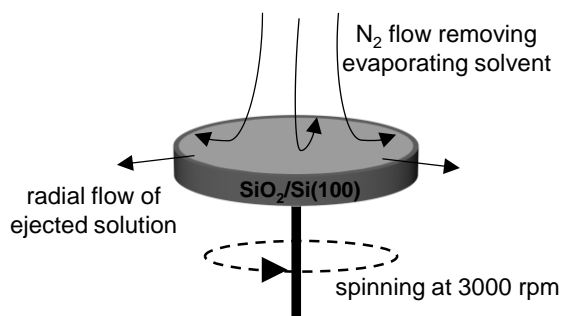


Figure 2.3: Schematic representation of the spin-coating process. Adapted from Hardeveld *et al.* [12].

2.4. X-ray photoelectron spectroscopy (XPS)

XPS is a powerful surface science technique that can be used on a variety of samples to (i) identify elements in a sample (ii) determine the relative concentration of elements in a sample and (iii) differentiate between chemical states (e.g. oxidation state) of elements.

X-ray photoelectron spectroscopy (XPS) is based on the photoelectric effect. A sample that is irradiated with light, of sufficiently small wavelength, emits electrons which are also referred to as photoelectrons [13]. The quantity of photoelectrons emitted depends on the intensity of the light and the kinetic energy of the electrons on the wavelength of the light, as well as on the chemical identity of the atom from which the electron originates. The Nobel Prize for Physics was awarded to Kai Siegbahn in 1981 for his work in the field of chemical analysis using electron spectroscopy.

Surface analysis by XPS entails the irradiation of a sample *in vacuo* with monoenergetic soft x-rays and analyzing the energy of emitted electrons [14]. Commonly used x-rays sources are Mg K α (1253.6 eV) and Al K α (1486.6 eV). The photons from these sources have a limited penetration depth of approximately 1 to 10 micrometers. Therefore, the photons interact with atoms in the surface region of the sample. The distance that emitted electrons travel through a surface depends on the electron mean free path, which in turn, depends on the electron kinetic energy [15]. Kinetic energies in the region of 15-1000 eV, limit the mean free path of electrons to 1-2 nm. Thus, electrons which leave the sample without energy loss originate from up to only a few nanometers below the surface, making XPS a surface-sensitive technique.

The kinetic energy of photoelectrons leaving the sample is detected by an electron spectrometer. The binding energy, E_b , of photoelectrons is calculated using Equation 2.1. XPS spectra are typically represented as a plot of the photoelectron intensity as function of the binding energy.

$$E_b = h\nu - \phi - E_k \quad (\text{Equation 2.1})$$

$h\nu$ is the photon energy, where h is Planck's constant & ν is the frequency of the exciting radiation). E_b is the binding energy of the atomic orbital from which the electron originated and ϕ is the spectrometer work function.

Each element has a unique set of binding energies, therefore XPS can identify the various elements in a compound. In addition, element binding energies can vary due to differences in chemical potential and polarizability of the atom. These variations are measured as chemical shifts in the XPS

Chapter 2

spectrum enabling a differentiation between the chemical states (e.g. oxidation state) of elements.

Spin-orbit splitting in the p, d and f orbital levels gives rise to two components, where the peak intensity ratio is 1:2 for p levels, 2:3 for d levels and 3:4 for f levels. The convention is to label the spin-orbit components as follows: $p_{1/2}$, $p_{3/2}$, $d_{3/2}$, $d_{5/2}$, $f_{5/2}$ and $f_{7/2}$. After photoemission, the atoms remain as unstable ions with a vacancy in the core level. The ion in the excited state will undergo a subsequent relaxation process, either *via* emission of an x-ray or emission of an Auger electron. In the latter process, an electron from the outer orbitals fills the vacancy in the core level and this energy transition results in the simultaneous emission of a second electron from the outer orbitals, the Auger electron (Figure 2.4). The Auger electron is emitted with an element-specific kinetic energy which is therefore fixed and independent of the x-ray energy used.

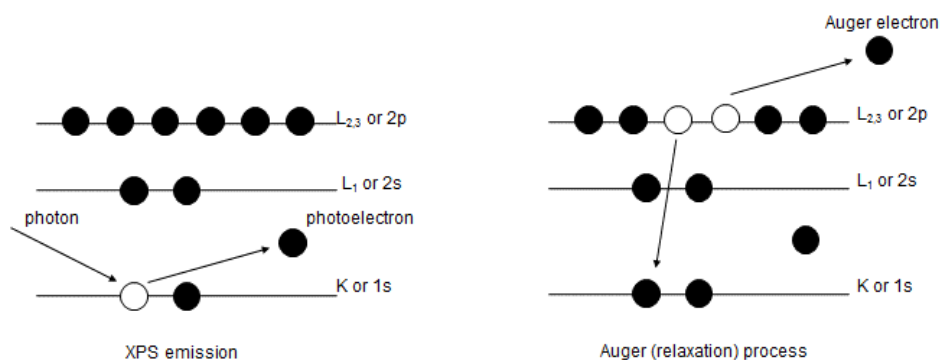


Figure 2.4: The XPS photoemission process (left) for a model atom where a photoelectron is emitted as result of an adsorbed photon. Subsequently, a relaxation (Auger) process (right) can occur whereby an Auger electron is emitted due to an electron energy transition into an inner orbital vacancy. Adapted from Moulder *et al.* [14].

Apart from emitting an electron from a core hole, the energy of the incoming photon can also be used to transfer an electron from one orbital to another. This process is called the shake-up process and can be used as a diagnostic tool because of the different binding energy of the shake-up peaks. For instance, the Co^{2+} compounds, CoO and CoAl_2O_4 , exhibit satellite peaks located ~5-6 eV above the main photoemission peaks [16]. For cobalt, the shake-up peaks arise due to a ligand-metal type charge-transfer excitation, whereby charge is transferred from the ligand (e.g. O 2p orbital in the case of CoO) to the metal (3d orbital of Co in CoO) [17,18]. Detection of these shake-up peaks proved particularly useful in the XPS analyses of Co model catalysts in the present study (Chapter 3). Metallic Co is the active phase for FTS, and thus the freshly reduced catalyst is analyzed to detect the presence of inactive Co^{2+} (cobalt oxide) compounds which present shake-up peaks.

Since XPS is surface sensitive, it can provide an indication of the dispersion of particles over a support [13]. For instance, small particles which are exposed at the surface will extensively cover the support and thus XPS will measure a high intensity from the particles (I_p) and a low intensity for the support (I_s). Thus, the XPS intensity ratio (I_p/I_s) will be high for well dispersed particles. Conversely, when more of the support is exposed as is the case with poorly dispersed particles, the XPS intensity ratio (I_p/I_s) will be low.

In this thesis, XPS is used on a range of samples with various applications. In Chapter 3, the relative surface concentration of cobalt and support (i.e. the Co/Si ratio) is used as a qualitative measure of metal dispersion on a $\text{Co/SiO}_2/\text{Si}(100)$ model catalyst before and after exposure to model FTS

Chapter 2

conditions. In Chapter 4, XPS is used to identify both short (acetate) and longer chain (octanoate) carboxylate molecules which are adsorbed on γ - Al_2O_3 and compare the relative quantities of adsorbed carboxylate before and after exposure to model FTS conditions. This is possible because the XPS spectrum shows distinctly different binding energies for the carbon atom in a carboxyl group and the carbon atom(s) in an alkyl group within the carboxylate molecule (since the carbon atoms are in different chemical environments in the molecule).

2.5. Transmission electron microscopy (TEM)

Electron microscopy is a powerful technique, widely employed to study the size and shape of supported nanoparticles. Using electron microscopy, direct local information of particles can be obtained and samples are measured in a contaminant-free environment under high-vacuum conditions.

In Chapter 3 of this thesis, transmission electron microscopy (TEM) is used to identify the changes to the size and location of cobalt nanoparticles on a model support after exposure to FTS conditions. The model support is a thin $\text{SiO}_2/\text{Si}_3\text{N}_4$ 'membrane window' through which an electron beam can pass. Ex situ TEM characterization is carried out on the model catalyst in the passivated state before and after exposure to Fischer-Tropsch synthesis (FTS) conditions.

For microscopy, the resolution obtained depends on the wavelength of the probing source e.g. light or electrons. Therefore, when using an optical

microscope, the resolution is limited to the rather long wavelength of photons (300-700 nm) [19]. Electrons have relatively much shorter wavelengths, on the order of Angstroms, therefore resolution on the atomic scale is achieved. In addition, electrons will respond to an electrostatic potential and therefore electromagnetic lenses can be used to focus and magnify images.

In a transmission electron microscope, an electron beam is transmitted through a thin electron transparent sample. Ernst Ruska and Max Knoll developed the first electron microscope in 1931, after which time Ruska was awarded the Nobel prize in 1986 for his efforts in the field. High energy electrons (100-400 keV), generated using an electron gun and accelerated using an applied voltage, are passed through a series of electromagnetic lenses and transmitted to the sample (Figure 2.5). The high energy electron beam, which is supplied in the form of parallel rays using a condenser, interacts with the sample in a number of scattering events. These include diffraction onto a focal plane and focusing onto an image plane. The 2D projection (image) is produced from the attenuated electron beam after subsequent magnification using the electron optics and is finally recorded using a highly sensitive CCD camera.

The benefit of using TEM to characterize supported particles is the distinctive contrast between particles and the support. This difference in contrast arises due to density and thickness variation over the sample which influences electron scattering. Dense regions or those with heavier elements can scatter the electron beam stronger, resulting in darker features in the TEM image. Also, less dense regions or those with lighter elements present as brighter features. The fact that transmission electron

Chapter 2

microscopy requires low pressure conditions, while catalytic reactions are often operated under high-pressure conditions, presents the challenge commonly referred to as ‘the pressure gap’. One method to circumvent this problem is to treat samples at high-pressure reaction conditions and then transport them to the TEM for analysis (i.e. the procedure followed in the present study described in Chapter 3).

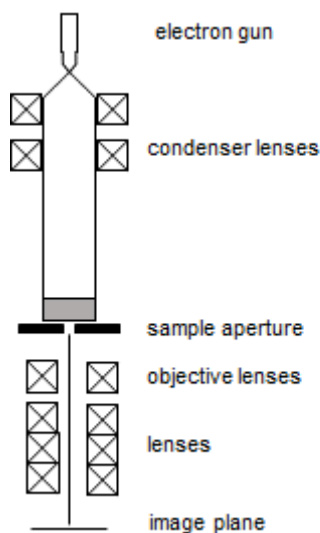


Figure 2.5: Schematic representation of a transmission electron microscope. Adapted from Niemantsverdriet [13].

2.6. Rutherford Backscattering Spectrometry (RBS)

Rutherford backscattering (RBS) is a high-energy ion scattering technique that is particularly useful in the characterization of planar model catalysts [20,21]. The elements in a sample can be identified and the metal loading on the support substrate can be precisely quantified. In Chapter 3 of this

thesis, RBS is used to quantify the cobalt loading on a $\text{SiO}_2/\text{Si}(100)$ model support before and after exposure to FTS conditions.

In ion scattering, the applied beam of ions scatters elastically from atoms in a solid (Figure 2.6). The incoming ions (energy E_i) collide with atoms in the sample and lose energy. Ions lose less energy to heavy atoms compared to lighter ones in a sample (similar to the description of the collision between billiard balls of different masses). The final kinetic energy of the ion (E_f), scattered over a specific angle (θ), is thus a function of the mass of the sample atom (Figure 2.6).

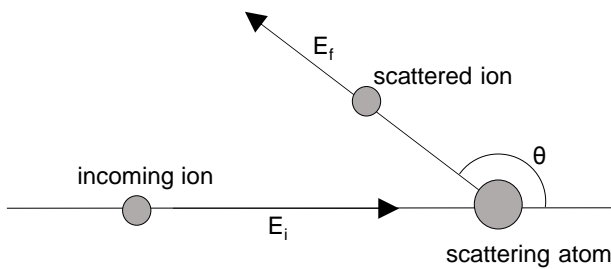


Figure 2.6: Representation of an ion scattering experiment. E_i is the energy of the incoming ion, E_f is the ion final kinetic energy and θ is the scattering angle. Adapted from Niemantsverdriet [13].

The mass of the sample atom can be identified using a parameter called the kinematic factor (K_M), which includes the energy of the incoming and outgoing ions over the specific scattering angle (Equation 2.2) [13]. Optimum differentiation between masses is obtained using incoming ions that are not too light and at relatively large scattering angles of 150° to 180° .

Chapter 2

$$K_M = \frac{E_f}{E_i} = \left(\frac{(M^2 - M_{ion}^2 \sin^2 \theta)^{\frac{1}{2}} + M_{ion} \cos \theta}{M + M_{ion}} \right)^2 \quad \text{Equation 2.2}$$

M is the atomic mass of the scattering sample atom and M_{ion} is the atomic mass of the incoming ion.

In RBS, a mono-energetic beam of usually He^+ ions, between 2 to 4 MeV, collide with atomic layers deep into the sample (penetration depth $\sim 2.5 \mu\text{m}$ on typical flat model samples) (Figure 2.7). Scattered ions which collide with elements at the surface (e.g. Co atoms of the Co/SiO₂/Si(100) model catalyst described in Chapter 3) have a final energy that is higher compared to those which originate from deeper into the sample (e.g. Si atoms of Co/SiO₂/Si(100)). This is because the latter undergo inelastic energy losses during entry or after collision. The height of an RBS spectrum signal (intensity), as well as the peak area, is a measure of the number of scattering atoms.

RBS is well-suited to the model catalyst since it consists of heavier metal atoms on a substrate of lighter elements (Figure 2.7c). This produces distinct peaks for the various atoms in overlayers (e.g. Co, Si, & O atoms in the Co/SiO₂ overlayer of Co/SiO₂/Si(100)) on a low background for the substrate (e.g. Si atoms of the Si(100) substrate), at the higher energies of the spectrum. The distinct peak for the heavier surface atoms allows precise quantification of metal loading using the peak area and atom cross section.

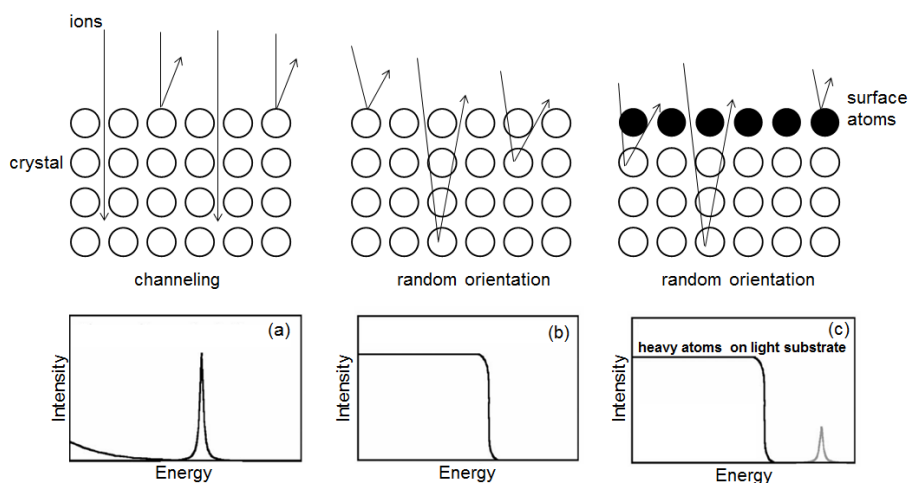


Figure 2.7: Schematic representation of Rutherford backscattering spectrometry (RBS). (a) The direction of the incoming beam is parallel to the lattice planes of the single crystal, resulting in ions being scattered back from the surface atoms and channeling deep into the crystal. (b) The incoming beam is applied in a random orientation. Ions that penetrate deeply into the crystal suffer inelastic energy losses which results in the energy of backscattered ions tailing to zero. (c) The typical case for planar model catalysts, which consists of heavy elements on top of a lighter substrate. The energy of ions scattered from the heavy surface atoms produces a sharp peak separated from that of the crystalline substrate. Adapted from Niemantsverdriet [13].

2.7. Attenuated total reflection Fourier transform infrared spectroscopy (ATR-FTIR)

Infrared (IR) spectroscopy is one of the most widely applied spectroscopic techniques in catalysis. This technique can be used to identify molecules

Chapter 2

and fingerprint chemisorbed species on catalyst surfaces by matching measured spectra with reference spectra.

IR spectroscopy is a type of vibrational spectroscopy that utilizes the process whereby vibrations in molecules are excited by the absorption of photons. Infrared radiation includes far, near and mid-IR radiation, but it is the latter with wavelengths of the order of 2-50 μm , that is most relevant for the detection of molecular vibrations [13].

Absorption of photons with frequency in the mid-IR region causes transitions between the discrete levels of vibrational energy in molecules. Atoms undergoing periodic small deviations from their equilibrium position, have a potential energy that can be approximated by the harmonic oscillator. The corresponding vibrational energy levels can be described according to Equation 2.3, which indicates that increasing bond strength and decreasing mass of the vibrating atom results in an increase in vibrational frequency.

$$E_n = (n + \frac{1}{2})h\nu \quad (\text{Equation 2.3})$$

$$\nu = \frac{1}{2\pi} \sqrt{\frac{k}{\mu}}$$

$$\mu = \frac{m_1 m_2}{m_1 + m_2}$$

E_n is the energy of the n -th vibrational level, n is an integer, h is Planck's constant, ν is the vibrational frequency, k is the bond force constant, μ is the reduced mass and m_i is the mass of the atoms in the vibrating molecule.

The selection rule for the absorption of photons implies that not all vibrations can be observed. Thus, photon absorption only occurs when a molecule possesses a permanent dipole which changes during a vibration. The vibrations depend on the translation and rotational degrees of freedom of a molecule. Linear molecules exhibit $3N-6$ (where N is the no. of atoms), while non-linear molecules exhibit $3N-5$ fundamental vibrations. These include stretching, bending (in and out of plane) as well as torsion vibrations. In addition, vibrations can also be divided into symmetric and asymmetric vibrations. Infrared vibrational frequencies are characteristic for different functional groups in molecules, due to the varying bond strengths and mass of atoms in molecules. Therefore, IR can be used to fingerprint regions and a number of correlation charts can be used to assign measured functional groups [22-24].

Attenuated total reflectance (ATR) describes the process of internal reflectance of light off the internal surface of an ATR crystal [25]. Attenuated total reflectance refers to sample absorbance of the IR beam which attenuates the intensity of the totally reflected beam (Figure 2.8).

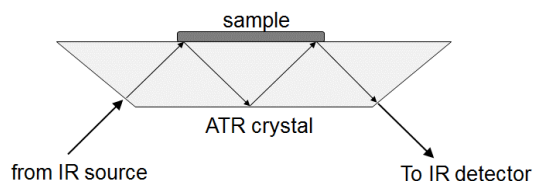


Figure 2.8: Schematic representation of the set-up for infrared measurements in attenuated total reflection mode. The IR beam undergoes reflections off the internal surface of the ATR crystal before the attenuated signal reaches the detector.

Chapter 2

Total internal reflection occurs at a specific angle of incidence, which is the angle of the incoming beam with respect to the surface normal. This critical angle depends on the refractive indices of the ATR crystal and the sample used in measurement. The IR amplitude at the point of internal reflectance produces light that projects into the sample, also referred to as an evanescent wave. Using a diamond ATR crystal and typical organic materials, the penetration depth of the evanescent wave can reach between 1-2 μm into the sample [26].

FTIR, the type of infrared spectrometer, is so called because measured interferograms are Fourier transformed to yield a spectrum [27]. The interferogram is a plot of light intensity as a function of optical path difference, which is the difference in distance travelled by two light beams which enter and leave an interferometer. The Michelson interferometer is the optical device commonly used to measure interferograms [26]. The resultant attenuated radiation (light intensity) is measured and plotted as a function of wavenumber (reciprocal wavelength) in an IR spectrum.

In Chapter 4 of this thesis, IR is used to detect the presence of oxygenated molecules on spent $\text{Co}/\text{Al}_2\text{O}_3$ FTS catalyst. IR peaks of the spent catalyst were detected at vibrational frequencies comparable to that of reference compounds of acetic and octanoic acid adsorbed on $\gamma\text{-Al}_2\text{O}_3$. This provided evidence that the oxygenated molecules on spent catalyst are composed of carboxylic acids adsorbed on the $\gamma\text{-Al}_2\text{O}_3$ support.

2.8. Temperature-programmed techniques

Temperature-programmed (TP) techniques are widely used methods which monitor chemical reactions while the temperature increases linearly with time [28]. TP instruments have become standard equipment in laboratories for catalysis research due to the relatively low cost of equipment. The instruments are relatively simple to build in the laboratory as opposed to those requiring ultra-high vacuum or reduced pressure conditions. TP techniques are versatile as they can operate practically on various types of catalysts and under relevant reaction conditions (e.g. temperature and gas atmosphere).

TP techniques use probe molecules to monitor chemical reactions as a function of temperature [13]. The probing gas is fed continuously to a tubular reactor which contains the sample in a fixed position (Figure 2.9). The probing gas can be varied according to the surface characterization targeted. The reactor is controlled by a processor which heats the reactor at the required linear rate of typically 0.1 to 20°C/min [28]. A mass spectrometer is used to measure the composition of the desorption products.

Temperature programmed techniques can be used on a quantitative basis, where reaction parameters such as pre-exponential factors and activation energies can be determined. However, quantitative interpretation can be rather complicated and thus TP techniques are often used on a qualitative basis, such as determining the maximum peak temperature or peak width at half-maximum.

Chapter 2

For instance, in temperature-programmed desorption (TPD) analysis, one simplified method used is the Redhead method [29] which provides the activation energy of desorption (E_{des}) in the case of first order-desorption and when a reliable pre-exponential value (ν) is used (Equation 2.4, where R is the gas constant). The heating rate (β) is a particularly important parameter as it impacts the rate of desorption and thus inherently can shift the peak maximum temperature (T_{max}) in a TP-MS measurement.

$$E_{des} = RT_{max} \left[\ln \left(\frac{\nu T_{max}}{\beta} \right) - 3.46 \right] \quad (\text{Equation 2.4})$$

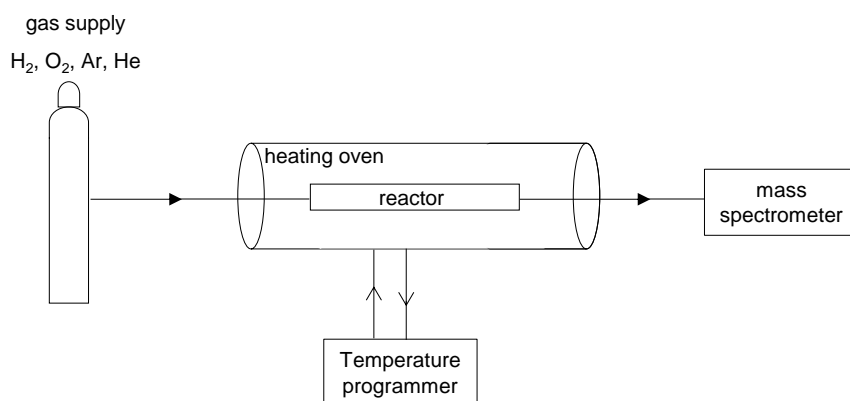


Figure 2.9: Experimental set-up for temperature-programmed hydrogenation, oxidation and desorption. The probing gas molecules can be hydrogen, oxygen or inert gas. The reactor tube is inside an oven which is connected to a temperature programmer which increases temperature linearly with time. Desorption products are detected using a mass spectrometer.

TP techniques can be combined with gas chromatography mass spectrometry (GC-MS), which is particularly useful since the individual

molecular species which make up the gaseous product mixture can be identified. Gas chromatography is the process of separating the gaseous product mixture into individual components by selectively attracting the components to a column. The column separates the components based on the time taken from injection into the GC instrument until elution through the column (retention time). The molecular structure of each component is identified by comparison of the retention times of the components to that of reference compounds.

In Chapter 4 of this thesis, temperature-programmed desorption (using inert gas) coupled with mass spectrometry (TPD-MS) is used to identify the decomposition temperature of adsorbed acid on pure γ -Al₂O₃ and detect the gaseous products released when the sample is heated. GC-MS analysis is used in combination with TPD-MS to identify the molecular structure of the desorption and reaction products. Temperature-programmed oxidation (TPO-MS) is used to quantify the carbon deposited due to acetic acid decomposition over γ -Al₂O₃. Temperature-programmed hydrogenation (TPH-MS) is used to identify the temperature at which carbon is removed (i.e. CH₄ formation) when acetic acid is decomposed over a reduced Co/ γ -Al₂O₃ FTS catalyst.

2.9. Density Functional Theory (DFT)

Quantum chemistry can be used to study a number of chemical and molecular systems in order to make predictions on the equilibrium structures of molecules, transition states and reaction pathways [30].

Chapter 2

Quantum chemistry approaches can provide information on both molecular (electronic, magnetic) and spectroscopic properties (e.g. NMR & IR).

In Chapter 5 of this thesis, Density Functional Theory (DFT) is used to describe the interaction between acetic acid and two representative alumina surfaces i.e. the γ -Al₂O₃ (100) and (110) surfaces. Vibrational frequencies are obtained by carrying out normal mode analyses on the most stable DFT optimized configurations. These frequencies are then compared to measured IR data to determine the precise adsorption structure of acetic acid adsorbed on γ -Al₂O₃. DFT calculations were performed using the VASP 4.6 package.

2.9.1. Background of DFT

DFT is an approach to find the solution to fundamental equations that describe the quantum behaviour of atoms and molecules [31,32]. The goal of most quantum mechanical approaches is to approximate the solution of the time-independent Schrödinger equation, aptly named after the development of the quantum wave equation by Erwin Schrödinger in 1926 [33]. John Pople and Walter Kohn were awarded the Nobel Prize in chemistry in 1998 for their work in the development of DFT and computational methods in quantum chemistry [30]. Two mathematical theorems by Kohn and Hohenberg as well as by Kohn and Sham (mid-1960s) forms the fundamental background of DFT.

The first Hohenberg and Kohn theorem [34] states that the ground state energy from Schrödinger's equation is a unique functional of the electron

density [35]. Their second theorem establishes the variational principle and states that the electron density that minimizes the energy of the overall functional (E_o) is the true electron density corresponding to the solution of the Schrödinger equation (Equation 2.5).

$$E_o = \min_{\rho \rightarrow N} (F(\rho) + \int \rho(r) V_{ne} dr) \quad (\text{Equation 2.5})$$

, where $F(\rho) = T(\rho) + J(\rho) + E_{ncl}$

The term (ρ) represents electron density, V_{ne} is the attractive potential exerted on electrons due to the nuclei, $T(\rho)$ is the kinetic energy term, E_{ncl} and $J(\rho)$ are the non-Coulombic and Coulombic electron-electron potentials respectively.

The Kohn-Sham method is derived from the fundamental idea that electron density can be represented as the sum of squares of N orbital densities [36], with the orbitals (referred to as spin orbitals) defining a single Slater determinant [31,37]. The ground state energy, $E(\rho)$, of a real, many-electron system can be represented by Equation 2.6, and the derived Kohn-Sham method by Equation 2.7 [35,37].

$$E(\rho) = T_s(\rho) + J(\rho) + E_{xc}(\rho) + E_{ne}(\rho) \quad (\text{Equation 2.6})$$

$$= T_s(\rho) + \frac{1}{2} \iint \frac{\rho(r_1)\rho(r_2)}{r_{12}} d_{r_1} d_{r_2} + E_{xc}(\rho) + \int \rho(r) V_{ne} dr$$

$$\left(-\frac{1}{2}\nabla^2 + V_{eff}\right) \Psi_i = \varepsilon_i \Psi_i \quad (\text{Equation 2.7})$$

V_{eff} , is the potential created when a reference system of N electrons interacts with an external potential, $E_{ne}(\rho)$ is the potential energy due to

nuclei-electron attraction, Ψ_i is the electronic wave function. The Exchange-Correlation energy, $E_{xc}(\rho)$ [31] is a functional that groups together the unknowns, including the residual kinetic energy, the Coulombic repulsion term as well as exchange and correlation energies.

2.9.2. DFT calculations using VASP

The Vienna *ab initio* Simulation package (VASP) [38] is a widely used modelling program able to perform DFT calculations. To calculate the ground-state electron density, numerical approximations are applied to accurately approach the exact solution posed by DFT using a specific exchange-correlation functional.

DFT calculations are applied to atomic arrangements that are periodic in space. Bloch's theorem [39] is used in solving the Schrödinger equation using periodic systems expressed as functions called plane-waves. VASP uses plane-waves as basis sets which have the periodicity of the supercell. VASP uses algorithms that solve the Kohn-Sham equations self-consistently using an iterative matrix diagonalization scheme with a Broyden/Pulay [40] mixing method for the charge density.

Numerical optimization enables that the electronic ground state energies are calculated for an input geometry, then the forces acting on the atoms are calculated. Thereafter, based on the calculated forces, a new geometry is proposed and the steps repeated until a convergence criterion is reached. VASP enables the numerical approximation of vibrational frequencies using the harmonic approximation and finite displacements

method. Atoms always move, or oscillate (even at 0 K) and do not have a definite position in space (due to the Heisenberg uncertainty principle). Atomic vibrations around an equilibrium position can contribute to the overall energy and are called zero-point energies. Vibrational analyses enable the determination of normal modes from vibrations of multiple atoms in molecular interactions and gives the zero-point energy corrections.

2.10. References

- [1] P. C. Thüne, J. Loos, D. Wouters, P. J. Lemstra, J. W. Niemantsverdriet, *Macromol. Symp.* 173 (2001) 37.
- [2] A. Borgna, B. G. Anderson, A. M. Saib, H. Bluhm, M. Haevecker, A. Knop-Gericke, A. E. T. Kuiper, Y. Tamminga, J. W. Niemantsverdriet, *J. Phys. Chem. B* 108 (2004) 17905-17914.
- [3] L. Coulier, V. H. J. de Beer, J. A. R. van Veen, J. W. Niemantsverdriet, *J. Catal.* 197 (2001) 26-33.
- [4] G. Kishan, L. Coulier, V. H. J. de Beer, J. A. R. van Veen, J. W. Niemantsverdriet, *J. Catal.* 96 (2000) 180-189.
- [5] A. Borgna, E. J. M. Hensen, J. A. R. van Veen, J. W. Niemantsverdriet, *J. Catal.*, 221 (2004) 541-548.
- [6] A. V. Cheruvathur, *Surface Chemistry of Flat Model Approach Ziegler-Natta Catalysts*, Ph.D Thesis, Eindhoven University of Technology, The Netherlands, 2013.
- [7] P. C. Thüne, C. J. Weststrate, P. Moodley-Gengan, A. M. Saib, J. van de Loosdrecht, J. T. Miller, J. W. Niemantsverdriet, *Catal. Sci. Technol.* 1 (2011) 689-697.
- [8] P. Moodley, F. J. E. Scheijen, J. W. Niemantsverdriet, P. C. Thüne, *Catal. Today* 154 (2010) 142-148.

Chapter 2

- [9] P. Moodley, J. Loos, J. W. Niemantsverdriet, P. C. Thüne, *Carbon* 47 (2009) 2002-2013.
- [10] P. C. Thüne, J. W. Niemantsverdriet, *Surf. Sci.* 603 (2009) 1756–1762.
- [11] P. L. J. Gunter, J. W. Niemantsverdriet, F. H. Ribeiro, G. A. Somorjai, *Catal. Rev. – Sci. Eng.* 39 (1997) 77.
- [12] R. M. van Hardeveld, P. L. Gunter, L. J. van Ijzendoorn, W. Wieldraaijer, E. W. Kuipers, J. W. Niemantsverdriet, *Appl. Surf. Sci.* 84 (1995) 339-346.
- [13] J. W. Niemantsverdriet, *Spectroscopy in Catalysis*, 3rd ed, Wiley-VCH, Weinheim, 2007.
- [14] J. F. Moulder, W. F. Stickle, P.E. Sobol, K. D. Bomben, *Handbook of X-ray Photoelectron Spectroscopy*, J. Chastain (Ed), Perkin-Elmer Corporation Physical Electronics Division, Minnesota, 1995.
- [15] G.A. Somorjai, *Chemistry in Two Dimensions, Surfaces*, Cornell University Press, Ithaca, 1981.
- [16] G. Fierro, M. L. Jacono, M. Inversi, P. Porta, *Top. Catal.* 10 (2009) 39.
- [17] K. S. Kim, *Phys. Rev. B* 11 (1975) 2177-2185.
- [18] M. A. Brisk, A.D. Baker, *J. Electron Spectrosc. Relatd. Phenom.* 7 (1975) 197-213.
- [19] R. F. Egerton, *Physical Principles of Electron Microscopy; an Introduction to TEM, SEM and AEM*, Springer-Verlag: 2005.
- [20] A. M. de Jong, H. J. Borg, L. J. van Ijzendoorn, V. G. F. M.Soudant, V. H. J. de Beer, J. A. R. van Veen, J. W. Niemantsverdriet, *J. Phys. Chem.* 97 (1993) 6477–6483.
- [21] E. M. E. van Kimmenade, A. E. T. Kuiper, Y. Tamminga, P.C. Thüne, J. W. Niemantsverdriet, *J. Catal.*, 223 (2004) 134 –141.
- [22] L. H. Little, *Infrared Spectroscopy of adsorbed species*, Academic press, New York, 1966.
- [23] A. Fadini, F.-M Schnepel, *Vibrational Spectroscopy*, Ellis-Horwood Ltd, Chichester, 1989.
- [24] W.O. George, P.S. McIntyre, *Infrared Spectroscopy*, Wiley, Chichester, 1987.

- [25] N. J. Harrick, F. K. du Pre, *Appl. Optics*, 5 (1966) 1739-1743.
- [26] B. C. Smith, *Fundamentals of Fourier Transform Infrared Spectroscopy*, 2nd ed, CRC Press, Boca Raton, 1996.
- [27] P. R. Griffiths, J. A. de Haseth, *Fourier Transform Infrared Spectroscopy*, Wiley, New York, 1986.
- [28] I. Chorkendorff, J.W. Niemantsverdriet, *Concepts of Modern Catalysis and Kinetics*, WILEY-VCH Verlag GmbH & Co. KGaA, Weinheim, 2003 (Chapter 4).
- [29] P.A. Redhead, *Vacuum* 12 (1962) 203.
- [30] http://www.nobelprize.org/nobel_prizes/chemistry/laureates/1998/advanced-chemistryprize1998.pdf
- [31] R.G. Parr, W. Yang, *Annu. Rev. Phys. Chem.* 46 (1995) 701-728.
- [32] D. Sholl, J. A. Steckel, *Density Functional Theory: A Practical Introduction*, John Wiley & Sons, Inc, New Jersey, 2009.
- [33] E. Schrödinger, *Phys. Rev.* (28) (1926) 1049-1070.
- [34] H. Hohenberg, W. Kohn, *Phys.Rev.* 136 (1964) B864-871.
- [35] W. Koch, M. C. Holthausen, *A chemist's guide to Density Functional Theory*, 2nd Ed, Wiley-VCH, Weinheim, 2001.
- [36] W. Kohn, L. J. Sham, *Phys. Rev.* 140 (1965) A1133-1138.
- [37] R.G. Parr, W. Yang, *Density-functional theory of atoms and molecules*, Oxford University Press, New York, Oxford, 1989.
- [38] <http://www.vasp.at>
- [39] F. Bloch, *Z. Physik*, 57 (1929) 545-555.
- [40] P. Pulay, *Chem.Phys. Lett.*, 73 (1980) 393-398.

3

**Ostwald ripening on a planar Co/SiO₂
catalyst exposed to model Fischer-
Tropsch synthesis conditions**

3.1. Introduction

3.1.1. Sintering as a cobalt Fischer-Tropsch synthesis catalyst deactivation mechanism

The capital investment required for a commercial-scale gas-to-liquids (GTL) plant is in the range of a billion dollars with annual profits from commercial operation reaching up to several hundred million dollars [1]. Stable catalyst performance is vital to the economics of a GTL process, making catalyst deactivation an important research topic in industrial catalyst development.

The postulated deactivation mechanisms of a cobalt Fischer-Tropsch synthesis (FTS) catalyst include (i) sintering of cobalt crystallites, (ii) carbon formation, (iii) poisoning by sulphur and/or nitrogen compounds, (iv) surface reconstruction, (v) cobalt-support compound formation and (vi) oxidation of the active cobalt metal [2,3].

In particular, sintering of the active metal phase has been identified in numerous Co-catalyzed FTS studies [4-19]. Saib *et al.*, for example, reported on the deactivation of a Co/Pt/Al₂O₃ catalyst during FTS (Figure 3.1) [3,20]. The observed deactivation was assigned to a complex interplay of deactivation mechanisms acting together but on different timescales. These proposed deactivation mechanisms included sintering as well as carbon deposition and possibly surface reconstruction under typical FTS conditions [21].

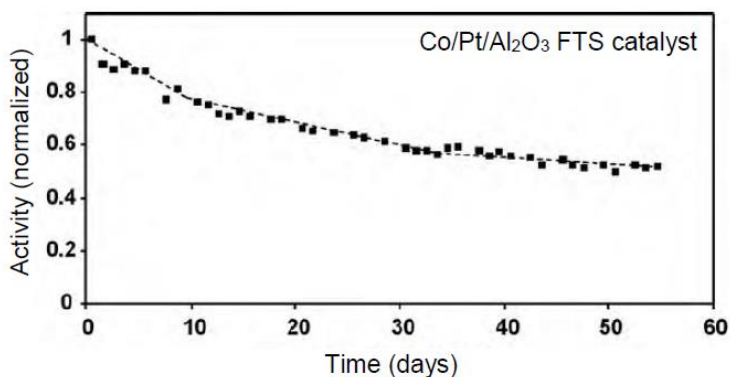


Figure 3.1: Normalized activity for a Co/Pt/Al₂O₃ catalyst during realistic FTS in a 100-barrel/day slurry bubble column reactor (230°C, 20 bar, H₂ + CO conversion of 50-70%, feed gas composition of 50-60 vol.% H₂ and 30-40 vol.% CO). Adapted from Saib *et al.* [3].

Since catalyst deactivation translates into a loss of millions of dollars in industrial application of FTS, uncovering mechanistic detail could help reduce costs inherent with deactivation and assist with the development of catalysts with improved stability. To our knowledge, direct evidence of the mechanism of loss of metal surface area during Co-catalysed FTS has not been reported in the literature. This is mainly due to the lack of direct characterization of single-particle size and location under commercially relevant reaction conditions. In this study, a Co/SiO₂ model catalyst is used in transmission electron microscopy (TEM) studies to uncover mechanistic detail on the sintering of Co nanoparticles when exposed to low conversion FTS conditions.

3.1.2. Loss of metal surface area or 'sintering'

Sintering, in the context of heterogeneous catalysis, is generally referred to as (thermally induced) catalyst deactivation caused by a loss of active metal surface area and/or support surface area [22]. However, sintering is not always thermally induced and is in reality the result of a complex interplay between different factors that affect particle loss and/or growth. These factors include (i) temperature, (ii) gas atmosphere, (iii) metal type, (iv) particle sizes and particle size distribution, (v) reaction time, (vi) support type, surface area, texture and porosity and (vii) promoters or impurities [23,24].

Sintering is unlikely to be exclusively thermally induced during Co-catalyzed FTS because of the relatively low reaction temperature typically used (200-230°C). The Hüttig temperature ($\sim 0.3 \cdot T_{\text{melting}}$) indicates the temperature where atoms at surface defects become mobile, while the Tamman temperature ($\sim 0.5 \cdot T_{\text{melting}}$) indicates the temperature when bulk atoms become mobile [25]. The Hüttig and Tamman temperatures for cobalt are around 250°C and 600°C respectively, above that of Co-catalyzed FTS. Therefore, sintering during FTS most likely proceeds *via* a mechanism in which all the abovementioned factors play a role.

Sintering, as described in an extensive review by Bartholomew *et al.*, can occur rapidly, within the first few hours [26]. Specifically in studies of Co-catalysed FTS, sintering has been reported within hours [16-18] or a few days [5,7,11,15], which is relatively fast compared to the lifetime of a catalyst. High temperatures could increase the extent of sintering as found by Rønning *et al.*, where a rather extreme temperature of 400°C resulted in

a relatively larger increase in average particle size in a Co/Re/ γ -Al₂O₃ catalyst when compared to 210°C [16]. The partial pressure of water during FTS also affects the extent of loss of metal surface area. Bertole *et al.* reported that high partial pressure of water (8 bar) significantly increased loss of metal surface area causing lower activity when using an unsupported Co-Re catalyst in isotopic transient studies [9].

‘Sintering’ is generally thought to be *thermally* induced *agglomeration* of particles when referred to in the literature. However, as discussed above, this is too simplistic in the description of a complex mechanism which depends not only on temperature but also catalyst characteristics and reaction conditions. Furthermore, the mechanism which leads to loss of metal surface area can involve mobility of atomic species and not only particle agglomeration. For this reason, the term ‘loss of metal surface area’ is used throughout the text.

3.1.3. Mechanisms of loss of metal surface area

Loss of catalyst active surface area is a result of loss and/or growth of the active metal phase. The thermodynamic driving force for the process originates from the higher chemical potential of the metal atoms in smaller particles compared to larger ones. This means that a particle system with fewer larger particles is more stable than one with many smaller particles, causing a shift toward a larger mean particle size. The Gibbs-Thomson relation (Equation 3.1) describes this dependence of the particle energy on size and provides the difference between the chemical potential of a metal atom in a particle (μ) compared to that in the bulk [27].

Chapter 3

$$\mu - \mu_0 = \frac{2\gamma\Omega}{r} \quad (\text{Equation 3.1})$$

μ_0 is the chemical potential of an infinite sized particle, γ is the metal surface free energy, Ω is the bulk metal volume per atom & r is the particle radius.

The driving force for sintering is demonstrated in work by Campbell *et al.* where it is shown that the stability of metal atoms in a particle decreases substantially as the radius decreases (below ~3nm for the system of Pb/MgO(100) based on heat of adsorption data) [28]. Thus, metal atom stability depends strongly on particle size, with atoms being more stable at larger particle sizes (as observed by little change in surface energy for particles ~8-10 nm in the case of Pb/MgO(100)). The finding that smaller particles have higher surface energy can be expected due to their relatively lower average coordination number (compared to large particles with more metal-metal bonds).

The principal mechanisms of loss of metal surface area on supported catalysts are (i) particle migration and coalescence [29] and (ii) atomic migration also referred to as Ostwald ripening [30]. Particle migration and coalescence is the *random* movement of whole particles over the support surface. When they collide with other mobile or immobile particles, they can merge to form a single, larger particle [31]. Ostwald ripening describes the emission of atomic species from immobile nanoparticles. Due to the relatively higher chemical potential of atoms in smaller particles, small particles emit more atoms than larger ones, which results is a net flux of atoms from smaller to larger particles. This flux or transfer of atoms can occur *via* diffusion over the support surface or through the vapour phase

[30,32]. Figure 3.2 shows a schematic representation of the difference between particle migration and Ostwald ripening.

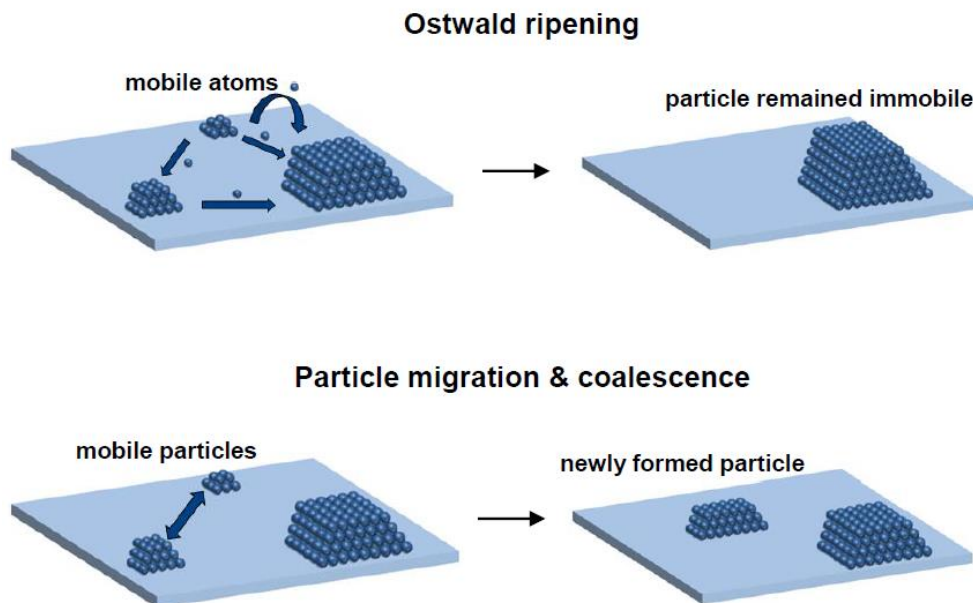


Figure 3.2: Schematic representation of the particle migration and coalescence and Ostwald ripening mechanisms. A planar surface is used to represent the catalyst support.

3.1.4. Determining mechanisms of loss of metal surface area

Direct measurements of particle sizes, particle size distributions and particle spacing is only possible using transmission electron microscopy (TEM). Other techniques to measure loss of metal surface area or particle growth include H₂ chemisorption, extended x-ray absorption fine structure (EXAFS) and x-ray diffraction (XRD). However, these techniques only

provide a single average value for loss of metal surface area from the contribution of all particles sizes.

Particle size distributions of spent catalyst, derived from TEM, have been used to indirectly derive the particle growth mechanism. For example, Sadeqzadeh *et al.* suggested that the fit of a particle size distribution of a spent Co-Re/SiO₂ FTS catalyst was indicative of a particle migration & coalescence mechanism [33]. Particle size distributions skewed to the left (Figure 3.3) have been suggested to indicate Ostwald ripening [34], while a size distribution skewed to the right (Figure 3.3) is proposed to indicate particle migration and coalescence [35,36].

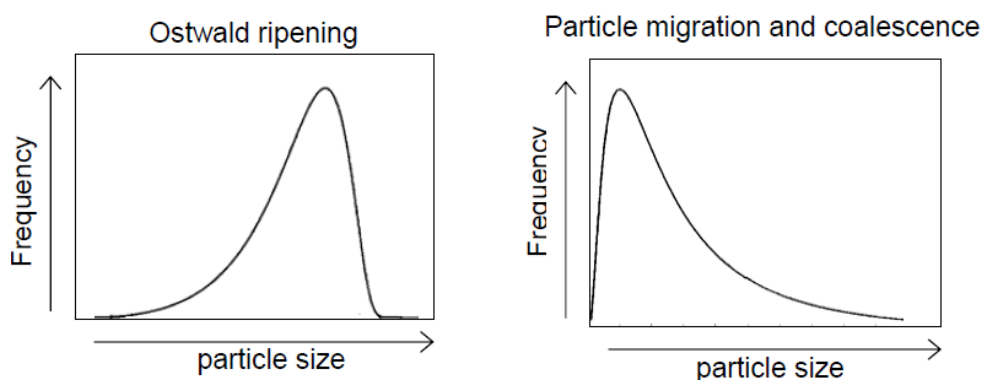


Figure 3.3: Particle size distributions proposed for Ostwald ripening [34] and particle migration and coalescence [35]. Adapted from Datye *et al.* [32]

However, the validity of this approach has been questioned in the literature [32,37]. For example, Wanke *et al.* postulated that the shape of a distribution could take a long time to change to that of the dominant mechanism [37]. Also, smaller particles in a distribution can be difficult to detect (although high-resolution TEM advancements have improved detection limits). Furthermore, Datye *et al.* deduced that the absence of a

tail toward smaller particles and a right-skewed distribution cannot be used to rule out Ostwald ripening [32].

The challenge with using TEM to determine particle growth mechanisms on supported catalysts is that it is very difficult to study particles from the same area on the industrial catalyst support before and after the reaction. Typically, randomly selected areas on the support are imaged. This means that changes to single-particle size and location is not observed. Thus, loss of metal surface area can occur, but comparing different areas on the catalyst support does not provide information on the mechanism.

Furthermore, TEM images give a two-dimensional projection of a three-dimensional support material. This can be challenging in mechanistic studies as, for example, particles located in the pores of support can be hidden from view. The approach to TEM studies using a model catalyst (described in section 3.1.6) reduces the complexity that is faced when studying the porous industrial catalyst support.

3.1.5. Determining mechanisms using model systems

Microscopy using model systems has provided direct evidence of dominant particle growth mechanisms. For instance, *in-situ* TEM operated at 10 mbar synthetic air and 650°C, convincingly revealed Ostwald ripening (atomic migration) for Pt/Al₂O₃ and Pt/SiO₂ model catalysts [38,39]. Simonsen *et al.* showed, using a Pt/SiO₂ model catalyst, that immobile particles could decay and grow over short reaction times (up to 330 min) [39]. Parkinson *et*

al. found, using scanning tunnelling microscopy imaging of a Pd/Fe₃O₄(001) model system, that a migration and coalescence mechanism occurred [40].

Thus, model systems provide an effective means of uncovering mechanisms of loss of metal surface area during reactions. The challenge with such systems is to maintain the high level of microscopy detail while operating under industrially relevant reaction conditions (which often requires high reaction pressures). One approach is to conduct the relevant reactions *ex-situ* and use the model system to maintain the high-level of microscopy detail, as is done in the present study.

3.1.6. The Co/SiO₂ model catalyst

SiO₂/Si(100) planar model systems provide a convenient and representative model for a catalyst support (Figure 3.4) [41]. The semi-conducting silicon single crystal is flat and covered by an outer layer of polycrystalline silica [42]. The model support can be modified for TEM analysis. The silicon substrate can be covered by a thin silicon nitride layer (15-20 nm thick) and the underlying silicon etched away to create a 'membrane window' (100x100 μm²), thin enough for high energy electrons to pass through (Figure 3.4). When this TEM 'window' undergoes a calcination, an outer layer of amorphous silica (~3nm thick) is formed. When using TEM, the electron beam can pass through the 'membrane window' enabling morphological studies of nanoparticles deposited on the surface [43,44]

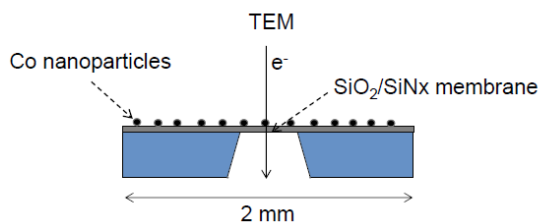


Figure 3.4: Schematic representation of the Co model catalyst with SiO₂/Si(100) substrate (well-suited to x-ray photoelectron spectroscopy) and the SiO₂/SiN_x membrane for TEM analyses. Adapted from Thüne *et al.* [42].

The support surface is sufficiently conductive to prevent charging in x-ray photoelectron spectroscopy (XPS) [45], resulting in higher resolution of photoemission measurements. The benefits of using the model catalyst for TEM studies is the fact that all nanoparticles present are exposed at the surface and can be imaged with excellent contrast on the support. This means that small particles cannot be hidden away from view, as can be the case with porous industrial supports. Most importantly for this study, the TEM ‘membrane window’ exposes an area on the model catalyst support which is conveniently found back and imaged again after the reaction. This enables a comparison of single particles before and after the reaction.

3.1.7. Research objective

In this study, a Co/SiO₂ planar model catalyst is used to uncover the mechanism of loss of metal surface area at the single-particle level. Exposure of the model catalyst to Fischer-Tropsch synthesis conditions of pressure (20 bar_a), temperature (230°C) and gas atmosphere (dry H₂/CO, low conversion) is achieved using a custom-designed high pressure

treatment cell. Characterization using TEM and x-ray photoelectron spectroscopy (XPS) is carried out before and after exposure to reaction conditions.

3.2. Materials and methods

3.2.1. Preparation of the Co model catalyst

Cobalt is deposited onto the planar model support by spin-coating of a viscous polymer solution containing the cobalt precursor. Subsequent calcination produced cobalt oxide nanoparticles on the model support, while the polymer solution is removed in the calcination step (confirmed using XPS).

3.2.1.1. Preparation of the Co containing polymer solution

Poly(methylvinylether) (10g, 50 wt% in H₂O) is added to H₂O (10 ml) and isopropanol (3.8 ml) to produce the polymer mixture. An aqueous Co(NO₃).6H₂O solution (0.5 ml from 50mM) is added to the polymer mixture (4.5 ml) to produce the spin-coating solution (5mmol) [46].

3.2.1.2. Preparation of Co nanoparticles on the model support

(i) The planar SiO₂/Si(100) support is prepared by oxidation, of a single crystal silicon wafer exposing the (100) surface plane, in stagnant air at 750 °C overnight.

(ii) The spin-coating solution is then spread over the entire support surface (2x2 cm wafer) while stationary, by applying small drops using a 1ml pipette. The sample is then spun at 3000 rpm for 1 min.

(iii) The resulting polymer-covered wafer is calcined (350 °C, 5 °C/min, 5 h) in flowing 20% O₂/Ar (20 ml(NTP)/min) and reduced (425 °C, 2 °C/min, 5 h) in pure H₂ (10 ml(NTP)/min).

(iv) This Co/SiO₂/Si(100) model catalyst is used for XPS analyses.

3.2.1.3. Preparation of the Co/SiO₂/Si₃N₄ model catalyst for TEM

(iv) For TEM analyses, an analogous procedure was used, the only difference being the use of a custom-designed model support containing the SiO₂/Si₃N₄ membrane (as described in section 3.1.6).

3.2.2. High-pressure cell experimental set-up

The Co/SiO₂ model catalyst was exposed to FTS conditions using a custom-designed high-pressure treatment cell (Figure 3.5). The model catalyst is enclosed in the treatment cell inside an oven, enabling heating to reduction and reaction temperatures. Feed gases are continuously supplied and the flow into an out of the cell is controlled independently using flow meters (Bronkhorst). After a reaction, the cell is detachable by closing the manual inlet and outlet valves for transferring samples under inert atmosphere.

A high-pressure control valve (Research Control® Valves) located before the cell maintains the required pressure during the reaction (Figure 3.6A). Samples are enclosed in the cell on a stainless steel plate (2x2 cm) with small flow openings (0.5 mm internal diameter) on opposite sides to allow the continuous gas flow through the cell (Figure 3.6B).

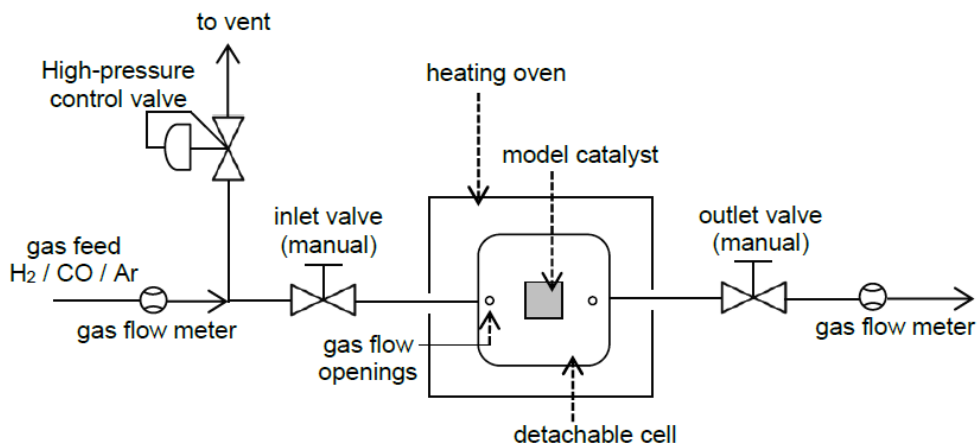


Figure 3.5: Schematic representation of the high-pressure experimental set-up.

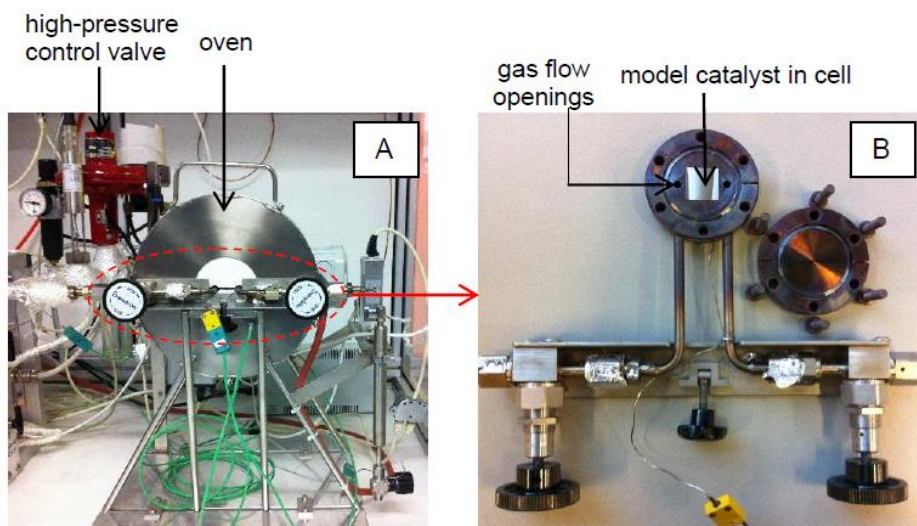


Figure 3.6: Images of (A) high-pressure experimental set-up, (B) model catalyst cell

3.2.3. Reactions using the high-pressure cell

3.2.3.1. Reduction

Calcined samples are reduced under pure H₂ (10 ml(NTP)/min) at 425°C (1°C/min) for 4h at atmospheric pressure in the cell. After the reduction, the cell is cooled to room temperature and transferred under inert atmosphere to a glovebox for passivation.

3.2.3.2. Fischer-Tropsch synthesis conditions

After characterization in the reduced-passivated state, samples are placed back into the cell where they are reduced again. After reduction, the cell is cooled from 425°C to 230°C. The cell is then pressurized to 20 bar_(a) using pure H₂. CO gas is then introduced to the cell to obtain the desired H₂/CO ratio (2/1) with a total gas flow of 10 ml(NTP)/min and a total pressure of 20 bar_(a). After the reaction time of 10h, CO gas flow is stopped and the cell is depressurized to atmospheric pressure under H₂. Finally, the cell is cooled to room temperature before inert transfer to a glovebox for passivation.

Industrial FTS reactors are typically operated at relatively high synthesis gas conversions (between 50-70%). This results in several bars of water partial pressure during the reaction. In this study, we utilize model catalysts which have low metal loading compared to industrial catalyst. This results in low conversion and therefore negligible water partial pressure. Therefore, in the present study, where only dry H₂/CO (synthesis gas) is used, the phrase 'FTS conditions' implies low conversion FTS conditions.

3.2.3.3. Reactions using only H₂

For the experiments using only a high-pressure of H₂ (i.e. to elucidate the role of CO gas), an analogous procedure is followed as described above (section 3.2.3.2) except that CO gas is not introduced at the reaction temperature (230°C), but instead the samples are exposed only to H₂ gas (20 bar_(a)) throughout the treatment.

3.2.4. Co passivation using the model catalyst cell

The target of this study was to identify loss of metal surface area and compare single-particle size and location before and after exposure to realistic reaction conditions. TEM and XPS analyses were used to achieve these targets, but both techniques require vacuum conditions to operate and are therefore not attached to the high-pressure set-up. After the reaction (reduction or FTS), samples are unloaded from the high-pressure cell under inert atmosphere, undergo a passivation step (at RT) and are finally transported through air for analyses. The passivation step prevents complete cobalt re-oxidation before characterization. In this study, passivation was achieved by overnight exposure of samples to a glovebox atmosphere, typically containing low levels of oxygen (<1 ppm) and water (~2-3 ppm). This produces a thin layer of cobalt oxide around the particles (~3 nm passivation layer as measured by TEM).

This passivation step could be carried out because the high-pressure cell is detachable from the experimental set-up (Figure 3.5). During the reaction, the cell is connected to the experimental set-up at the manual inlet and outlet valves (Figure 3.5). After a reaction, the manual inlet and outlet valves are closed, keeping the model catalyst sample under an air and

water-free atmosphere. The detached cell with closed valves is then transferred to a glovebox, where the transfer cell is opened and the samples undergo a slow passivation.

3.2.5. X-ray photoelectron spectroscopy

The passivated model catalyst samples were characterized using x-ray photoelectron spectroscopy (XPS) before and after exposure to Fischer-Tropsch synthesis conditions. Measurements on two separate XPS instruments were carried out. The first instrument (section 3.2.5.1) was used for ex situ measurements after the samples underwent passivation. For measurement of samples in the reduced state, a second XPS instrument was used, which consisted of an attached reactor cell (section 3.2.5.2).

3.2.5.1. XPS measurements (ex situ)

XPS spectra were measured using a ThermoFischer Scientific Kalpha spectrometer equipped with a monochromatic Al K α x-ray source (1486.6 eV) operating at 150W. Measurements in the analysis chamber were carried out at a background pressure of $\leq 8 \times 10^{-8}$ mbar. Binding energies were calibrated using the Si2p peak of amorphous silica at 103.3 eV. For analyses of Co dispersion, peak fitting and integration (using a Shirley background correction) was carried out using the CasaXPS software version 2.3.15. The relative peak area of the Co3p and Si2p signals, from survey spectra, were quantified and used to determine Co/Si peak intensity ratios. The average peak intensity ratios were determined using six survey spectra which were measured from different areas on the

sample. This was done to account for any sample inhomogeneity. The orientation of the sample inside the XPS chamber was noted, so that approximately the same areas on the sample could be located and measured before and after the reaction.

3.2.5.2. XPS measurements (in situ)

XPS analyses were carried out using a Kratos Axis Ultra spectrometer with monochromatic Al K α x-ray source (1486.6 eV). The sample was reduced in the attached reactor cell (1 bar_(a) pure H₂, 425°C, 1 °C/min, 4 h), cooled, the cell evacuated and finally the sample transferred under vacuum (7 x10⁻⁸ mbar) to the XPS analysis chamber.

3.2.6. Transmission Electron Microscopy (TEM)

Transmission Electron Microscopy (TEM) measurements were carried out using a Tecnai 20F (FEI) Sphera microscope with primary electron energy of 200 keV. Digital images were collected using a Gatan CCD system in the Gatan Digital Micrograph program. Typically, several images of the same area on the support are taken at varying level of focus to ensure that all particles are identified and counted.

3.2.7. Particle size determinations

Particle sizes were measured from TEM images using the ImageJ 1.45p software [47]. The particles were measured in the passivated state using TEM. The size of the passivation layer around the particles was consistently measured to be ~3 nm in size (described in detail in section 3.3.3.1). This enabled a back-calculation to obtain the metallic particle sizes.

The metal size of small particles (<6nm, i.e. less than twice passivation layer thickness) was back-calculated from the TEM measured size of the passivated particle. This back-calculation was done on a volume basis (i.e. from CoO to Co). For larger particles, the metal size is the sum of the TEM measured metal size and the back-calculated metal size from the passivation layer. These metal sizes were calculated as follows, assuming spherical particles:

(i) For smaller particles, metal radii were back-calculated according to Equation 3.2 [48] (assuming Co fcc).

(Equation 3.2):

$$d(\text{Co}) = \left[\frac{\rho(\text{CoO}) \cdot M_w(\text{Co})}{\rho(\text{Co}) \cdot M_w(\text{CoO})} \right]^{1/3} \times d(\text{CoO})$$

Mw Co: 58.93 g/mol, Mw CoO: 74.93 g/mol, $\rho(\text{Co})$: 8.72 g/cm³, $\rho(\text{CoO})$: 6.49 g/cm³

(ii) For larger particles, metal radii were calculated using a total metal volume determination according to Equation 3.3.

(Equation 3.3):

$$\text{Total metal volume} = \text{Vol}_{(\text{size measured})} + \text{Vol}_{(\text{back-calculated})}$$

$\text{Vol}_{(\text{size measured})}$ is the metal volume calculated using the TEM measured radius,

$\text{Vol}_{(\text{back-calculated})}$ is the volume of metal back-calculated (using equation 3.2) from the volume of the 3nm passivation layer around the particle.

3.2.8. Rutherford backscattering spectrometry

Rutherford backscattering spectrometry (RBS) was performed by employing a 1.85 MeV He⁺ beam produced by the HVE Singletron from AccTec BV in Eindhoven, the Netherlands (RBS by Detect99)¹. Channeling spectra have been collected under normal incidence with the surface barrier detector at a scattering angle of 155°. The layer composition was determined by simulation with the WINDF package [49].

3.3. Results

The following results section describes the characterization of the model catalyst before and after exposure to FTS conditions. The techniques used and their application is as follows:

- X-ray photoelectron spectroscopy (XPS) is used to detect all elements present on the catalyst surface, check for contamination and to obtain a qualitative measure for the average Co dispersion.
- A second XPS instrument with an attached reactor cell enables comparison of degree of reduction to detect the presence of any unreduced or metal-support compounds.
- Rutherford backscattering spectrometry (RBS) is used to determine the metal loading and exclude the loss of Co from the catalyst surface.

¹ RBS experiments carried out by Wim Arnold Bik at the Eindhoven University of Technology.

- Transmission electron microscopy (TEM) enables comparison of single-particle size and location and is the main tool used to deduce the mechanism of loss of metal surface area.

3.3.1. X-ray photoelectron spectroscopy (XPS)

3.3.1.1. Ex situ XPS

The elements present on the Co/SiO₂/Si(100) model catalyst surface were measured using XPS. Figure 3.7 depicts the reduced-passivated XPS survey spectrum. This is the state of the model catalyst when characterized using TEM as well (described in section 3.3.3). The elements cobalt, silicon, oxygen and carbon are identified, as expected. Therefore, no unwanted elements are detected and the samples are found to be sufficiently clean of contaminants.

A carbon signal is typically measured when carrying out ex situ analyses. The carbonaceous deposits originate either from the (glovebox) atmosphere or from inside the XPS chamber. Consequently, the relative concentration of carbon deposited from a reaction (e.g. hydrocarbons from FTS) cannot be determined reliably when using ex situ analyses in this manner.

Figure 3.7 (inset) shows specifically the Co2p region spectrum of reduced-passivated Co/SiO₂/Si(100). The reduced-passivated sample contains both CoO (Co2p_{3/2} peak at 781.4 eV) and metallic Co (Co2p_{3/2} peak at 778.3 eV). The peak at ~787.4 eV arises due to shake-up lines from the

photoemission process and occurs $\sim 6\text{eV}$ on the higher binding energy side of the Co $2p_{3/2}$ peak of CoO [50,51]. These spectra show that the passivation step (which includes controlled exposure to ppm levels of oxygen/water after reduction) produces CoO and leaves some metallic Co as well, thus preventing re-oxidation to Co_3O_4 .

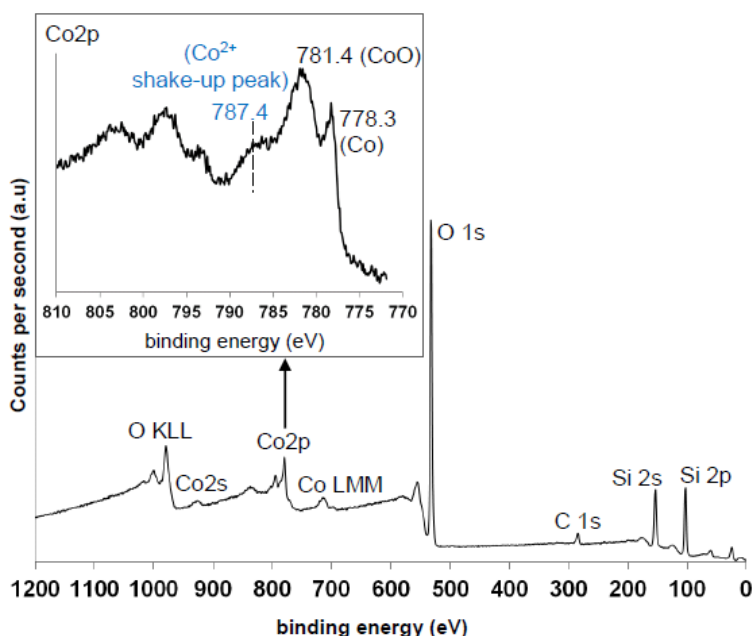


Figure 3.7: XPS survey spectrum of reduced-passivated Co/SiO₂/Si(100) model catalyst. Inset: Co2p region spectrum.

3.3.1.2. Metal surface area determinations using ex situ XPS analyses

Using XPS, the Co dispersion before and after the reaction is estimated. The relative surface concentration of cobalt and support (Co/Si ratio) is

used as a qualitative method which enables a simple comparison. The Co/Si peak intensity ratios from two separate sets of experiments are plotted in Figure 3.8. The first is before and after exposure of the model catalyst to high-pressure of H₂ (20 bar_(a)) (as described in section 3.2.3.3). The second is before and after exposure to FTS conditions.

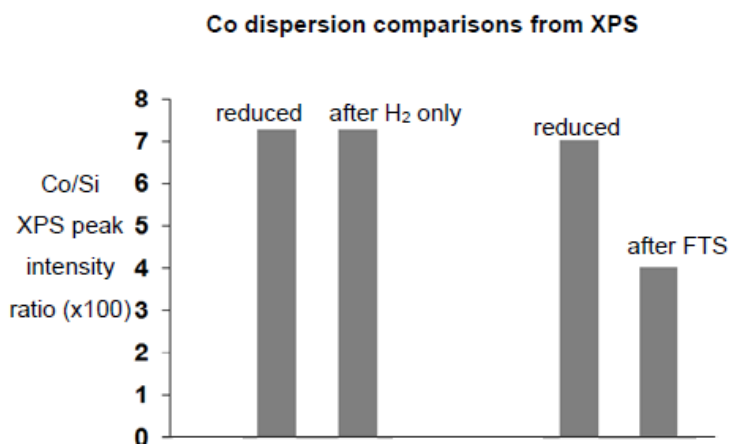


Figure 3.8: Comparison of Co/Si XPS peak intensity ratio on Co/SiO₂/Si(100) (i) in the reduced-passivated state and after reaction under pure H₂ followed by passivation, (ii) in the reduced-passivated and FTS-passivated states. Peak intensity ratios determined as described in section 3.2.5.1. Standard error in ratio values is ± 0.002 , determined using a standard deviation calculation from six measurements per sample.

The results show that the Co dispersion is unchanged after a pure H₂ treatment. However, the Co dispersion is ~40% lower after exposure to FTS conditions. The deposition of carbon, which could lower the quantity of either Co or Si that is visible by XPS, can be eliminated as a reason for this decrease in Co dispersion as the carbon-to-silica (C/Si) ratio was unchanged (Appendix Table 3.2).

3.3.1.3. Excluding formation of unreduced compounds using in situ XPS analyses

The presence of hard-to-reduce cobalt compounds, on the fresh and FTS-exposed sample, was probed using XPS. Cobalt-oxide compounds that are detected after a reduction treatment (to 425°C in pure H₂), could be due to metal-support compounds or cobalt particles that are not fully reduced.

The XPS instrument used for these experiments contains an attached reactor cell (described in section 3.2.5.2). The sample exposed to FTS conditions was passivated, re-reduced by flowing pure H₂ in the attached reactor cell and then transferred under vacuum to the XPS analysis chamber. This circumvents the passivation step and gives information on the degree of reduction. The freshly calcined sample was reduced in the attached cell and also analysed.

Figure 3.9 compares the XPS Co2p region spectrum of the FTS-exposed then re-reduced sample with a freshly reduced sample. In addition, reference compounds for Co metal and CoO are plotted. The CoO reference contains a shake-up peak (at ~787.4 eV) on the higher binding energy side of the Co2p_{3/2} peak (~780.4 eV). This shake-up peak has also previously been observed when measuring a Co₂SiO₄ compound [52]. Thus, the shake-up peak is distinctive of a Co²⁺ species. This shake-up peak is not identified on either the freshly reduced or FTS-exposed and re-reduced sample. In fact, the model catalyst samples closely match the reference spectrum of metallic Co, which presents with the Co2p_{3/2} (~778.3 eV) and Co2p_{1/2} (~793.3 eV) peaks.

These findings imply that the fresh sample is fully reduced and the formation of cobalt-oxide compounds (such as Co₂SiO₄) during the FTS reaction, is not significant.

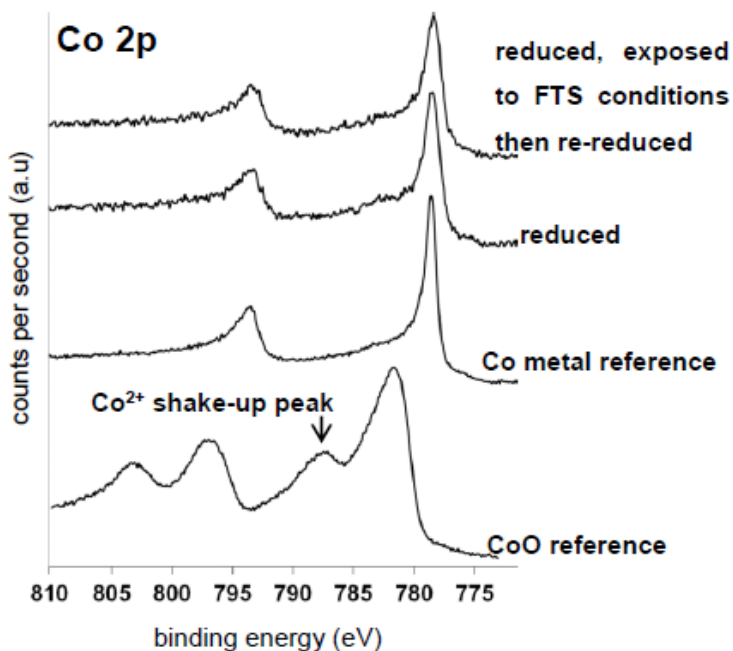


Figure 3.9: XPS Co2p region spectrum of Co/SiO₂/Si(100) model catalyst (i) reduced, exposed to FTS conditions then re-reduced and (ii) reduced. Reference compounds of metallic Co (a sputtered metal foil) and CoO (prepared by decomposition of Co(OH)₂ followed by fast transfer through air to the XPS instrument) are also plotted.

3.3.2. Rutherford backscattering spectrometry (RBS)

Rutherford backscattering spectrometry (RBS) was used to compare the Co loading on the Co/SiO₂/Si(100) model catalyst before and after exposure to FTS conditions (Figure 3.10). RBS quantifies all the cobalt present on the sample, not just that at the surface (as opposed to XPS). Therefore, it can be deduced whether Co is removed from the catalyst surface during the reaction, for e.g., by evaporation of volatile Co species such as carbonyls. RBS analyses indicated that the Co loading before and after exposure to FTS conditions is comparable ($\sim 5.0 \times 10^{15}$ Co atoms/cm²). This indicated that the quantity of cobalt on the support is conserved during the FTS reaction and therefore no Co metal is lost from the surface.

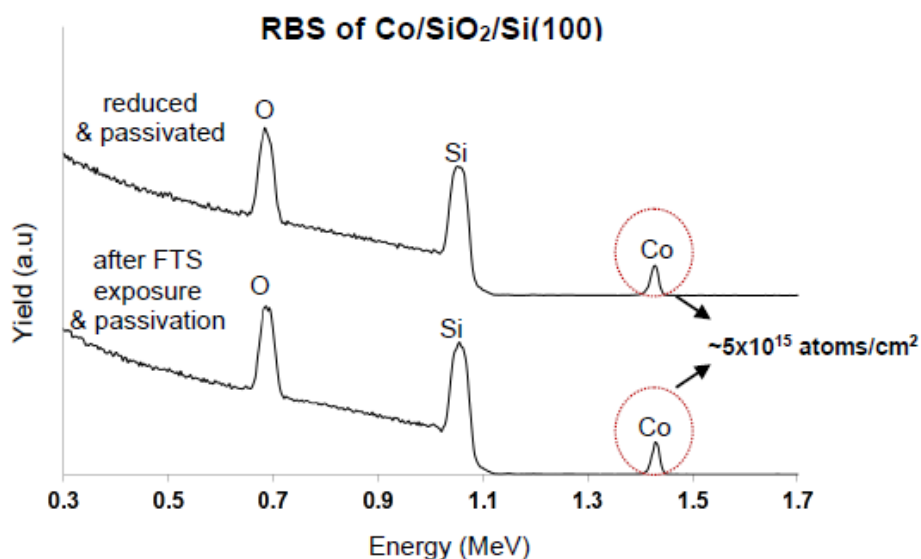


Figure 3.10: Rutherford backscattering spectra of Co/SiO₂/Si(100) (i) reduced-passivated and (ii) FTS-exposed and passivated. Statistical error in Co loading: 1.5%.

3.3.3. Transmission electron microscopy (TEM)

3.3.3.1. TEM after passivation

The passivation step after reduction or exposure to FTS conditions (described in section 3.2.4), resulted in the formation of CoO and prevented complete re-oxidation (confirmed by XPS, Figure 3.7). This enabled ex situ TEM characterization of the nanoparticles which are preserved in a state that is representative of their size (metal size with passivation layer) and location on the silica support during the reaction. Figure 3.11 shows two bright-field TEM images of a reduced-passivated sample. Both images, taken from different areas on the support, show cobalt particles as a dark core surrounded by a thin and slightly more transparent outer layer. The dark core is interpreted as metallic Co, while the thin outer layer is assigned to the passivation layer of (amorphous) CoO. The outer layer and inner core are clearly visible for relatively larger particles, but for some of the smaller particles, a darker inner core is not observed. This implies that for small particles the metallic cobalt is quantitatively converted to CoO during passivation.

The TEM images enable an accurate measurement of the thickness of this passivation layer. From a large number of measurements on particles of various sizes, the thickness of the passivation layer was estimated to be ~3nm (schematic below in Figure 3.11). This determination of passivation layer thickness was used to back-calculate the original metallic particles size (explained in detail in section 3.2.7) after both reduction and exposure to FTS conditions.

Chapter 3

TEM observation of a thin CoO passivation layer around the metallic cobalt particle explains the detection of both cobalt metal and CoO by XPS (Figure 3.7). This CoO layer completely encapsulates the metallic particle, but is thin enough to enable photoelectrons from the underlying metallic cobalt to escape and reach the detector.

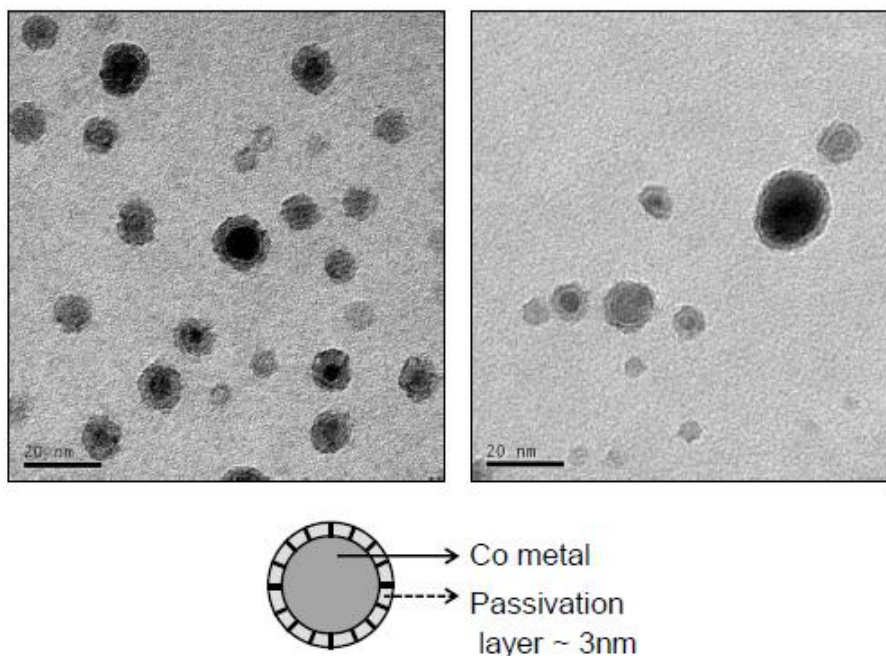


Figure 3.11: Bright-field TEM images of a reduced-passivated model catalyst. Darker features are the Co particles while the brighter background is the silica support layer. The schematic shows that the metallic particles are encapsulated by the thin passivation layer (consistently measured to be ~3nm).

3.3.3.2. TEM before & after exposure to high-pressure H₂ conditions

In this study, TEM is used to identify the mechanism of loss of metal surface area. This is done by comparing single-particle size and location, on the same area of the support, before and after the reaction.

To observe changes to particles due to only H₂ gas and temperature, TEM was carried out on the cobalt model catalyst before (reduced-passivated state) and after exposure to high-pressure conditions i.e. (20 bar_(a)) pure H₂ gas at 230°C for 10h. Figure 3.12 compares TEM images of sample before (images a & c) and after the treatment (images b & d). Selected areas (box frames in images (a) and (b)) have been further magnified to produce images (c) and (d). Figure 3.12 shows that the same area on the support was measured before and after the reaction.

In this particular case, the reduced-passivated fresh sample shows a somewhat thicker passivation layer compared to the treated sample. This can be attributed to a harsher passivation of this sample i.e. more metallic Co converted to CoO as a somewhat more crude passivation method was used for this earlier sample (i.e. the sample was unloaded in air rather than controlled passivation in a glovebox as was the case for all other samples). This difference in extent of passivation does not affect observations of particle loss (in fact lack thereof) or location of particles after the reaction.

The location of all particles is found to be identical before and after the treatment (Figure 3.12). In addition, all Co particles present before the reaction are also observed after the reaction (i.e. none are lost). In other

words, neither particle migration nor particle loss or growth occurs at typical FTS temperatures and in the presence of H_2 . This is confirmed by the XPS measurements (Figure 3.8), which showed that the Co dispersion is unchanged after a pure H_2 treatment.

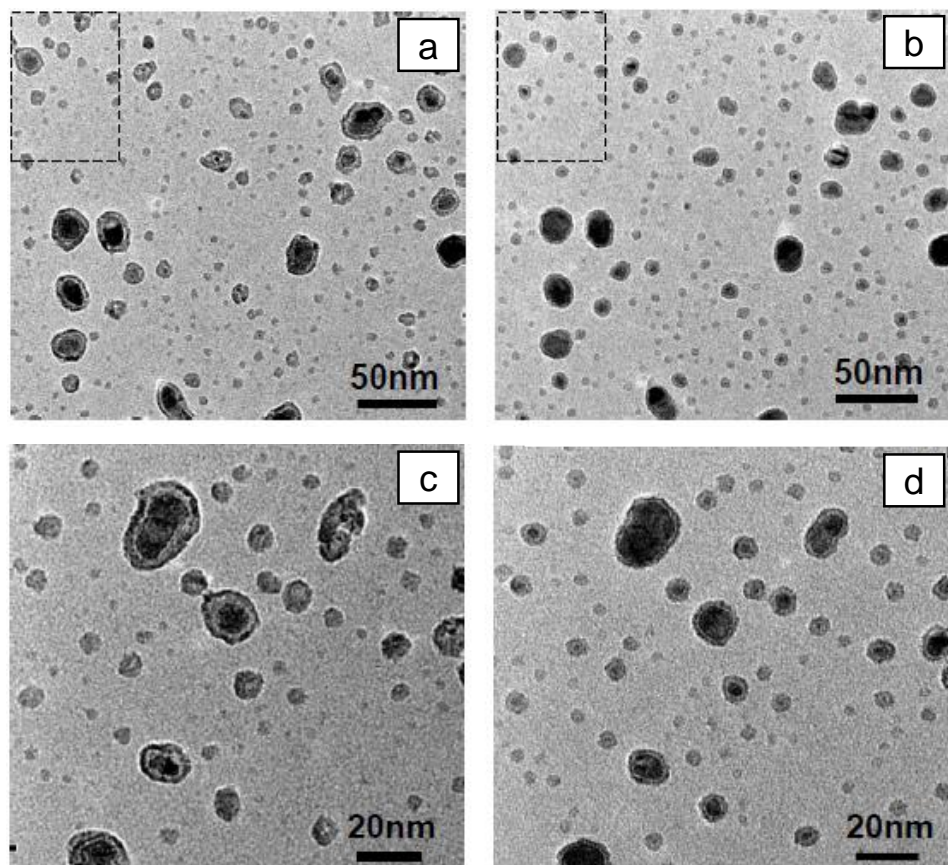


Figure 3.12: Bright-field TEM images of model catalyst reduced-passivated (a & c) and exposed to high-pressure H_2 conditions (20 bar_(a) at 230°C for 10h) & passivated (b & d). The box frames in image (a) and (b) indicate the specific areas that have been magnified to produce images (c) and (d) respectively (sample area measured is 140 x 140 nm)

3.3.3.3. TEM before & after exposure to Fischer-Tropsch synthesis conditions

Figure 3.13 compares the TEM images of the same area on a model catalyst before and after exposure to FTS conditions (i.e. 20 bar_(a) H₂/CO:2/1 at 230°C for 10h). TEM images (a) & (c) show the fresh reduced-passivated state and images (b) & (d) shows the FTS-exposed then passivated state. Selected areas (box frames in images (a) and (b)) have been further magnified to produce images (c) and (d).

Under these reaction conditions, changes to Co nanoparticles due to exposure to FTS conditions, is clearly evident. Firstly, loss of some relatively smaller particles is observed (red circles in Figure 3.13(c)). The size of these smaller particles lost is measured to be ~4nm (i.e. corrected Co metal size). The loss of Co particles is quantified by manual particle counting using these TEM images (Table 3.1), where the particles density after exposure to FTS conditions has decreased by ~17%.

Table 3.1: Co particle densities before and after exposure to FTS conditions

Co/SiO₂/Si(100) treatment	Number of particles per μm² support *
Reduced-passivated	1445
FTS conditions-passivated	1200

* 71 & 59 particles were counted from the respective TEM images (Fig 3.13 a & b). When counted manually, higher magnification images enable a more precise measurement of particle diameters (compared to lower magnification images where particles appear smaller due to scale). In this study, all particles that could be identified in the respective images were counted.

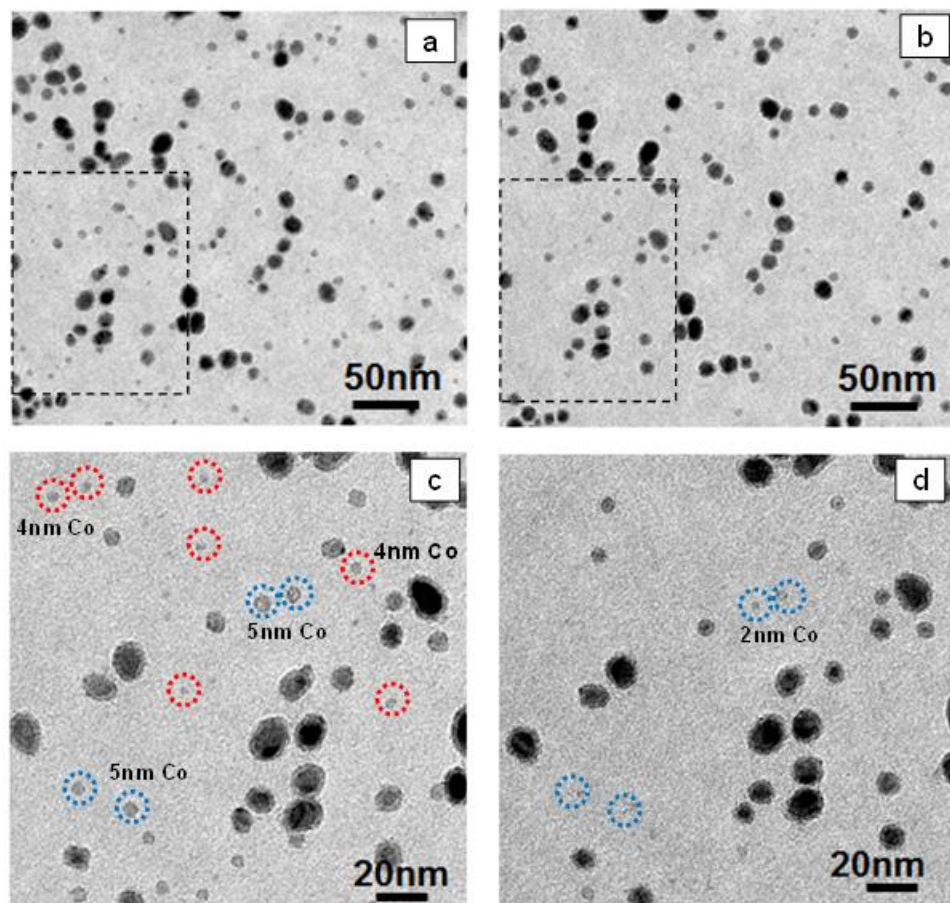


Figure 3.13: Bright-field TEM images of model catalyst reduced-passivated (a & c) and after exposure to FTS conditions then passivation (b & d). The box frame in images (a) and (b) indicate the specific areas that have been magnified to produce images (c) and (d) respectively (sample area measured is 180 x 180 nm). Red dashed circles indicate particles which have been lost during FTS treatment. Blue dashed circles indicate particles which have significantly decreased in size with treatment.

Furthermore, some of the larger particles (typically ~5nm) were found to decrease considerably in size (to ~2nm) after exposure to FTS conditions (blue circles in Figure 3.13 (c) and (d)).

Finally, the remaining particles (i.e. are not lost) are found to be at the same location on the support before and after the reaction. This implies that these particles remained immobile on the support during the reaction.

The growth of particles due to the incorporation of the cobalt that was initially present in the relatively smaller particles, is not clearly apparent from the TEM images. As the particle volume scales with d^3 , the increase of the diameter of a large particle requires a significant volume increase. For example, for a particle of radius of 10nm to increase to 11nm its volume will increase by ~1400nm³ (from 4189nm³ to 5580nm³ assuming spherical particles). This increase is equivalent to the volume of five 4nm particles. Thus, particles which have incorporated atoms from other relatively smaller particles, have probably not grown enough to see a significant increase in their diameter.

Particle size distributions before and after exposure to FTS conditions were determined using the corrected metal sizes (Figure 3.14). Interestingly, a number of smaller particles, below the size of ~4nm, are still measured after exposure to FTS conditions. This implies that these particles have either not lost any mass during FTS and/or they originate from larger particles which have lost some of their initial mass and have consequently decreased in size.

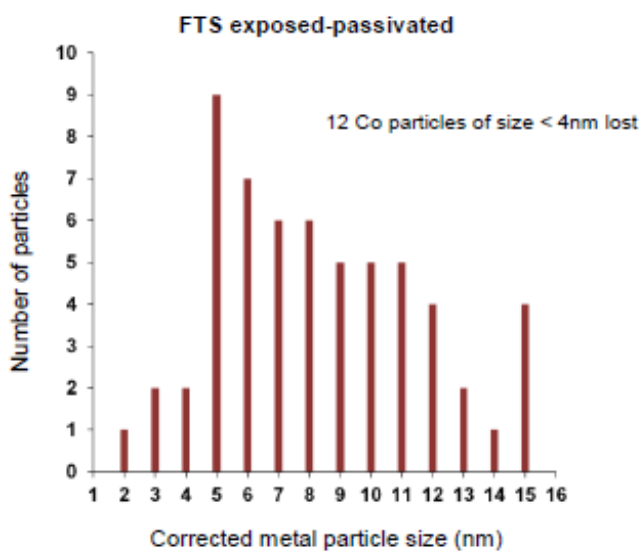
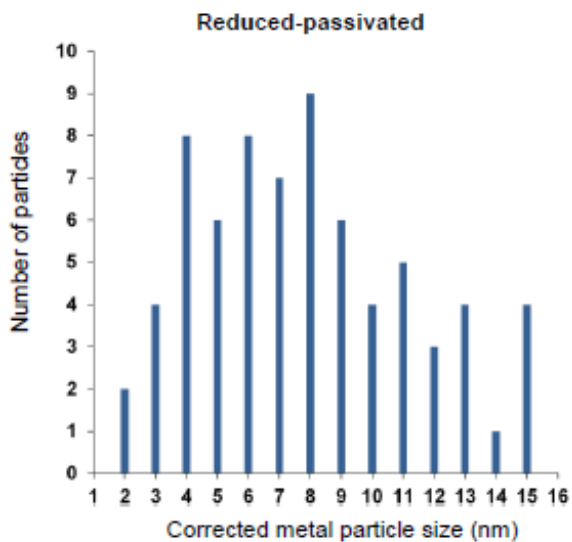


Figure 3.14: Particle size distribution of corrected metallic particles sizes before & after exposure to FTS conditions (derived from 71 & 59 particles counted respectively).

The possibility of beam damage needs to be thoroughly taken into account in studies with prolonged beam exposure times such as *in-situ* TEM studies [38,39]. The energetic beam has previously been shown to result in particle decay and this could be mistakenly interpreted as sintering. In this study, however, imaging was carried out over relatively short times (within 30 min per sample) and reactions carried out in a reaction cell outside the TEM instrument. Therefore, any effect of the beam was minimized.

Typically, several images of the same area on the support are taken at varying level of optical focus to ensure that all particles are identified and counted. These TEM observations are confirmed by a duplicate experiment (Appendix A, Figure 3.16), where a different sample was used under otherwise the same conditions.

3.4. Discussion

Loss of metal surface area is a proven deactivation pathway in Co-catalyzed low-temperature FTS. To our knowledge, direct observation of the loss of metal surface area has not been reported in the literature. After exposure of the Co/SiO₂/Si(100) model catalyst to FTS conditions (i.e. 20 bar_(a) dry H₂/CO (2/1) at 230°C), cobalt dispersion decreases significantly (~40% decrease of Co/Si ratio in XPS). The fact that this occurs in a short time interval (10h) shows that the initial decrease in metal surface area is a rapid process. No loss in Co dispersion is found in experiments using pure H₂ gas only (i.e. 20 bar_(a) dry H₂ at 230°C for 10h), which implies that CO

Chapter 3

gas is required, in addition to H₂ at FTS temperature, for loss of metal surface area to occur.

TEM findings provide important information on the mechanism of loss of metal surface area due to exposure to FTS conditions. TEM shows that some small particles disappear (≤ 4 nm corrected metal size), while some particles decrease in size (from ~ 5 nm to 2nm). Furthermore, the remaining particles are completely immobile during the FTS reaction.

The *random* movement of particles over the surface, or the collision and merging of particles is not observed by TEM in our experiments. Therefore, a particle migration and coalescence mechanism, as previously suggested by Sadeqzadeh *et al.* [33] & Tsakoumis *et al.* [53], is not observed on the model catalyst under the reaction conditions used. On supported catalysts, the mechanism of loss of metal surface area is typically derived from changes in the shape of the particle size distribution [33,53], while in the present study, changes are observed at the single-particle level (using TEM).

The present study provides direct evidence of Ostwald ripening of smaller particles in the early stages of FTS, where loss of metal surface area proceeds *via* diffusion of monoatomic species (or very small clusters) over the support surface with particles remaining immobile. This is in agreement with the observations of Hansen *et al.* for Ni sintering on MgAl₂O₄ in a reaction atmosphere of H₂/H₂O (1:1) at 4mbar and 750°C [54-56]. In their study, early stages of sintering were dominated by the loss of small particles (initial size of ~ 2.5 nm) which was found to be very rapid (within

3h), with the important mechanism of sintering deduced to be atomic migration rather than particle migration [54].

The reason for the observed rapid loss of smaller particles (*via* atomic migration) compared to larger particles, can be explained in terms of the difference in surface energy of atoms in smaller particles compared to larger ones. Campbell *et al.* showed that the stability of metal atoms in a particle decreases substantially as the radius decreases (below ~3nm for the system of Pb/MgO(100)) [28]. Thus, metal atom stability depends strongly on particle size, with atoms being more stable at larger particle sizes (as observed by little change in surface energy for particles ~8-10 nm in the case of Pb/MgO(100) [28]).

In the present study, in situ XPS analyses shows that the fresh model catalyst was fully reduced after the reduction step and that metal-support compound formation (e.g. CoO-SiO_x) was not significant. Since cobalt loading on the support was conserved during exposure to FTS conditions (determined using RBS analyses), it is concluded that cobalt did not leave the sample *via* the gas phase, which certainly would have occurred if volatile Co compounds had formed. These findings imply that metal-support compound formation and volatile Co species can be excluded as reasons for the measured loss in Co dispersion (XPS) and loss of smaller particles (TEM). Since the formation of volatile cobalt species was not significant, this confirms that Co transport took place over the support surface and gas phase transport is not significant.

Loss of metal surface area is not observed unless CO gas is present (i.e. both CO and H₂ gas is required at FTS temperature). Cobalt-subcarbonyl

Chapter 3

species, $\text{Co}(\text{CO})_x$ ($x=1-4$), have previously been considered to be mobile species over a Co surface under CO hydrogenation conditions ($\text{H}_2/\text{CO}:2$, 4 bar, 250°C) [57]. (Sub)carbonyls undergoing Ostwald ripening have also been considered to be the mobile species in CO hydrogenation using Ni catalysts ($\text{H}_2/\text{CO}:2$, 1 bar, 230°C) [58], although in the case of Ni gas phase transport is likely. Instead for Co, the mobile species is deduced to be transported *via* diffusion over the support surface (implied from RBS data). Volatile Co-carbonyls are more difficult to form than Ni-carbonyls as they contain two Co atoms ($\text{Co}_2(\text{CO})_8$) [59] as opposed to the volatile Ni carbonyl ($\text{Ni}(\text{CO})_4$). The observation that Co mobility is only apparent in the presence of $\text{CO}_{(\text{g})}$ is thus taken as evidence that mobile cobalt-subcarbonyl species, transported *via* diffusion over the support, is the principal mechanism for transport of Co during the FTS reaction (under the negligible water partial pressure conditions used in this study).

Experimental details needs to be carefully considered when generalizing the loss of metal surface area that is found in a specific reaction environment [23]. Factors such as reaction gas atmosphere and less obvious parameters such as catalyst pre-treatments and even catalyst preparation method could also affect particle growth [60]. An important discrepancy between the present model study and commercially applied FTS, is the absence of water. Industrial FTS reactors are typically operated at relatively high synthesis gas conversions (between 50-70%), resulting in a water partial pressure of $\sim 4-6$ bar during the reaction [21]. In this study, the utilized model catalyst has a significantly low metal loading compared to industrial catalyst, resulting in low conversion and therefore negligible water partial pressure. Bertole *et al.* reported that high partial pressures of water (8 bar) significantly increased loss of metal surface area compared to lower

pressures, resulting in lower activity when using an unsupported Co-Re catalyst in isotopic transient studies [9]. Thus, loss of metal surface area could be greater under conditions of high water partial pressure, which could mean that atomic migration occurs faster or that pathways for instances of particle migration are created.

A more fundamental limit for the usefulness of planar model catalysts is the support. The model catalyst consists of a smooth, planar support surface, while the industrially employed high surface area supports expose rough, highly defective surfaces and are typically nanocrystalline. This affects the interaction of Co particles and mobile Co species with the support and could therefore give rise to differences, in particular to the sintering rate. The impact of support substrate was recently shown by Fukamori *et al.* where it was proposed that mitigation of sintering could be achieved when the support substrate contains areas which strongly adsorb metal clusters (preventing cluster diffusion) and areas of weak interaction with metal atoms (preventing atomic diffusion) [61]. Monodispersed Pd clusters underwent Ostwald ripening on a Rh(111) surface (scanning tunnelling microscopy over several hours at RT under ultrahigh vacuum conditions) exhibiting strong adsorption of metal clusters, while particle migration & coalescence was found to dominate on a graphene/Rh(111) substrate (after annealing to 300K-500K under ultrahigh vacuum conditions) attributed to relatively weaker cluster adsorption on the substrate [61]. Apart from the roughness and defect density, chemical nature is expected to be important as well. Al₂O₃, for example, could have an impact on Co reducibility when compared to SiO₂, which is typically attributed to a stronger interaction between the metal and the support. This interaction of

Chapter 3

metal and support could also play a role for Co mobility over the support surface.

Thus, the present model study provides a starting point for understanding the loss of Co metal surface area during FTS on a fundamental level. The impact of other contributing factors on the dominant mechanism of loss of metal surface area, in particular the chemical nature of the support and the role of water, needs to be investigated further using the model catalyst. This can be done by changing the model support material as well as co-feeding water to mimic FTS at realistic conversion.

Industrial catalyst often consists of a mixture of both larger and smaller particle sizes (i.e. a wide particle size distribution). For FTS on such a catalyst, loss of metal surface area alone does not necessarily mean loss of activity, due to the size-dependent reactivity of Co in FTS. Bezemer *et al.* reported that particles smaller than 6-8nm have a low activity [62] and hence their loss would not greatly affect the observed FTS activity. In the present study, the loss of ~4nm particles was observed within the reaction time of 10h, while some particles of ~5nm were observed to decrease in size. Particles larger than 5nm, which may be optimum for FTS activity, could become smaller with longer reaction times (>10h), resulting in particles sizes which have low activity in FTS. Therefore, atomic migration of cobalt could contribute to catalyst deactivation.

Our findings indicate that two approaches should be investigated. This includes reducing the driving force for sintering (thermodynamic consideration) and slowing down the diffusion of mobile Co species (kinetic considerations). One method can be to prepare fresh catalyst particles with

a highly uniform particle size distribution (ideally with the optimal size for target FTS performance [62,63]). This results in a catalyst with particles of similar surface energy which will slow Co mobility. Loss of metal surface area could also be slowed down by maximizing the inter-particle distances during the catalyst preparation step. This increases the diffusion distance of mobile species which therefore applies to both Ostwald ripening and particle migration and coalescence. Lower Co loading could increase inter-particle distance, but this may be less desirable in commercial catalyst preparation (where highest activity per volume of catalyst used is important). Alternatively, the reaction conditions can be adjusted to suppress formation of atomic cobalt-subcarbonyl species, such as lowering the CO pressure (also a limited parameter as target FTS performance is dependent on H₂, CO and H₂O partial pressures).

3.5. Conclusion

The mechanism of loss of metal surface area was studied by exposing a Co/SiO₂/Si(100) model catalyst to low-conversion Co Fischer-Tropsch synthesis (FTS) conditions. Identical location TEM showed the loss of ≤4nm particles and decrease in size of ~5nm particles within 10h. All remaining particles were immobile during the reaction, indicating that Ostwald ripening mechanism is dominant using our model catalyst under the present conditions. It was found that loss of metal surface area at FT temperature requires the presence of CO in combination with H₂, as the temperature is too low for purely thermally-induced loss of metal surface area. Metal-support compound formation as well as the formation of volatile species were excluded as reasons for the measured loss of metal surface

Chapter 3

area. These findings suggested that the mechanism proceeds *via* a mobile cobalt-subcarbonyl species that is transported *via* diffusion over the support surface. The rapid loss of particles and decrease in particle size *via* Ostwald ripening implies that particle sizes can be altered to sizes that are less active for FTS and in this way could contribute to catalyst deactivation.

3.6. Appendix

Table 3.2: XPS analyses of Co/SiO₂/Si(100). Co/Si and C/Si peak intensity ratios of reduced-passivated, FTS exposed-passivated and H₂ exposed-passivated.

Co/SiO ₂ /Si(100) treatment	Co/Si XPS peak intensity ratio	C/Si XPS peak intensity ratio
reduced-passivated	0.07	0.08
FTS exposed-passivated	0.04	0.08
reduced-passivated	0.07	0.03
H ₂ exposed-passivated	0.07	0.12

Peak ratios determined as described in section 3.2.5.1.

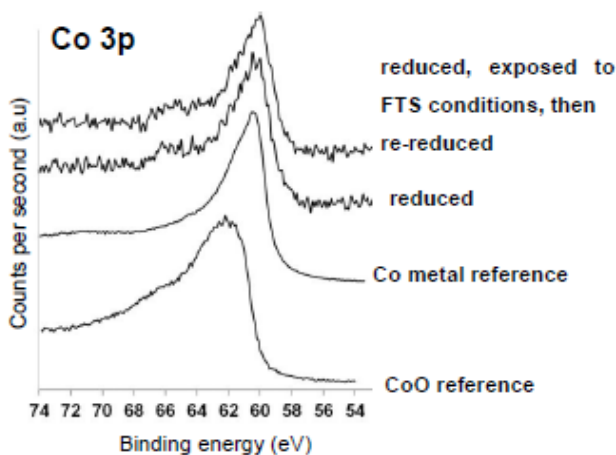


Figure 3.15: XPS Co3p of reduced Co/SiO₂/Si(100) model catalyst and sample that is reduced, exposed to FTS conditions and reduced again. Reference compounds for metallic Co and CoO are also plotted.

TEM before and after exposure to Fischer-Tropsch synthesis conditions (duplicate experiment)

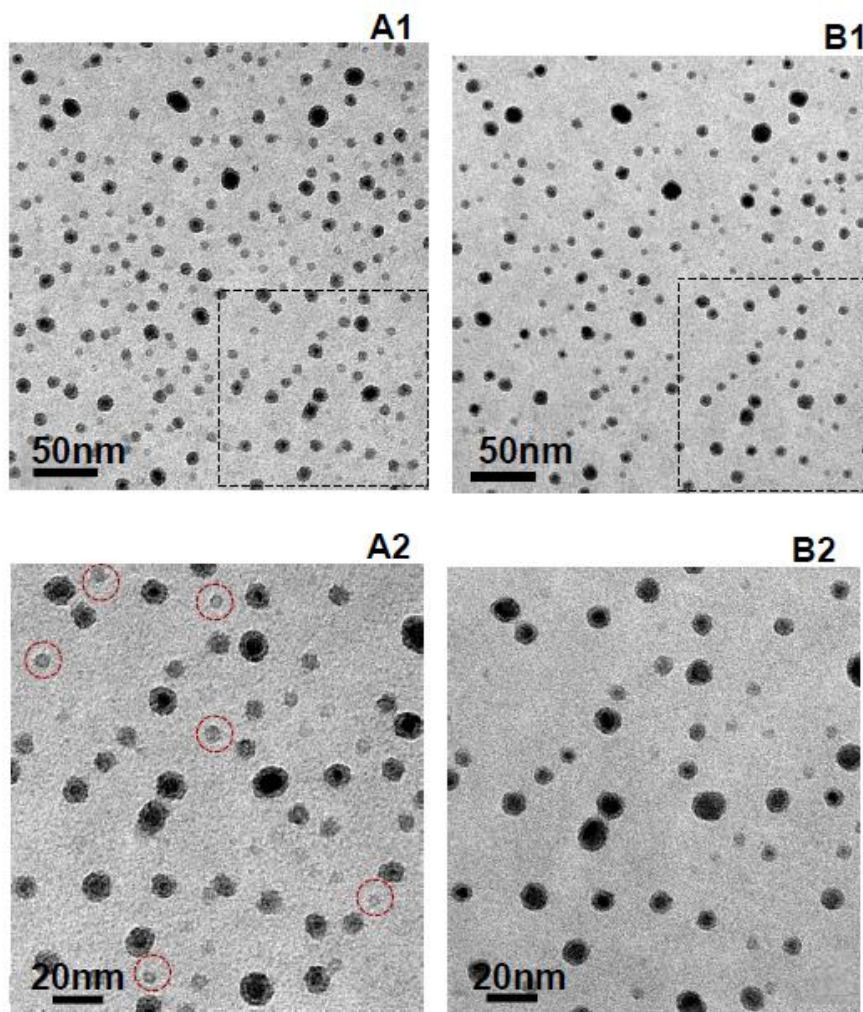


Figure 3.16: Bright-field TEM images of model catalyst reduced-passivated (A1 & A2) and after exposure to FTS conditions & passivation (B1 & B2). The box frame in images A1 and B1 indicate the specific areas that have been magnified to produce images A2 and B2 respectively. Red dashed circles indicate particles which have been lost during FTS treatment.

3.7. References

- [1] <http://www.sasol.com>, Sasol Financial Report July–December 2010.
- [2] N. E. Tsakoumis, M. Rønning, Ø. Borg, E. Rytter, A. Holmen, *Catal. Today*, 154 (2010) 162–182
- [3] A. M. Saib, D. J. Moodley, I. M. Ciobîcă, M. M. Hauman, B. H. Sigwebela, C. J. Weststrate, J. W. Niemantsverdriet, J. van de Loosdrecht, *Catal. Today* 154 (2010) 271–282.
- [4] G. Kiss, C. E. Kliewer, G. J. DeMartin, C. C. Culross, J. E. Baumgartner, *J. Catal.* 217 (2003) 127–140.
- [5] G. Jacobs, P. M. Patterson, Y. Zhang, T. Das, J. Li, B.H. Davis, *Appl. Catal. A* 233 (2002) 215–226.
- [6] G. P. Jacobs, M. Patterson, T. Das, M. Luo, B. H. Davis, *Appl. Catal. A* 270 (2004) 65–76.
- [7] T. K. Das, G. Jacobs, P. M. Patterson, W. A. Conner, J. Li, B. H. Davis, *Fuel* 82 (2003) 805–815.
- [8] D. Pena, A. Griboval-Constant, F. Diehl, V. Lecocq, A. Y. Khodakov, *ChemCatChem*, 5 (2013) 728–731.
- [9] C. J. Bertole, C. A. Mims, G. Kiss, *J. Catal.* 210 (2002) 84–96.
- [10] G. -Z. Bian, N. Fujishita, T. Mochizuki, W. -S. Ning, M. Yamada, *Appl. Catal. A* 252 (2003) 251–260.
- [11] A. Tavasoli, R. M. Malek Abbaslou, A. K. Dalai, *Appl. Catal., A* 346 (2008) 58–64
- [12] A. Tavasoli, M. Irani, R.M. Malek Abbaslou, M. Trépanier, A.K. Dalai, *Can. J. Chem. Eng.* 86 (2008) 1070–1080.
- [13] A. Tavasoli, M. Trépanier, A.K. Dalai, N. Abatzoglou, *J. Chem. Eng. Data* 55 (2010) 2757–2763.
- [14] W. Zhou, J. Chen, K. Fang, Y. Sun, *Fuel Process. Technol.* 87 (2006) 609–616.

Chapter 3

- [15] G. L. Bezemer, T. J. Remans, A. P. van Bavel, A. I. Dugulan, *J. Am. Chem. Soc.* 132 (2010) 8540-8541.
- [16] M. Rønning, N. E. Tsakoumis, A. Voronov, R. E. Johnsen, P. Norby, W. van Beek, Ø. Borg, E. Rytter, A. Holmen, *Catal. Today* 155 (2010) 289-295.
- [17] H. Karaca, J. Hong, P. Fongarland, P. Roussel, A. Griboval-Constant, M. Lacroix, K. Hortmann, O.V. Safonova, A.Y. Khodakov, *Chem. Commun.* 46 (2010) 788–790.
- [18] H. Karaca, O. V. Safonova,, S. Chambrey, P. Fongarland, P. Roussel, A. Griboval-Constant, M. Lacroix, A. Y. Khodakov , *J. Catal.* 277 (2011) 14–26.
- [19] M. Sadeqzadeh, H. Karaca, O.V. Safonova, P. Fongarland, S. Chambrey, P. Roussel, A. Griboval-Constant, M. Lacroix, D. Curulla-Ferré, F. Luck, A. Y. Khodakov, *Catal. Today* 164 (2011) 62-67.
- [20] J. van de Loosdrecht, B. Balzhinimaev, J. -A. Dalmon, J. W. Niemantsverdriet, S. V. Tsybulya, A. M. Saib, P. J. van Berge, J. L. Visagie, *Catal. Today* 123 (2007) 293-302.
- [21] A. M. Saib, A. Borgna, J. van de Loosdrecht, P. J. van Berge, J.W. Niemantsverdriet, *Appl. Catal. A: Gen.* 312 (2006) 12-19.
- [22] C. H. Bartholomew, *Appl. Catal. A* 212 (2001) 17–60.
- [23] C. H. Bartholomew, in: B. Delmon, G.F. Froment (Eds.), *Catalysis Deactivation*, *Stud. Surf. Sci. Catal.*, Vol. 88, Elsevier, Amsterdam, 1994, p. 1-16.
- [24] R. J. Farrauto, C.H. Bartholomew, *Fundamentals of Industrial Catalytic Processes*, Chapman & Hall, Kluwer Academic Publishers, London, 1997 (Chapter 5).
- [25] M. D. Argyle, T. S. Frost, C. H. Bartholomew, *Top Catal* 57 (2014) 415-429
- [26] C.H. Bartholomew, *Appl. Catal. A* (1993) 107, 1–57.
- [27] P. Wynblatt, N. A. Gjostein, *Acta Metall.* 24 (1976) 1165-1174.
- [28] C. T. Campbell, S. C. Parker, D. E. Starr, *Science* 298 (2002) 811-814.
- [29] E. Ruckenstein, B. Pulvermacher, *J. Catal.* 29 (1973) 224.
- [30] B. K. Chakraverty, *J. Phys. Chem. Solids* 28 (1967) 2401-2412.
- [31] P. Wynblatt, N. A. Gjostein, *Prog. Solid State Chem.* 9 (1975) 21.

- [32] A. K. Datye, Q. Xu, K. C. Kharas, J. M. McCarty, *Catal. Today* 111 (2006) 59-67.
- [33] M. Sadeqzadeh, J. Hong, P. Fongarland, D. Curulla-Ferré, F. Luck, J. Bousquet, D. Schweich, A. Y. Khodakov, *Ind. Eng. Chem. Res.* 51 (2012) 11955-11964.
- [34] R. Finsy, *Langmuir* 20 (2004) 2975–2976.
- [35] C. G. Granqvist, R. A. Buhrman, *J. Catal.* 42 (1976) 477-479.
- [36] C. G. Granqvist, R. A. Buhrman, *J. Appl. Phys.* 47 (1976) 2200–2219.
- [37] S. E. Wanke, *J. Catal.* 46 (1977) 234–237.
- [38] S. B. Simonsen, I. Chorkendorff, S. Dahl, M. Skoglundh, J. Sehested, S. Helveg, *J. Am. Chem. Soc.* 132 (2010) 7968-7975.
- [39] S. B. Simonsen, I. Chorkendorff, S. Dahl, M. Skoglundh, J. Sehested, S. Helveg, *J. Catal.* 281 (2011) 147-155.
- [40] G. S. Parkinson, Z. Novotny, G. Argentero, M. Schmid, J. Pavelec, R. Kosak, P. Blaha & U. Diebold, *Nature Mater.* 12 (2013) 724-728.
- [41] P. C. Thüne, C. J. Weststrate, P. Moodley-Gengan, A. M. Saib, J. van de Loosdrecht, J. T. Miller, J. W. Niemantsverdriet, *Catal. Sci. Technol.* 1 (2011) 689-697.
- [42] P. C. Thüne, J. W. Niemantsverdriet, *Surf. Sci.* 603 (2009) 1756–1762.
- [43] P. Moodley, F. J. E. Scheijen, J. W. Niemantsverdriet, P. C. Thüne, *Catal. Today*, 154 (2010) 142-148.
- [44] P. Moodley, J. Loos, J. W. Niemantsverdriet, P. C. Thüne, *Carbon*, 47 (2009) 2002-2013.
- [45] P. L. J. Gunter, J. W. Niemantsverdriet, F. H. Ribeiro, G. A. Somorjai, *Catal. Rev. – Sci. Eng.* 39 (1997) 77.
- [46] C. J. Weststrate, M. M. Hauman, D. J. Moodley, A. M. Saib, E. van Steen, J. W. Niemantsverdriet, *Top Catal.* 54 (2011) 811–816.
- [47] Rasband, W.S., ImageJ, U. S. National Institutes of Health, Bethesda, Maryland, USA, <http://imagej.nih.gov/ij/>, 1997-2012.

Chapter 3

- [48] J. P. den Breejen, J. R. A. Sietsma, H. Friedrich, J. H. Bitter, K. P. de Jong, J. Catal. 270 (2010) 146–152.
- [49] N. P. Barradas, C. Jeynes, Nucl. Instrum. Methods Phys. Res. B 266 (2008) 1875-1879.
- [50] C. R. Brundle, T. J. Chuang, D. W. Rice, Surf. Sci. 60 (1976) 286-300.
- [51] L. B. Backman, A. Rautiainen, M. Lindblad, O.Jylha, A.O.I. Krause, M. Lindblad, Appl Catal. A: General 208 (2001) 223–234.
- [52] A. M. Saib, A. Borgna, J. van de Loosdrecht, P. J. van Berge, J. W. Niemantsverdriet, J. Phys. Chem. B 110 (2006) 8657-8664.
- [53] N. E. Tsakoumis, R. Dehghan-Niri, M. Rønning, J. C. Walmsley, Ø. Borg, E. Rytter, A. Holmen, Appl. Catal. A 479 (2014) 59.
- [54] T. W. Hansen, A. T. DeLaRiva, S.R. Challa, A. K. Datye, Acc. Chem. Res. 46 (2013) 1720.
- [55] S. R. Challa, A. T. Delariva, T. W. Hansen, S. Helveg, J. Sehested, P. L. Hansen, F. Garzon,, A. K. Datye, J. Am. Chem. Soc. 133 (2011) 20672.
- [56] A. DeLaRiva, Sintering of Ni/MgAl₂O₄ catalyst *via* in situ TEM, Ph.D. Dissertation, University of New Mexico, 2010.
- [57] J. Wilson, C. de Groot, J. Phys. Chem. 99 (1995) 7860.
- [58] M. Agnelli, M. Kolb, C. Miradatos, J. Catal. 148 (1994) 9.
- [59] A. A. Blanchard, Chem. Revs. 21 (1937) 3.
- [60] F. Behafarid, B. Roldan Cuenya, Top Catal 56 (2013) 1542.
- [61] Y. Fukamori, M. König, B. Yoon, B. Wang, F. Esch, U. Heiz, U. Landman, ChemCatChem 5 (2013) 3330.
- [62] G. L. Bezemer, J. H. Bitter, H. P. C. E Kuipers, H. Oosterbeek, J. E. Holewijn, X. Xu, F. Kaptein, A. J. van Dillen, K. P de Jong, J. Am. Chem. Soc. 128 (2006) 3956-3964.
- [63] L. A. Richard, P. Moreau, S. Rugmini, F. Daly, Appl. Catal. A:Gen 464-465 (2013) 200-206.

4

The role of carboxylic acids in cobalt Fischer-Tropsch synthesis catalyst deactivation

4.1. Introduction

4.1.1. Carbon deposition during Cobalt Fischer-Tropsch synthesis

Build-up of carbonaceous species on the catalyst during Fischer-Tropsch synthesis (FTS) can negatively influence activity over an extended reaction time. The possible effects could be blocking of active sites, formation of bulk or surface carbides and pore blockage resulting in mass transfer limitations. Moodley *et al.* reviewed the role of carbon in Co FTS catalyst deactivation [1,2]. The types of carbon identified on spent catalyst include (i) surface carbidic species (referred to as atomic carbon) and (ii) subsequent reactions with FTS intermediates and (iii) polymeric carbon (which refers to hydrogen-lean chains of carbon atoms connected by covalent bonds). Temperature-programmed hydrogenation mass spectrometry (TPH-MS) data, carried out on spent Co/Pt/Al₂O₃ FTS catalyst, exhibited three main methane peaks (Figure 4.1) which were assigned to atomic carbon, residual wax in the pores of the alumina support and polymeric carbon [2-5].

The polymeric carbon content, determined using TPH/TPO data, was found to increase with the time that the catalyst was used (i.e. time-on-line, TOL), with a 180 day old spent catalyst containing ~2wt% of polymeric carbon [2]. Based on the Co loading and dispersion, this quantity of polymeric carbon was deduced to be the equivalent of four carbon atoms per surface cobalt atom. This significant quantity of deposited carbon led to the conclusion that only a portion of this carbon could be located on the metal phase resulting in active site blocking. Energy-filtered transmission electron

microscopy (EFTEM) identified that polymeric carbon was present on both the cobalt and the alumina support. The support-bound carbon was postulated to be the result of carbon spillover from the metal onto the support [6].

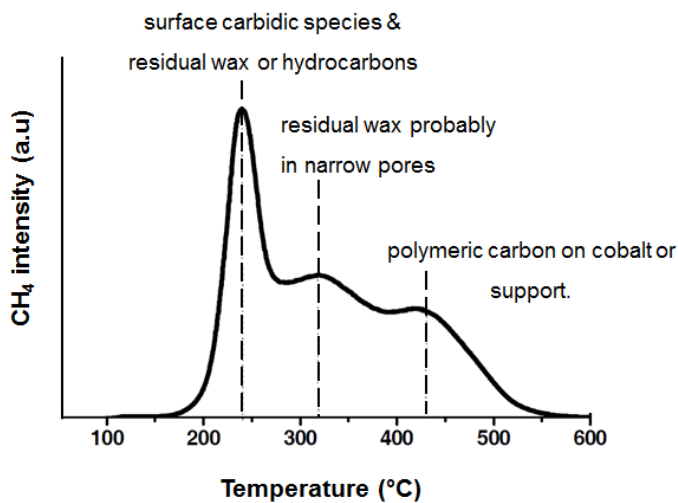


Figure 4.1: TPH-MS CH_4 peaks of a wax extracted spent $\text{Co/Pt/Al}_2\text{O}_3$ FTS catalyst removed from a slurry reactor operated at commercially relevant FTS conditions. Adapted from Moodley *et al.* [1].

H_2 chemisorption experiments showed a correlation between loss of metal surface area and an increase in polymeric carbon with time on line [2]. The presence of polymeric carbon rather than sintering seemed to be contributing to this loss in surface area, over long reaction times, since hydrogen treatments (to 500°C) to remove this polymeric carbon restored the metal surface area capacity to some extent. A regeneration treatment (to 300°C in O_2) of the spent catalyst to remove polymeric carbon, resulted in a 90% recovery of FTS activity. Thus, it was concluded that polymeric carbon could contribute to longer term deactivation in extended runs of FTS.

Chapter 4

In a later study, Pena *et al.* deduced that, in addition to sintering, strongly adsorbed hydrocarbons species and amorphous polymeric carbon plays a significant role in deactivation of a Co/Al₂O₃ FTS catalyst [7]. Weststrate *et al.* showed that polymeric carbon, formed *via* an ethylene treatment (260°C, 3h) over a fresh Co/Al₂O₃ catalyst, was indeed detrimental for catalyst activity [8]. The FTS activity of this catalyst (with carbon deposited) demonstrated activity close to that of a spent catalyst of ~100 days of FTS.

Earlier work by Weststrate *et al.* investigated the surface chemistry of carbon on a cobalt surface by dosing ethylene and acetylene to a single crystal Co (0001) surface in a scanning tunneling microscopy (STM) study [9]. Mono-atomic step edges on the Co (0001) surface were observed to be the nucleation points for small graphene islands [9]. This polymeric-type of carbon was suggested to form *via* a side reaction to FTS, whereby acetylenic surface intermediates undergo cyclo-polymerization. Although acetylenic intermediates are not typically found in the Co low temperature FTS product spectrum, Density Functional Theory (DFT) calculations together with energetic parameters obtained experimentally on Ni and Co surfaces, provided evidence that alkynes (C₂H_x and C₃H_x) are the most stable adsorbates on a close-packed Co metal surface [8]. Since long chain products are produced during FTS, terminal alkynes of various chain length were envisaged to be incorporated into the aromatic structure, forming compounds known as asphaltenes [8]. The high reactivity of acetylenic species on a cobalt metal surface, led to the conclusion that these alkyne species could be responsible for the formation of both aromatic and non-aromatic polymeric carbon during FTS [8].

In more recent work by Pinard *et al.* the chemical nature of carbon species on spent Co-Ru/Al₂O₃ FTS catalyst was determined [17]. Carbon on spent catalyst (after wax removal by N₂ stripping) was extracted and found to contain carboxylic acids and alcohols. The carboxylic acids were detected using TPH-IR and found to be resistant to a hydrogen treatment (up to 600°C in 10% H₂/Ar). This led to the postulation that carboxylic acids and alcohols can be added to the list of carbon species detected during TPH-MS on spent catalyst (Table 4.1) [2]. Pinard *et al.* found that carboxylic acids and alcohols were removed at temperatures of 320-330°C and 275-290°C respectively during TPH-MS (Table 4.1) [17].

Table 4.1: TPH-MS methane peaks and assigned carbon species reported by Pinard *et al.* [17] and Moodley *et al.* [2]

Possible carbon species on spent catalyst	TPH-MS methane peak T (°C) ^a	
	Pinard <i>et al.</i> [17]	Moodley <i>et al.</i> [2]
Surface carbidic species (atomic carbon)	260-270°C	250
Hydrocarbons (alcohols)	275-290°C	
Hydrocarbons (carboxylic acids)	320-330°C	
Residual wax (in small support pores)		330
Polymeric carbon on cobalt or support	420-460°C	445

^aTPH-MS studies (Ref [2] & [17]) were carried out under identical reaction conditions.

4.1.2. Carboxylic acids produced in FTS

FTS produces not only the desired hydrocarbons, but also water and oxygenated compounds such as carboxylic acids, alcohols, esters and

ketones [10,11]. Oxygenates are unwanted side-products in low-temperature Co-catalyzed FTS which is geared towards production of long chain paraffinic waxes. For Fe-catalyzed FTS some specific oxygenates are in fact valuable commodities [12]. Carboxylic acids typically comprise a very small quantity of the FTS liquid products (e.g. 0.05 wt% acetic acid & 0.01 wt% propanoic acid [13]). Typically, acetic acid is found to be the most abundant of the carboxylic acids produced [14,15]. Short chain oxygenates are predominantly found in the FT product water, while less soluble (long chain) oxygenates are found in the hydrocarbon phases.

4.1.3. Oxygenated compounds on spent Co FTS catalyst

Oxygenates can be part of the composition of carbon which is deposited on the catalyst during FTS. Pena *et al.* detected branched fatty acids (C7-C28) and α -alkyl cinnamic aldehydes (C12 – C32) when the organic compounds were extracted from spent Co/Al₂O₃ catalyst and analyzed using GC-MS (FTS at 220°C, H₂/CO:3/1, 20 bar) [16]. FTIR absorption peaks corresponding to carboxylic acids were observed, in particular, after FTS at relatively higher CO conversion (~65-70% initial conversion) [16].

Pinard *et al.* analyzed the carbon species on spent Co-Ru/Al₂O₃ FTS catalyst [17]. Carbon extracted from the spent catalyst was found to consist of both carboxylic acids (~C4-C24 on a 7 day old catalyst) and alcohols (~C12-C32 on a 7 day old catalyst). TPH-IR indicated that complete removal of carboxylate species required temperatures above 600°C. Carboxylic acids (C1-C7 acids) adsorbed on pure γ -Al₂O₃ showed IR frequencies in the same IR region (corresponding to O-containing

molecules) as those of spent Co/Ru/Al₂O₃ FTS catalyst. Organic acids were deduced to adsorb strongly on the support or on the metal, implying a significant contribution of carboxylic acids to deactivation in the case of adsorption on the metal.

4.1.4. Carbon formation from oxygenated compounds

Acid can adsorb on pure γ -Al₂O₃, as was reported by Hasan *et al.*, where *in-situ* FTIR spectroscopy showed that both dissociative and non-dissociative adsorption of acetic acid occurs, with the former producing adsorbed acetate species (stable up to 400°C on pure Al₂O₃) [18]. Lewis acidic sites on oxidic support surfaces adsorb carboxylic acid while basic sites can enable condensation reactions which produce carbon species. For instance, thermal treatment of oxide compounds, such as TiO₂, CeO₂, in the presence of acetic acid results in a ketonization reaction which produces acetone [18]. Acetone can subsequently produce light, gaseous carbonaceous compounds such as mesityl oxide (C₆H₁₀O), isobutylene (C₄H₈) and methane (CH₄) *via* condensation reactions over the support [19-21].

Oxygenates are commonly known to form carbon (also referred to as coke) on steam reforming catalysts. Steam reforming of acetic acid over Co/Al₂O₃ can result in thermal decomposition of acid [22] as reported by Hu *et al.* [23]. Reactions using pure acetic acid on Co/Al₂O₃ catalyst (1h, 400°C) produced hydrogen, acetone, ketene, methane, CO and significant carbon formation [23]. The Co/Al₂O₃ catalyst deactivated (in the steam reforming reaction) severely over time (100h, 400°C, 1 bar, steam-to-acid ratio: 7.5).

Chapter 4

TGA indicated significant carbon formation on the catalyst, which was postulated to arise either from the Boudouard reaction (of the CO product) or reaction between acetone intermediates [24,25]. Coke formed directly from acid decomposition was deduced to be unlikely at the selected reaction conditions [26]. Both oxidation of metal (determined by XRD) and coke formation was proposed to be responsible for severe catalyst deactivation. Interestingly, the production of CO, acetone and ketene were not affected while the catalyst deactivated (i.e. during carbon build-up and oxidation). This implied that the ketonization and dehydration reactions were being catalyzed by the alumina support sites and did not require the metal sites.

Vagia *et al.* investigated the feasibility of reforming oxygenated compounds used thermodynamic calculations [26]. In their theoretical study, carbon formation showed highest selectivity at low steam-to-acid ratio (0.5) and showed a decreasing trend with temperature until being completely suppressed above 723°C [26]. The effect of pressure (1-20 bar) was investigated at constant steam-to-carbon ratio (3) and was found not to significantly affect carbon formation.

4.1.5. Research objective

Polymeric carbon deposited on Co/Al₂O₃ catalyst can negatively impact FTS activity. Carbon on spent Co/Al₂O₃ FTS catalyst has been found to contain oxygenated compounds such as alcohols and carboxylic acids. Oxygenated compounds could therefore be potential precursors for carbon deposited on Co FTS catalyst. This carbon could be a result of oxygenate

decomposition over the metal or support surface. Oxygenates could also be strongly adsorbed on Al₂O₃ support or form metal-carboxylate compounds and consequently affect Co FTS catalyst performance. The primary objective of this study is to determine whether carboxylic acids contribute to catalyst deactivation: This is achieved by investigating:

- (i) The location (Co metal and/or γ -Al₂O₃ support) of the carboxylate species identified on spent catalyst.
- (ii) The feasibility of polymeric carbon formation due to carboxylic acid decomposition on Co/Al₂O₃ FTS catalyst.
- (iii) The effect of acid co-feeding during Co-catalyzed FTS at realistic conditions.

4.2. Materials and methods

4.2.1. Materials

Acids

Acetic acid (99%) and octanoic acid (99%) were purchased from Sigma-Aldrich and used as received.

Alumina and cobalt catalyst

γ -Al₂O₃ support material was supplied by Sasol Germany. Fresh Co/Pt/ γ -Al₂O₃ catalyst (20 wt% Co, 0.05 wt% platinum) was obtained from Sasol. The catalyst was prepared by slurry impregnation of the γ -Al₂O₃

Chapter 4

support with an aqueous cobalt nitrate and ammonium platinum nitrate solution. After impregnation and drying, the catalyst precursor was calcined (at 250°C in air) and this procedure was repeated to achieve the desired metal loading [27-30]. The catalyst was reduced (in pure H₂ at 425°C) and embedded in wax (Sasol H1 wax, density 0.94 g/cm³) before FTS testing.

Spent FTS catalyst

Spent Co/Pt/Al₂O₃ FTS catalyst samples were supplied by Sasol. The samples were removed from the Sasol Catalyst Testing Reactor in Sasolburg, South Africa, which is a slurry bubble column FTS reactor operated at commercially relevant conditions i.e. 230°C, 20 bar, H₂ + CO conversion 50-70%, feed gas composition of 50–60 vol% H₂ and 30–40 vol% CO. Samples were removed at various time intervals (including 5 and 90 day old samples reported in this study) and contained a protective wax layer. Before further analysis, a wax extraction procedure was carried out according to the procedure described by Moodley *et al.* [2].

Acids adsorbed on γ -Al₂O₃

Acetic acid was adsorbed on γ -Al₂O₃ by adding (10 ml) of an aqueous acetic acid solution (5 vol %, room temperature) to γ -Al₂O₃ (2g) which was pre-dried at 120°C for 10 mins. The resulting suspension was stirred (1 min) before the excess solution was filtered off and the sample dried (for 10 min) at 120 °C in air. Octanoic acid was adsorbed on γ -Al₂O₃ by adding (10 ml) of an octanoic acid in methanol solution (5 vol %, room temperature) to γ -Al₂O₃ (2g) which was pre-dried at 120°C for 10 mins. Methanol was used a solvent for this acid solution instead of water, due to the low solubility of octanoic acid in water.

4.2.2. Methods

4.2.2.1. Acetic acid addition to alumina and pre-reduced cobalt catalyst at 230°C under H₂/CO

Acetic acid saturated synthesis gas was obtained by flowing H₂ (10 ml(NTP)/min), CO (5ml(NTP)/min) and Ar (90 ml(NTP)/min) gas through a stainless steel saturator filled with pure (99%) acetic acid (25 ml) which was kept at room temperature (~0.02 bar vapor pressure of acetic acid at RT as determined in Ref [31]).

The acetic acid saturated gas was led over the sample of either γ -Al₂O₃ or Co/Pt/Al₂O₃ catalyst (100mg). The sample was loaded and enclosed with glass wool in a quartz glass reactor tube (4mm internal diameter). The reactor tube was contained in an oven that was used to heat the sample evenly.

The reactor tube contained two separate inlet connections, one for acid saturated gas and the other for acid-free gas. All treatments were carried out at atmospheric pressure. The Co-catalyst sample was pre-reduced at 425°C (5°C/min, 4h) under 10% H₂/Ar, followed by cooling to 230°C in the same gas mixture. Once 230°C was reached, the feed gas was changed to acid-saturated H₂/Ar gas and CO was introduced to the gas mixture at this point as well. The samples were exposed to this gas mixture for 15 min, after which time the feed gas was changed back to acid-free H₂/Ar gas, which was flowed for 1h at 230°C to ensure acid was removed from the reactor tube (as monitored by MS). The sample was then cooled to room temperature under H₂/Ar gas flow.

Chapter 4

In the cases where in-situ temperature programmed (TP) experiments coupled with mass spectrometry (MS) was carried out, samples were cooled in H₂/Ar and kept under H₂/Ar gas flow at room temperature until the TPH-MS measurement was carried out. Those measurements were carried out by heating the sample to 800°C (5°C/min) using 10% H₂/Ar (50 ml(NTP)/min). The evolving gases were monitored using a Omnistar™ Thermostar™ GSD 320 mass spectrometer.

In the cases where ex-situ TPH-MS, XPS and ATR-IR was carried out, samples were slowly exposed to air after cooling to room temperature. This was done by stopping the gas flow and opening the narrow inlet and outlet openings of the reactor which enabled air to slowly replace the H₂/Ar mixture in the reactor tube. Samples were then unloaded in air and used for measurements.

4.2.2.2. Temperature programmed (TP) techniques coupled with mass spectrometry (MS)

For ex situ TP-MS measurements, samples were packed into a quartz glass reactor tube (4mm ID) and enclosed with glass wool. Measurements were carried out by heating samples to 800°C (5°C/min) using 10% H₂/He (50 ml(NTP)/min total flow) in the case of TPH-MS and pure He (50 ml(NTP)/min) in the case of TPD-MS . The evolving gases were monitored using a Balzers QMA 400 mass spectrometer.

TPD-MS coupled with GC-MS was carried out on sample of acetic acid adsorbed on γ -Al₂O₃.² The sample (700 mg) was packed in a fixed bed

² TPD-GC-MS experiments carried out by Jack Fletcher at the Eindhoven University of Technology.

reactor (catalyst bed 800 by 5mm) and enclosed with SiC (using a quantity that filled the rest of the catalyst bed volume). The reactor was heated under Ar (50 ml(NTP)/min) to 500°C (2°C/min). GC-MS was carried out using a Varian CP-Pora-BondQ column (L=50m, ID 0.32mm) with He as a carrier gas and a sampling temperature program of 240°C (5°C/min) for 10 min.

4.2.2.3. ATR-IR

Attenuated total reflectance infrared spectroscopy (ATR-IR) spectra were recorded using a Nicolet Smart Golden gate instrument equipped with a diamond crystal (cutoff at 800 cm^{-1}). Measurements were carried out in transmission mode using the appropriate background with a resolution of 2 cm^{-1} over 128 scans.

4.2.2.4. XPS

X-ray photoelectron spectroscopy (XPS) spectra were measured using a K-alpha spectrometer equipped with a monochromatic AlK α x-ray source (1486.6 eV) operated at 150W (15kV and 10mA emission current). The $\gamma\text{-Al}_2\text{O}_3$ powder samples were filled into pots on a copper plate, which served as the XPS sample holder. During measurements, the pressure in the analysis chamber was $<10^{-8}$ mbar. Binding energies were calibrated using the Al2p peak of $\gamma\text{-Al}_2\text{O}_3$ at 74.4 eV [32]. For analyses of C1s/Al2p peak intensity ratios, peak fitting (using a Shirley background correction & atomic sensitivity factors for each element included) was carried out using the CasaXPS software version 2.3.15. The relative peaks of the C1s signals and the Al2p signal was quantified and used to determine C1s/Al2p peak intensity ratios.

4.2.2.5. SEM

Scanning electron microscopy (SEM) was performed using a Philips environmental scanning electron microscope FEI XL-30 ESEM FEG in high-vacuum mode at 2kV voltage. The alumina samples were deposited onto a silica wafer containing a layer of colloidal silver dispersed in toluene (supplied by Electron Microscopy Sciences).

4.2.2.6. TGA

Thermo-gravimetric analysis (TGA) was carried out using TGA Q5000 V3.15 Build 263 apparatus.³ Samples were heated from room temperature to 700°C (5°C /min) under He (25 ml(NTP/min)).

4.2.2.7. FTS testing

FTS testing was carried out using a Co/Pt/Al₂O₃ catalyst in a continuous stirred-tank reactor (volume 1L) at commercially relevant FTS conditions i.e. 230°C, ~20 bar, conversion between 50-70% (constant conversion was targeted), feed gas composition of ~50 vol% H₂, 30 vol% CO and 20% inert gas (Ar), reactor P_{H₂O} of ~4-6 bar.⁴ To enable a comparison on the activity profiles between two different FTS runs, activity was first calculated as mol(CO converted)/g(catalyst)/h and then a FT activity ratio was determined. For the FTS experiments with acid co-feeding, an HPLC pump was used to flow (~0.1 mol/h) of an acetic acid (20-200 ppm) in ethanol

³ TGA experiments carried out by Veronica Patterson at Sasol Technology, South Africa.

⁴ FTS testing carried out by Herman Preston at Sasol Technology, South Africa.

solution directly into the reactor using a separate inlet feed line. CO conversion was determined using an online GC-MS with TCD detection.

4.3. Results

4.3.1. ATR-IR of spent Co FTS catalyst

In order to confirm the presence of oxygenated compounds, ATR-IR measurements were carried out on wax-extracted spent Co/ γ -Al₂O₃ FTS catalyst (Figure 4.2). Spent catalyst which is only wax-extracted still contains residual wax that can be trapped in the pores of the support and carbon that is deposited during FTS [2]. Therefore, not only a set of wax-extracted spent catalysts were measured, but also a set of wax-extracted then hydrogen treated (using pure H₂, 5°C/min, 280°C, 6h) and passivated spent catalysts were measured. The spectrum of a reduced fresh catalyst is also measured to compare to spent catalyst samples and to identify the presence of oxygenates on fresh catalyst. This reduced fresh sample was wax-encapsulated and subsequently hydrogen-treated (to 280°C). The background spectra used for each respective IR measurement is listed in the Appendix (Table 4.5).

The IR absorption spectra of two spent catalyst (wax-extracted) samples with relatively short (5 days-on-line) and longer (90 days-on-line) time in the FTS reactor are shown in Figure 4.2. These spent catalysts show peaks in the IR spectral region which correspond to functional groups of oxygen-containing molecules (at ~1409, 1464 and 1548 cm⁻¹) and alkyl-containing molecules (at ~2849 and 2916 cm⁻¹). This provides evidence for the

presence of oxygenated compounds (consisting of C-O and CH groups) on spent catalysts. These findings are in agreement with those of Pinard *et al.* where IR vibrations indicative of oxygenate species were identified on spent Co-Ru/Al₂O₃ FTS catalyst [17]. Although appearing in the regions corresponding to carboxylate (COO⁻) vibrations, the detected vibrational frequencies in the 1400-1550 cm⁻¹ IR region (Figure 4.2) are not unique for only carboxylates, as other oxygenates could give rise to peaks in the same region.

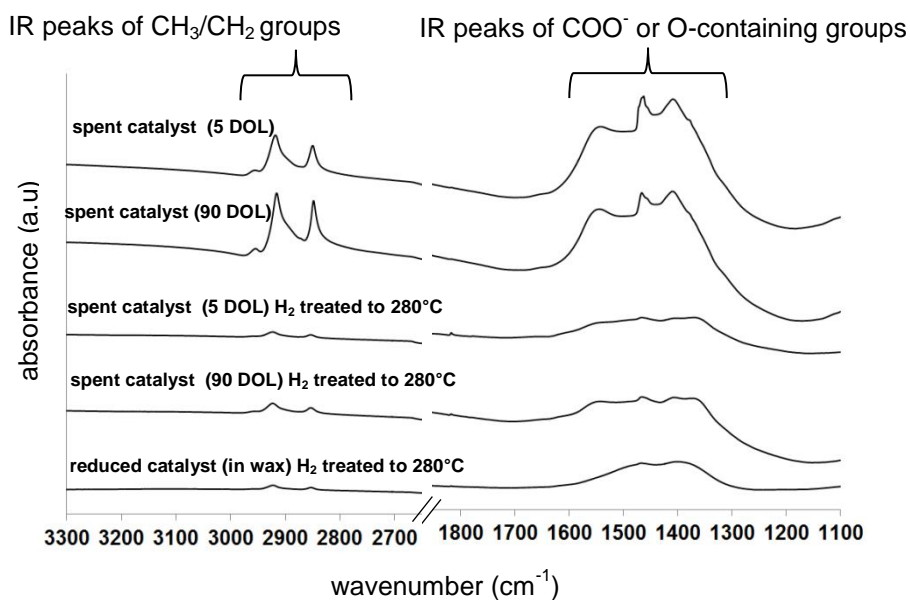


Figure 4.2: Infrared absorption spectra showing the carboxylate (COO⁻) and alkyl (CH_x) region spectra for spent Co FTS catalyst (5 & 90 days-on-line) both wax-extracted and after subsequent H₂ treatment (to 280°C). In addition, a sample of reduced catalyst embedded in wax (& H₂ treated to 280°C in) is measured for comparison.

The presence of absorption peaks corresponding to oxygenate-containing molecules are also detected in the IR spectra of the hydrogen-treated (to 280°C) spent catalysts (Figure 4.2). Therefore, some of the oxygenated compounds detected on spent catalyst are resistant to H₂ up to 280°C, which is above the temperature of Co FTS (200-230°C). Thus, the oxygenated compounds are expected to be adsorbed during Co FTS.

The IR absorption spectra of reduced and hydrogen-treated (to 280°C) fresh catalyst shows broad peaks in the spectral region corresponding to oxygenate-containing compounds (~1390 and 1460 cm⁻¹, Figure 4.2). These oxygenates possibly originate from contaminants in the wax used for embedding the reduced catalyst. This indicates that some oxygenates can already be present prior to FTS. However, this is not expected to account for all of the oxygenate species observed on spent catalyst since oxygenates will be continuously produced during FTS and can therefore accumulate on the catalyst.

4.3.2. ATR-IR of acetic and octanoic acid adsorbed on γ -Al₂O₃

The presence of oxygenate species, resistant to H₂ (to 280°C), on spent Co/ γ -Al₂O₃ FTS catalyst (Figure 4.2) could be due to species that are strongly adsorbed on the γ -Al₂O₃ support. Carboxylate molecules, which contain a nucleophilic carboxylate (COO⁻) group, can be envisaged to have a strong interaction with the aluminum cations (Al³⁺) of γ -Al₂O₃. In fact, Pinard *et al.* reported that carboxylic acids (C1-C7 acids) adsorbed on pure γ -Al₂O₃ showed IR frequencies in the same vibration region (corresponding

Chapter 4

to oxygen-containing molecules) as those detected on spent Co/Ru/Al₂O₃ FTS catalyst.

Carboxylic acids are a major component of the oxygenated compounds produced during FTS, of which acetic acid is typically found in the highest concentration [11-15]. This makes acetic acid a relevant compound to study the interaction of a carboxylate with a Co metal surface and γ -Al₂O₃. Octanoic acid is a carboxylate with a considerably longer carbon chain (C8) compared to acetic acid (C2), making it a useful compound to study the adsorption of carboxylate (with a long carbon chain) on γ -Al₂O₃.

To investigate the adsorption of a carboxylic acid on Co/ γ -Al₂O₃ FTS catalyst, model experiments were carried out using carboxylic acid and pure γ -Al₂O₃ (described in the following section) or a Co metal surface (described later in next section 4.3.3).

Pure γ -Al₂O₃ was impregnated with both short (acetic acid) and longer chain (octanoic acid) carboxylic acid (as described in experimental section 4.2.1). Figure 4.3 shows the IR absorption spectra of the resulting acid-impregnated γ -Al₂O₃ samples as well as the respective pure acid compounds for reference.

The IR absorption spectrum of pure acetic acid shows a sharp peak at $\sim 1710\text{ cm}^{-1}$ attributed to the carboxyl group of the free acid (Figure 4.3). For the sample of acetic acid-impregnated γ -Al₂O₃, the absorption peak of the carboxyl group appears at a lower frequency of $\sim 1580\text{ cm}^{-1}$. This shift in absorption peak suggests that acetic acid is chemisorbed on γ -Al₂O₃, in the form of acetate. This shift in frequency is expected when the oxygen atoms

of the carboxylate group are coordinated to the aluminum cations of $\gamma\text{-Al}_2\text{O}_3$, as this will result in a weaker C-O bond strength and consequently a lower IR frequency. The IR frequencies (Figure 4.3) of acetic acid adsorbed on $\gamma\text{-Al}_2\text{O}_3$ of ~ 1574 , 1469 and 1424 cm^{-1} agree with reported literature values [18,33] assigned to the anti-symmetric carboxylate absorption, symmetric carboxylate absorption and rotational methyl absorption respectively. The IR vibrations which result due to adsorption of acetic acid on $\gamma\text{-Al}_2\text{O}_3$ is further studied using Density Functional Theory (DFT) and discussed in Chapter 5 of this thesis.

For the case of acetic acid adsorbed on $\gamma\text{-Al}_2\text{O}_3$, the acid was impregnated on $\gamma\text{-Al}_2\text{O}_3$ using an aqueous solution before a drying step followed by IR measurement. This means that acetic acid and water are added simultaneously to $\gamma\text{-Al}_2\text{O}_3$ during sample preparation. Since IR shows that acetate is adsorbed (Figure 4.3), this implies that acetic acid competes with water for adsorption sites on $\gamma\text{-Al}_2\text{O}_3$.

For the carboxylate with longer carbon chain length, the IR absorption peak attributed to the carboxyl group shifts from $\sim 1720\text{ cm}^{-1}$ in free octanoic acid to $\sim 1570\text{ cm}^{-1}$ for octanoic-impregnated $\gamma\text{-Al}_2\text{O}_3$ (Figure 4.3). This provides evidence for the adsorption of the longer chain carboxylate on $\gamma\text{-Al}_2\text{O}_3$, in the form of octanoate. The absorption spectrum of octanoic acid shows peaks in the vibration region corresponding to alkyl (CH_3/CH_2) groups [34], which identifies the alkyl chain of octanoate.

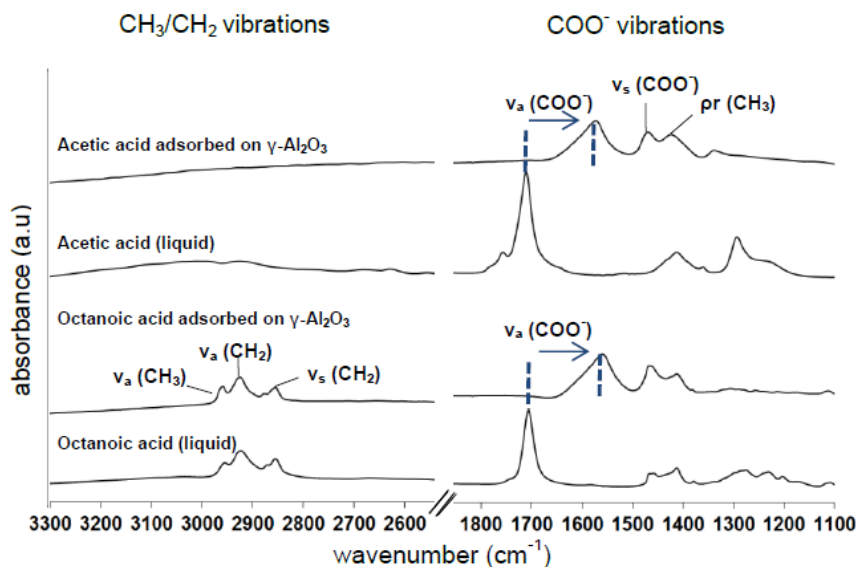


Figure 4.3: ATR-IR of acetate and octanoate adsorbed on $\gamma\text{-Al}_2\text{O}_3$ compared to reference compounds of pure acetic and octanoic acid (liquids).

These findings suggest that both short (acetic acid) and longer chain (octanoic acid) carboxylic acids adsorb on $\gamma\text{-Al}_2\text{O}_3$, as carboxylates. In addition, acetic acid competes with water for adsorption sites on $\gamma\text{-Al}_2\text{O}_3$.

4.3.3. Single crystal Co(0001) experiments using acetic acid

The stability of carboxylate on a Co surface was studied by dosing acetic acid to a Co(0001) single crystal surface in an ultrahigh vacuum (UHV)

experimental setup (see footnote⁵). These experiments were used to determine if carboxylate detected on Co/Al₂O₃ FTS catalyst (using IR) could in fact be due carboxylate located on the Co metal.

Figure 4.4 shows the temperature-programmed desorption spectrum (detecting gas phase products) and the corresponding temperature-programmed work function data (detecting changes on the surface) from an experiment where acetic acid was dosed onto a Co(0001) surface at low temperature.

The TPD spectrum (Figure 4.4a) shows CO and H₂ desorption below 400K (127°C), indicating an acetic acid decomposition process that occurs at relatively low temperature. The work function plot (Figure 4.4b) shows that the decomposition proceeds in a series of reaction steps which all occur below 230°C (the molecular structure of the intermediates after the different steps is beyond the scope of the present study).

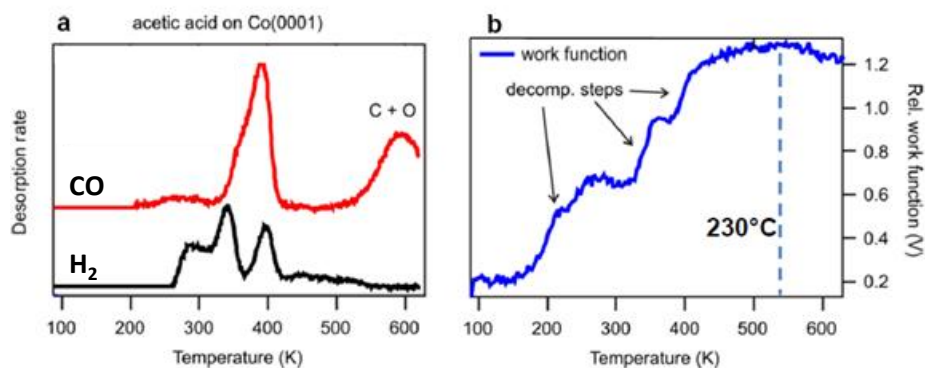


Figure 4.4: (A) TPD and (B) work function plots of acetic acid on Co (0001).

⁵ Ultrahigh vacuum (UHV) experiments were carried out by C.J. Weststrate at the Eindhoven University of Technology.

These findings indicate that acetic acid is thermally unstable on a Co metal surface at FTS temperature. This implies that carboxylate compounds which are strongly bound to spent Co FTS catalyst (detected using IR) are not bound to the metal but instead are adsorbed on the $\gamma\text{-Al}_2\text{O}_3$ support.

4.3.4. SEM of acetic acid adsorbed on $\gamma\text{-Al}_2\text{O}_3$

SEM and BET measurements were carried out to investigate whether the exposure of pure $\gamma\text{-Al}_2\text{O}_3$ to an aqueous acetic acid solution at room temperature (as described in experimental section 4.2.1) influenced the integrity of the support.

Figure 4.5 compares the SEM images of the $\gamma\text{-Al}_2\text{O}_3$ support material before and after exposure to an aqueous solution of acetic acid. The size and shape of the support particles is comparable before and after the acid impregnation and there is no observable deterioration of the support particles. BET measurements (Appendix, Table 4.6) confirm that the support integrity is not compromised by the impregnation treatment, as the surface area and pore volume do not change significantly. These findings imply that the method used to adsorb acid on the support does not cause a deterioration of the structural integrity of the support.

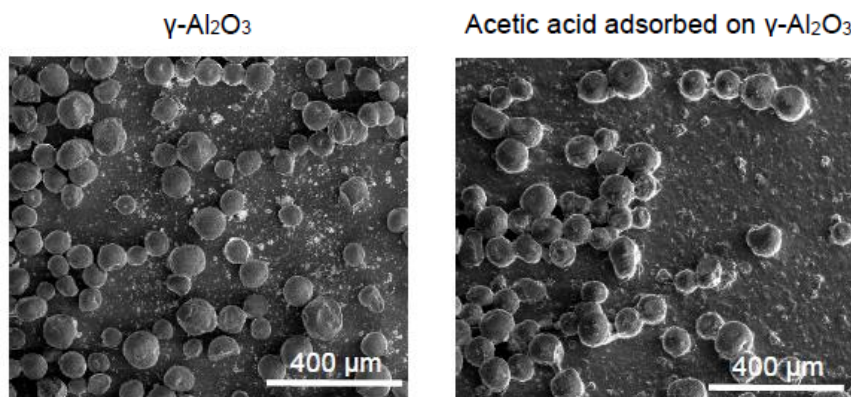


Figure 4.5: SEM images of pure $\gamma\text{-Al}_2\text{O}_3$ and $\gamma\text{-Al}_2\text{O}_3$ impregnated with an aqueous solution of acetic acid at RT.

4.3.5. XPS of acid adsorbed on $\gamma\text{-Al}_2\text{O}_3$

The binding energies of the C1s peaks in an XPS spectrum can differentiate the carbon atom in a carboxyl group from the carbon atom(s) in an alkyl group within the carboxylate molecule. This is because these carbon atoms have a different chemical environment in the molecule. In addition, XPS peak intensities can be used in a quantitative manner to determine the ratio between different types of carbon present on a sample. For instance, in the case of octanoate, a significantly larger peak intensity of the carbon atom of the alkyl group is expected ($\text{C}_7\text{H}_{15}\text{:COO} = 7:1$), while for the case of acetate the relative peak intensities should be the same ($\text{CH}_3\text{:COO} = 1:1$).

Figure 4.6 shows the XPS C1s core level spectra of acetate and octanoate on $\gamma\text{-Al}_2\text{O}_3$ (XPS survey spectra in Appendix Figure 4.16 shows that all expected elements were identified and that no unexpected elements were

detected). For both cases, two distinct peaks are observed at 285.0 and 289.1 eV, which are assigned to the carbon atom(s) in the alkyl group and carbon atom in the carboxyl group respectively.

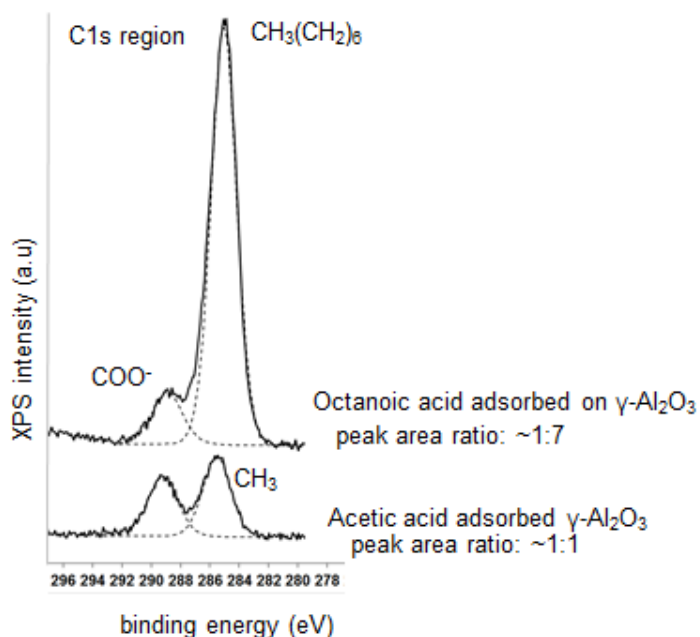


Figure 4.6: XPS C1s region of acetate and octanoate adsorbed on $\gamma\text{-Al}_2\text{O}_3$. Dashed lines (---) indicates the deconvolution of the respective peaks (as described in experimental section 4.2.2.4)

For the case of acetate, the XPS spectrum shows (and peak fitting confirmed) that the peak intensities are approximately equal, as expected ($\text{CH}_3:\text{COO} = 1:1$). For the case of octanoate, the C1s peak intensity due to carbon atoms in the alkyl group was significantly larger, as expected (~ 7 times larger peak area determined by peak fitting of the C1s spectrum)

4.3.6. Thermal stability of acid adsorbed on γ -Al₂O₃: XPS

XPS was used to determine whether octanoate and acetate adsorbed on γ -Al₂O₃ would remain intact during FTS. For this purpose, γ -Al₂O₃ containing adsorbed carboxylate was exposed to model FTS conditions i.e. H₂/CO gas (at 1 bar) at 230°C for 10h.

Specifically the carboxylate carbon peak (binding energy of ~289.1 eV, Figure 4.6) intensities are compared before and after the reaction, since they represent the molecular concentration of either acetate or octanoate. The alkyl peak intensities were unchanged in spectral shape and only changed in relative intensity. Thus, analyses of the carboxylate carbon peak was sufficient to compare molecular concentration of acid adsorbed. The peak intensities are reported as a ratio of C1s_(carboxylate)/Al2p peak intensity to account for variations in total photoelectron counts (total signal intensity) between the measurements.

Figure 4.7 compares the relative amount of carboxylate on γ -Al₂O₃ before and after the treatment. For both acids, the quantity of carboxylate adsorbed was comparable before and after the treatment. This shows that the carboxylates remained strongly adsorbed on γ -Al₂O₃ during exposure to model FTS conditions, probably in their saturation amounts.

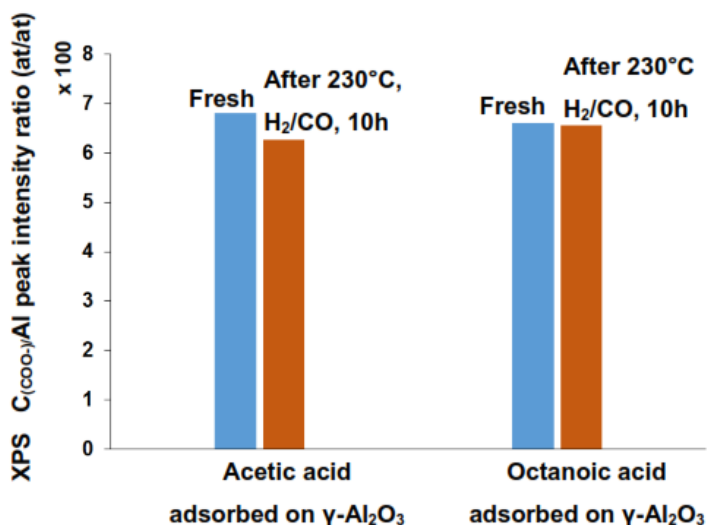


Figure 4.7: XPS C_{1s(carboxyl peak)}/Al_{2p} peak intensity (at/at) ratio comparing acetate and octanoate on γ -Al₂O₃ with the respective samples after exposure to model FTS conditions (i.e. 230°C under H₂/CO (1 bar) for 10h). Peak areas were determined from peak deconvolution carried out using the CasaXPS 2.3.15 software (as described in section 4.2.2.4).

4.3.7. Thermal stability of acetic acid adsorbed on γ -Al₂O₃ studied using TP-MS

TPD-MS was used to study the thermal stability of adsorbed acid on pure γ -Al₂O₃ and the nature of the gaseous products released when the sample is heated. For the case of acetate adsorbed on γ -Al₂O₃, online GC-MS analysis was used to identify the molecular structure of the desorption products and to translate the mass fragments detected by TPD-MS to molecular products. In addition, TPO-MS was used to identify the nature of the carbon deposited a result of thermal treatment of acetate over γ -Al₂O₃.

Figure 4.8 shows the TPD-MS (under pure He) of acetate adsorbed on γ -Al₂O₃. TPD-MS data shows that water desorbs at lower temperatures (100 & 250°C), but the first gaseous products only appear above 300°C (Figure 4.8). Using GC-MS, the major desorption peaks can be identified as acetone (375°C) and carbon dioxide (400°C). Minor products include carbonaceous species, specifically, isobutylene (420°C), propene (490°C) and methane (600°C).

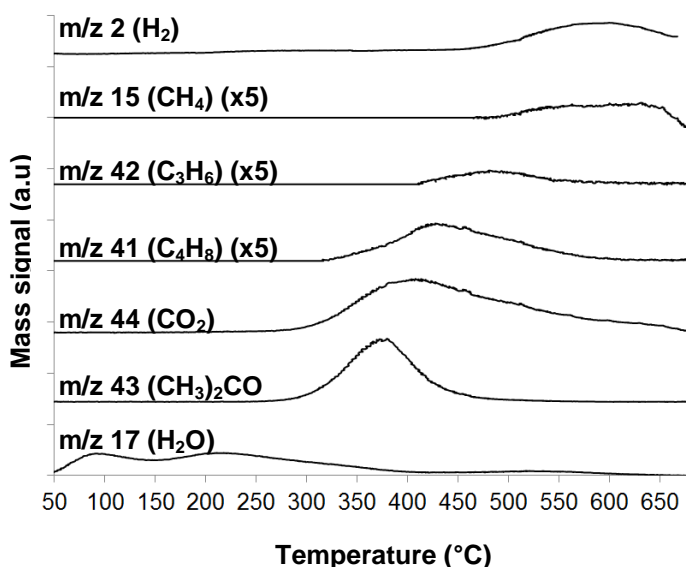


Figure 4.8: TPD-MS spectrum of acetate adsorbed on γ -Al₂O₃, labelled using GC-MS data: (CH₃)₂CO (m/z = 43), CO₂ (m/z = 44), H₂O (m/z = 17), H₂ (m/z = 2), C₄H₈ (m/z = 41), CH₄ (m/z = 15) & C₃H₆ (m/z = 42).

The hydrogen evolution starting around 500°C is deduced to be a result of the thermal treatment of adsorbed acid on γ -Al₂O₃ since it was not observed using a blank γ -Al₂O₃ sample (Appendix

Chapter 4

Figure 4.17). Thermal treatment of adsorbed acetate under a hydrogen atmosphere produces identical results (TPH-MS in Appendix Figure 4.18a).

Figure 4.9. shows the TPD-MS (under pure He) of octanoate adsorbed on γ - Al_2O_3 . As was the case for acetate, water desorbs at relatively lower temperatures (~ 150 - 250°C), while further products are detected above 300°C . In fact, the onset of products due to thermal treatment of adsorbed octanoate is $\sim 100^\circ\text{C}$ higher compared to acetic acid, which indicates that octanoate is more thermally stable on γ - Al_2O_3 . The mass fragments of major (m/z 43 & 44) and minor (m/z 15, 41 & 42) desorption species are comparable to the case of acetate, which suggests that both short and longer chain carboxylates have a similar reaction pathway on γ - Al_2O_3 (however, the exact nature of the desorbed species from octanoate decomposition needs to be monitored using online GC-MS to confirm this). Thermal treatment of adsorbed octanoate under a hydrogen atmosphere produces identical results (TPH-MS in Appendix Figure 4.18b).

The detection of products due to a thermal treatment of carboxylate adsorbed on γ - Al_2O_3 , occurs at temperatures significantly higher (i.e. $>300^\circ\text{C}$) than that of Co FTS (200 - 230°C). This implies that carboxylate decomposition on γ - Al_2O_3 is expected to be slow at Co FTS temperature.

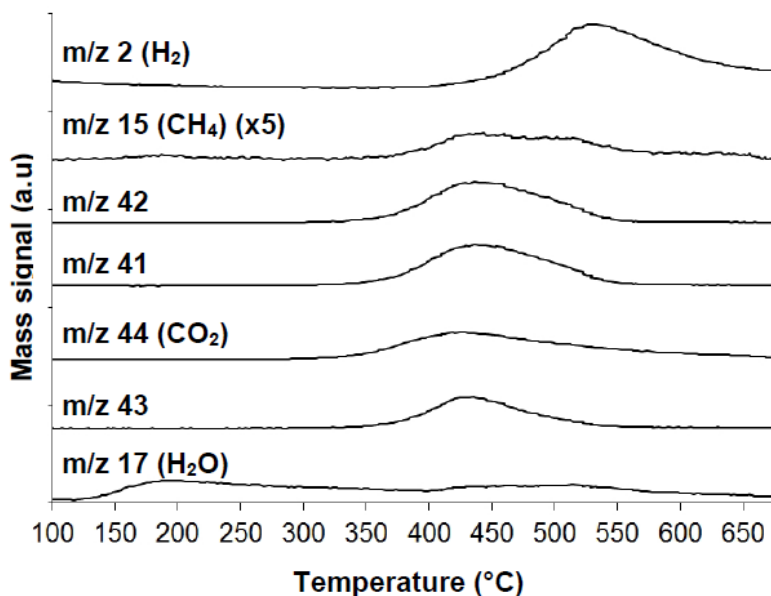


Figure 4.9: TPD-MS spectrum of octanoate adsorbed on γ - Al_2O_3

Carbon is deposited when acid is thermally decomposed over γ - Al_2O_3 . Figure 4.10a shows the image of a sample of acetate adsorbed on γ - Al_2O_3 in a reactor tube after a TPD treatment (700 $^{\circ}\text{C}$ under He) is carried out. The sample is black in color which indicates carbon deposition on γ - Al_2O_3 . The sample returns to its original white color (i.e. the carbon is removed) when a TPO-MS experiment is carried out directly after the TPD treatment (Figure 4.10b).

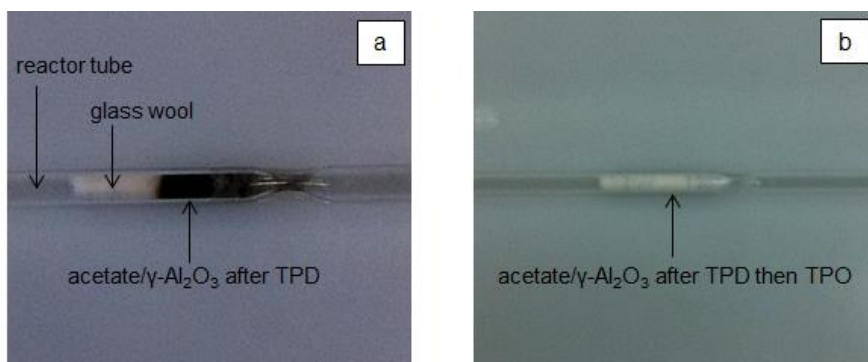


Figure 4.10: Images of a sample of acetate adsorbed on γ -Al₂O₃ in a reactor tube after (a) TPD and after (b) TPD followed directly by TPO.

The evolution of CO₂ (m/z 44) was monitored during the TPO-MS experiment and revealed a broad peak around 400°C (Figure 4.11). Previous work by Moodley *et al.* showed that polymeric carbon on a spent Co/Al₂O₃ FTS catalyst resulted in a TPO-MS peak around 450°C [2]. Therefore, thermal treatment (to 700°C in He) of acetate adsorbed on γ -Al₂O₃ results in polymeric-type carbon formation on pure γ -Al₂O₃.

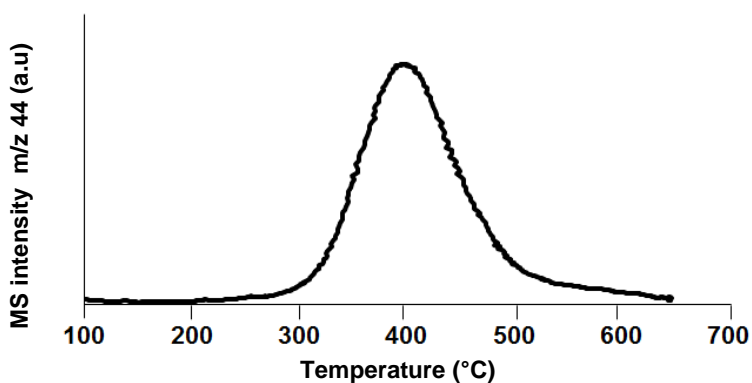


Figure 4.11: TPO-MS spectrum of acetate adsorbed on γ -Al₂O₃ carried out directly after TPD.

4.3.8. Saturation coverage of acids adsorbed on γ -Al₂O₃ studied using TGA

TGA analyses were performed to estimate the saturation coverage of acetate and octanoate adsorbed on pure γ -Al₂O₃. Figure 4.12 shows the TGA curves of pure γ -Al₂O₃ as well as adsorbed acetate and octanoate on γ -Al₂O₃. The weight loss measured from the TGA curve of pure γ -Al₂O₃ can be attributed to the loss of water only as this sample does not contain adsorbed acid. In the case of adsorbed acids on γ -Al₂O₃, the weight loss measured is due to the loss of both water and acid. TP-MS of both acetate and octanoate adsorbed on γ -Al₂O₃ (Figure 4.8 & Figure 4.9) indicated that acid decomposition occurs above 300°C. Therefore, the weight loss measured above 300°C in the TGA curves (Figure 4.12) can be taken as a measure of loss of acetate or octanoate, while the weight loss below 300°C can be attributed to the loss of water.

The TGA curve of pure γ -Al₂O₃ shows that significant loss of water occurs below 300°C (Figure 4.12). This weight loss is relatively larger than that observed for acetate or octanoate on γ -Al₂O₃, which instead show significant weight losses above 300°C. This implies that relatively more (weakly bound) water is adsorbed on pure γ -Al₂O₃, but in the case of the acids on γ -Al₂O₃, some acid molecules are adsorbed instead of water molecules.

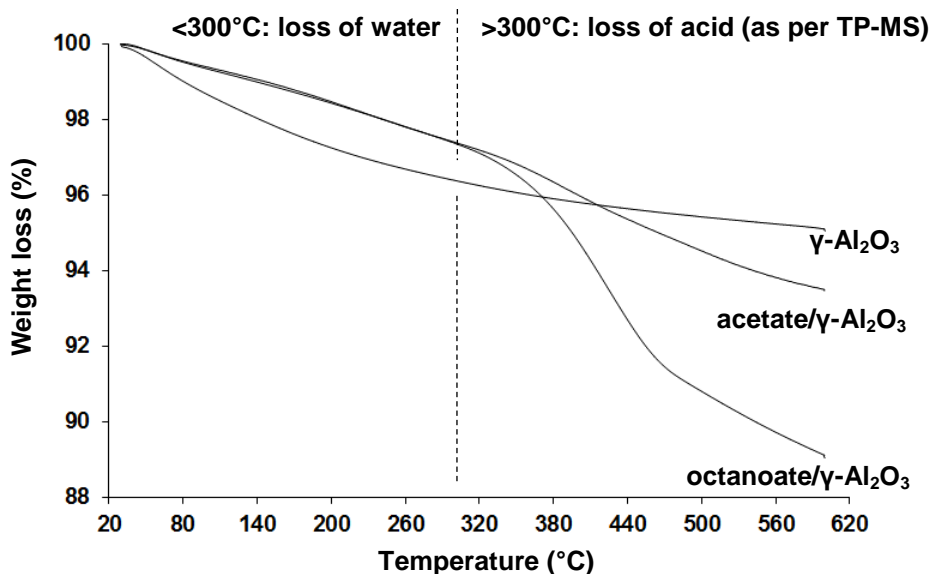


Figure 4.12: TGA curves of pure $\gamma\text{-Al}_2\text{O}_3$, acetate & octanoate adsorbed on $\gamma\text{-Al}_2\text{O}_3$. Dotted line indicates the temperature (300°C) above which the weight loss is attributed to acid decomposition (as determined using TPD-MS, Figure 4.8 & Figure 4.9).

Table 4.2 indicates the calculated saturation coverage of the acids on $\gamma\text{-Al}_2\text{O}_3$. These coverages refer to the freshly prepared acetate and octanoate adsorbed on $\gamma\text{-Al}_2\text{O}_3$, which was previously found to be comparable to the coverage after exposure to model FTS conditions (1 bar H_2/CO , 230°C, 10h) as determined by thermal stability studies using XPS (Figure 4.7). Both acetate and octanoate is adsorbed at a coverage of ~ 3 molecules per nm^2 of $\gamma\text{-Al}_2\text{O}_3$.

The difference between an acetate (C2) and octanoate (C8) molecule is the length of the carbon chain, but they are similar in the fact that they both

contain a carboxyl group. Therefore, the saturation coverage must be determined by the carboxyl groups of the acid and not by the length of the carbon chain.

Table 4.2: TGA results and calculated coverages of acetate & octanoate adsorbed on γ -Al₂O₃.

Sample	Total weight loss		Acid weight loss ^a		Acid Coverage ^b (molecules/nm ²)
	(%)	(mg)	(%)	(mg)	
acetate/ γ -Al ₂ O ₃	(6.6)	(0.2)	(4)	(0.1)	~3
octanoate/ γ -Al ₂ O ₃	(11.1)	(1.1)	(8.5)	(0.8)	~3

^a weight loss above 300°C in TGA curves (Figure 4.12)

^bcalculated using γ -Al₂O₃ surface area (BET) of 142 m²/g (Appendix Table 4.6)

Carbon is deposited on a sample of thermally treated adsorbed acetate on γ -Al₂O₃ (Figure 4.10). This quantity of carbon contributes to the initial quantity of acetate adsorbed on γ -Al₂O₃. In order to quantify the amount of deposited carbon, TPO-MS calibration experiments were carried out (Appendix Table 4.7). These experiments showed that the amount of carbon deposited was ~0.1wt% (mCarbon/mSample). This translates to ~0.1 molecules of acetic acid per nm² of γ -Al₂O₃. Therefore, the carbon deposited (0.1 wt%) is very small compared to the quantity of acetate desorbed from γ -Al₂O₃ after a thermal treatment (i.e. 4wt% acid loss measured by TGA).

Table 4.3 indicates the calculated water coverages on pure γ -Al₂O₃ as well as samples of acetate and octanoate adsorbed on γ -Al₂O₃. Interestingly, the acetate and octanoate-impregnated samples have comparable water

Chapter 4

coverages of ~ 7 molecules per nm^2 of $\gamma\text{-Al}_2\text{O}_3$. Furthermore, these samples have a lower water coverage than that of pure $\gamma\text{-Al}_2\text{O}_3$ (7 vs 13 molecules per nm^2 of $\gamma\text{-Al}_2\text{O}_3$, Table 4.3). Thus, 3 acid molecules (Table 4.2) replaces 6 water molecules on $\gamma\text{-Al}_2\text{O}_3$. For the case of acetate adsorbed on $\gamma\text{-Al}_2\text{O}_3$, the sample is prepared by impregnating an aqueous solution of acetic acid on pure $\gamma\text{-Al}_2\text{O}_3$, which means that water and acid are simultaneously added to $\gamma\text{-Al}_2\text{O}_3$. The result (after a drying step) is strongly adsorbed acetate on $\gamma\text{-Al}_2\text{O}_3$, which is evidence that the acid competes with water for adsorption on $\gamma\text{-Al}_2\text{O}_3$. This would explain the lower calculated water coverage on the samples of acids adsorbed on $\gamma\text{-Al}_2\text{O}_3$ compared to pure $\gamma\text{-Al}_2\text{O}_3$ (Table 4.3). For the case of octanoate adsorbed on $\gamma\text{-Al}_2\text{O}_3$, a methanol/octanoic acid impregnating solution is used, with the result being strongly adsorbed octanoate on $\gamma\text{-Al}_2\text{O}_3$. This further emphasizes the adsorption strength of the carboxylate, as this proves it to be stronger than that of an alcohol as well.

Table 4.3: TGA results and calculated water coverages on samples of pure $\gamma\text{-Al}_2\text{O}_3$ as well as acetate & octanoate adsorbed on $\gamma\text{-Al}_2\text{O}_3$.

Sample	Total weight loss		Water weight loss ^a		Water Coverage ^b (molecules/ nm^2)
	(%)	(mg)	(%)	(mg)	
pure $\gamma\text{-Al}_2\text{O}_3$	(5.0)	(0.3)	(5.0)	(0.3)	~ 13
acetate/ $\gamma\text{-Al}_2\text{O}_3$	(6.6)	(0.2)	(2.6)	(0.1)	~ 7
octanoate/ $\gamma\text{-Al}_2\text{O}_3$	(11.1)	(1.1)	(2.6)	(0.3)	~ 7

^aweight loss below 300°C in TGA curves (Figure 4.12)

^bcalculated using $\gamma\text{-Al}_2\text{O}_3$ surface area (BET) $142 \text{ m}^2/\text{g}$

4.3.9. IR of Co/ γ -Al₂O₃ catalyst treated with acetic acid at model FTS conditions

The previous sections (4.3.2 to 4.3.6) dealt with the adsorption and thermal stability of carboxylic acid on either the pure γ -Al₂O₃ support or cobalt metal surface in isolation. The present section investigates the stability and decomposition pathways of acetate on a commercially relevant Co/Pt/Al₂O₃ FTS catalyst. Reduced Co/Pt/Al₂O₃ catalyst was exposed to acetic acid saturated H₂/CO gas (1 bar_(a)) at 230°C to obtain conditions to model that of FTS. The resulting sample was characterized *ex situ* in the passivated state using IR (described in the present section) and characterized *in situ* using TPH-MS (described in the next section 4.3.9).

The IR absorption spectra of the acid-treated Co/Pt/Al₂O₃ FTS catalyst is shown in Figure 4.13. For comparison, spent Co FTS catalyst as well as acid-treated γ -Al₂O₃ is also plotted (Figure 4.13). A cobalt acetate reference compound is used to identify if either the fresh or spent catalyst could contain this metal-carboxylate compound.

The IR absorption spectrum of acetic acid-treated γ -Al₂O₃ exhibits peaks at ~1574, 1469 and 1424 cm⁻¹ (Figure 4.13). This is in agreement with IR absorption peaks obtained when acetate is adsorbed on γ -Al₂O₃ using an aqueous solution (Figure 4.3). Therefore, two different methods of acid impregnation have resulted in acetate formation on γ -Al₂O₃. In one method, acetate formed on γ -Al₂O₃ in the presence of water (Figure 4.3), while in the current method acetate formed on γ -Al₂O₃ at 230°C under H₂/CO gas (Figure 4.13). This emphasizes the adsorption strength of acetic acid to

Chapter 4

compete with water adsorption and the thermal stability of adsorbed acetate.

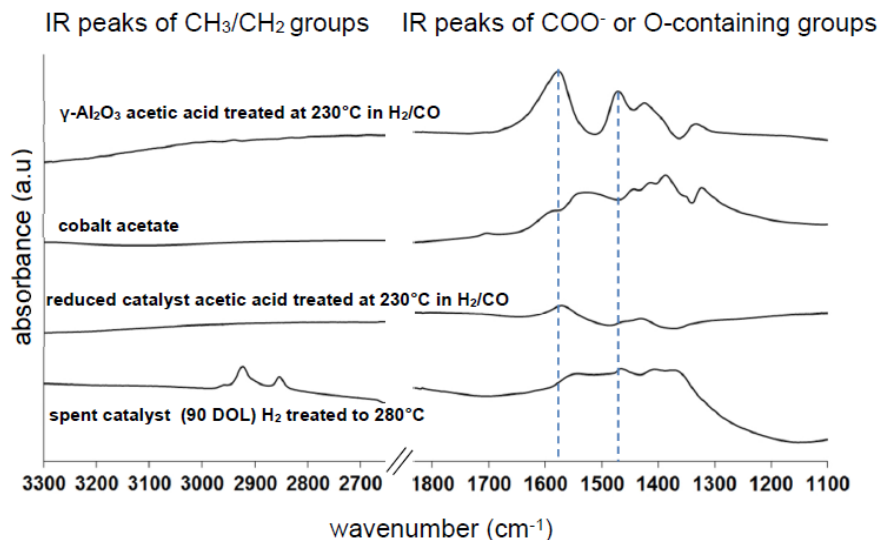


Figure 4.13: ATR-IR of spent Co/Pt/Al₂O₃ FTS catalyst (90 DOL) (wax extracted and hydrogen treated (to 280°C) and reference compounds (i) fresh catalyst acetic acid treated at 230°C in 1 bar H₂/CO (2/1), (ii) cobalt acetate and (iii) γ -Al₂O₃ acetic acid treated at 230°C in 1 bar H₂/CO (2/1).

The IR absorption spectrum of acetic acid-treated Co/Pt/Al₂O₃ catalyst exhibits peaks at ~1572, 1463 and 1429, cm⁻¹ (Figure 4.13). Therefore, the IR absorption peaks of acid-treated catalyst is comparable to that of acid-treated γ -Al₂O₃. Furthermore, the IR frequencies of cobalt acetate do not match those of acid-treated catalyst, implying that cobalt acetate compound formation is not significant. These findings suggest that intact acetate, observed after the treatment in acid-saturated synthesis gas, is adsorbed on the γ -Al₂O₃ support of the catalyst.

Similarly, the IR absorption peaks of spent catalyst also exhibit frequencies comparable to that of acid-treated $\gamma\text{-Al}_2\text{O}_3$ (Figure 4.13). This then implies that the origin of oxygenates on spent catalyst can be due to carboxylate adsorbed on the $\gamma\text{-Al}_2\text{O}_3$ support.

4.3.10. TPH-MS of Co/Pt/ $\gamma\text{-Al}_2\text{O}_3$ catalyst treated with acetic acid at model FTS conditions

TPH-MS experiments were carried out *in-situ* after reduced Co/Pt/ Al_2O_3 catalyst was exposed to acetic acid saturated H_2/CO gas (1 bar) at 230°C (i.e. conditions to model that of FTS). The TPH-MS profile was used to characterize the carbon deposited as a result of acid decomposition on Co/Pt/ $\gamma\text{-Al}_2\text{O}_3$ FTS catalyst (Figure 4.14). For comparison, TPH-MS profiles of spent catalyst as well as acid-treated $\gamma\text{-Al}_2\text{O}_3$ are also plotted (Figure 4.14).

The TPH-MS profile of wax extracted spent catalyst (90 DOL) shows three methane peaks at $\sim 290^\circ\text{C}$, 440 and 560°C (Figure 4.14). These temperatures are comparable to those found by Pinard *et al.*, where these peaks were assigned to atomic carbon, reduction of surface carboxylates and polymeric carbon respectively using TPH-IR [17]. The TPH-MS profile of acid-treated catalyst exhibits a broad methane peak at $\sim 295^\circ\text{C}$ (Figure 4.14), which is in the temperature range assigned to atomic carbon ($\sim 290^\circ\text{C}$) and lower than that assigned to polymeric carbon ($\sim 560^\circ\text{C}$) on spent catalyst [17]. This indicates that acetic acid decomposition over Co/Pt/ $\gamma\text{-Al}_2\text{O}_3$ FTS catalyst deposits predominantly atomic carbon on the catalyst.

Chapter 4

Carbon deposition could arise not only from acid decomposition on reduced catalyst, but also from CO dissociation on the metal surface (since acid saturated H_2/CO was used at $230^\circ C$). Therefore, a reference TPH-MS experiment was carried out on the reduced catalyst, where the synthesis gas used was acid-free (Figure 4.14). In this case, only a relatively small methane peak at $\sim 285^\circ C$ is observed, implying that carbon deposited specifically from CO dissociation contributes only a small quantity to the total carbon observed.

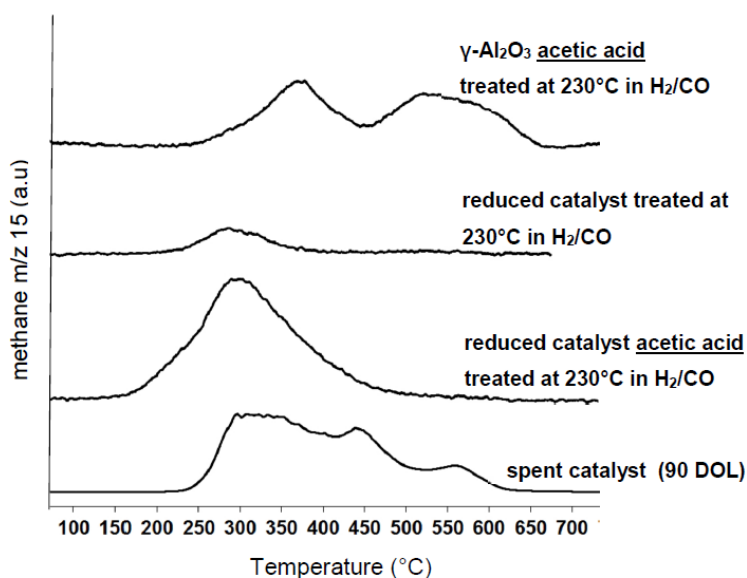


Figure 4.14: TPH-MS methane (m/z 15) profiles of wax-extracted spent Co FTS catalyst (90 DOL) and model compounds (i) reduced catalyst acetic acid treated at $230^\circ C$ in H_2/CO , (ii) reduced catalyst H_2/CO treated at $230^\circ C$ (iii) $\gamma-Al_2O_3$ acetic acid treated at $230^\circ C$ in H_2/CO .

Interestingly, the TPH-MS profile of acid-treated $\gamma-Al_2O_3$ showed two methane peaks at $290^\circ C$ and $550^\circ C$. Online GC-MS showed that these two

peaks can be assigned to acetone and methane respectively (Figure 4.8). Since these peaks are not observed at the same temperatures for that of acid-treated catalyst, this implies that the presence of cobalt on $\gamma\text{-Al}_2\text{O}_3$ changes the thermal stability and decomposition pathway of acetic acid. The major difference being that acetic acid decomposition forms polymeric carbon on pure $\gamma\text{-Al}_2\text{O}_3$ (peak at $\sim 550^\circ\text{C}$) but predominantly atomic carbon when Co metal is present (peak at $\sim 295^\circ\text{C}$).

4.3.11. Acetic acid co-feeding during Co-catalyzed FTS

In order to directly measure the effect of carboxylic acid on catalyst deactivation, a Co/Pt/ Al_2O_3 catalyst was tested in a CSTR operated at commercially relevant FTS conditions, while acetic acid was co-fed into the reactor with time-on-line (Figure 4.15).

The initial deactivation of a Co FTS catalyst can be attributed to a number of deactivation mechanisms including sintering, carbon deposition and metal surface reconstruction [35]. Sintering of the active metal phase is particularly severe in the first few days of FTS [35]. Therefore, to limit the contribution of sintering in the current deactivation study, the catalyst used had already been utilised in FTS for an extended period. The spent catalyst was initially removed from a FTS reactor after 30 days-on-line and recovered by unloading into wax. Then, for the purpose of this acid co-feeding experiment, the sample was loaded into the reactor again and reduced (at 425°C in H_2) before FTS testing. The fact that this catalyst was previously run for 30 days in a FTS reactor is the reason that the activity profiles plotted in Figure 4.15 begin after 30 DOL.

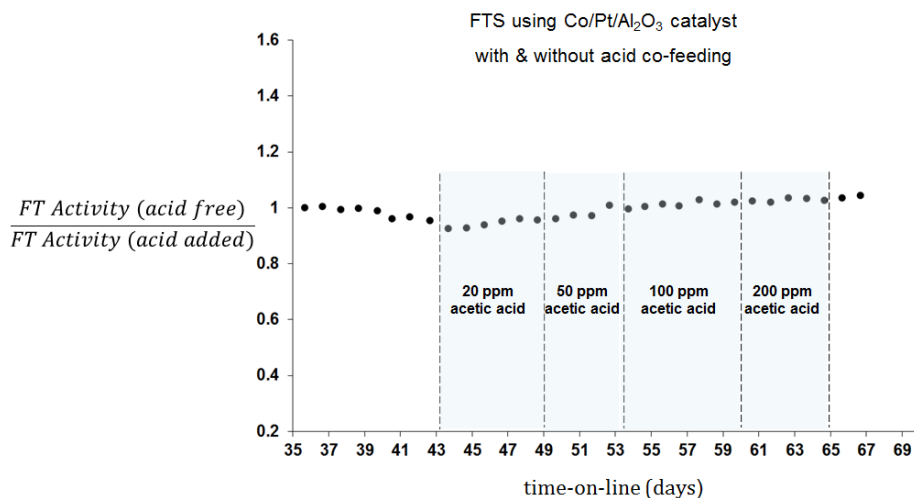


Figure 4.15: FTS testing of a Co/Pt/Al₂O₃ catalyst in continuous stirred-tank reactor (volume 1L) operated at 230°C, ~20 bar, (H₂+CO) conversion between 50-70% (constant conversion was targeted), feed gas composition of ~50 vol% H₂, 30 vol% CO and 20% inert gas (Ar), reactor water partial pressure of ~4-6 bar. An HPLC pump was used to flow (~0.1 mol/h) an acetic acid in ethanol (20-200 ppm) mixture directly into the reactor using a separate inlet feed line. Activity was first calculated as mol(CO converted)/g(catalyst)/h and then the ratio “FT Activity (acid-free) / FT Activity (acid added)” was determined.

Figure 4.15 shows the profile obtained when the FT activity of a typical Co catalyst is compared to that of a run when the concentration of acetic acid is gradually increased from 20ppm (at ~43 days) to 200 ppm (at ~60 days). The activity ratio (FT Activity (acid-free) / FT Activity (acid added)) is approximately 1 throughout the 24 days of FTS (Figure 4.15). This indicates that there is no enhancement of deactivation due to the addition of ~20-200 ppm acetic acid over 24 days. In fact, treating the catalyst with a range of acids of various chain length, such as formic, acetic, isobutyric and

hexanoic acid, during FTS still does not cause a significant enhancement of catalyst deactivation (Appendix, Figure 4.20)

4.4. Discussion

The primary objective of this study is to determine whether carboxylic acids contribute to Co FTS catalyst deactivation. Oxygenates have previously been detected on spent Co/Al₂O₃ FTS catalyst [16,17] and have also been identified as precursors for carbon formation [23,26]. These findings prompted an investigation into:

- (i) The location of adsorbed oxygenates on Co/Al₂O₃ FTS catalyst
- (ii) The stability and quantity of adsorbed carboxylate on γ -Al₂O₃ support
- (iii) Carbon formation due to thermal treatment of carboxylate adsorbed on γ -Al₂O₃
- (iv) Carbon formation due to acid decomposition over Co/Pt/Al₂O₃ catalyst
- (v) The current understanding of carbon formation as a Co FTS catalyst deactivation mechanism
- (vi) The effect of acid co-feeding on FTS catalyst deactivation

The location of adsorbed oxygenates on Co/Al₂O₃ FTS catalyst

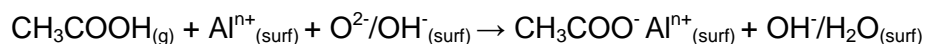
ATR-IR measurements show that oxygenated compounds are adsorbed on spent Co/Pt/Al₂O₃ FTS catalyst and remain adsorbed above FTS temperatures (i.e. they are stable up to 280°C in H₂).

Chapter 4

To investigate the adsorption of an oxygenated compound on Co/Pt/ γ -Al₂O₃ FTS catalyst, three separate approaches using model systems were taken. The interaction of carboxylic acid and pure γ -Al₂O₃ or a Co metal surface was studied in isolation. Also, Co/Pt/Al₂O₃ catalyst was exposed to acetic acid under model FTS conditions.

IR absorption spectra show that acetic acid is chemisorbed on pure γ -Al₂O₃ at room temperature. This adsorption results in the formation of stable acetate species *via* dissociative adsorption on γ -Al₂O₃ (Equation 4.1) [18].

(Equation 4.1)



Acetic acid competes with water for adsorption on γ -Al₂O₃ (since samples were prepared in an aqueous impregnating solution yet adsorbed acetate is still observed using IR). Furthermore, IR showed that a carboxylate with a relatively longer carbon chain (octanoic acid) is also chemisorbed on pure γ -Al₂O₃.

Co single crystal (0001) experiments indicate that acetic acid is thermally unstable on a Co metal surface at Co FTS temperature (200-230°C). This indicates that adsorbed oxygenates on spent catalyst are unlikely to be located on the metal phase.

Reduced Co/Pt/Al₂O₃ catalyst was exposed to acetic acid at model FTS conditions (i.e. acetic acid saturated H₂/CO (2/1) gas (1 bar) at 230°C). IR absorption peaks of acetic acid-treated Co/Pt/Al₂O₃ catalyst is comparable to those of γ -Al₂O₃ containing adsorbed acetate. In addition, IR absorption

peaks of a cobalt-acetate reference compound was not comparable to those of acid-treated catalyst or spent catalyst. This implies that the formation of a metal-carboxylate complex is not significant, supported by the findings from Co single crystal experiments.

Findings from these model studies provide evidence that adsorbed oxygenates detected on spent Co/Pt/ γ -Al₂O₃ FTS catalyst are located on the γ -Al₂O₃ support. These findings confirm the conclusions of Pinard *et al.* where acids adsorbed on γ -Al₂O₃ were reported to exhibit IR absorption peaks which were comparable to those of oxygenates identified on spent Co/Ru/Al₂O₃ FTS catalyst.

The thermal stability and quantity of adsorbed carboxylate on catalyst support

The thermal stability of acids adsorbed on pure γ -Al₂O₃ (acetate and octanoate) was investigated using XPS, TGA and TP-MS. XPS analyses show that the quantity of acid adsorbed is comparable before and after exposure to model FTS conditions. This implies that carboxylates adsorbed on γ -Al₂O₃ are thermally stable under synthesis gas at FTS temperature. TGA data enabled a calculation of the saturation coverages of acids on γ -Al₂O₃. Both acetate and octanoate are found to contain a coverage of ~3 molecules of acid and 7 molecules of water per nm² of γ -Al₂O₃, while pure γ -Al₂O₃ contains a water coverage of ~13 molecules per nm². These comparable saturation coverages are explained by similar modes of carboxylate and water coordination on the γ -Al₂O₃ surface. For instance, the 3 carboxylate functionalities (for acetate & octanoate) have a large

enough adsorption strength to displace the 6 water molecules from the Al^{3+} sites in a unit area of pure $\gamma\text{-Al}_2\text{O}_3$.

Carbon formation due to thermal treatment of carboxylate adsorbed on $\gamma\text{-Al}_2\text{O}_3$

Products formed due to thermal treatment of acetate and octanoate adsorbed on pure $\gamma\text{-Al}_2\text{O}_3$ requires temperature above 300°C . For the case of acetate, GC-MS analyses indicate that major gaseous products include acetone (375°C) and carbon dioxide (400°C) which can originate from a ketonization reaction over $\gamma\text{-Al}_2\text{O}_3$ [18,36,37].



Specific carbonaceous desorption products include methane (TPH peak at 600°C), propene (490°C) and isobutylene (420°C). These carbon species can arise from condensation reactions over the $\gamma\text{-Al}_2\text{O}_3$ surface as was previously proposed for the formation of isobutylene [18,19].



Products at temperatures significantly higher than that of Co FTS (i.e. $>300^\circ\text{C}$) imply that carboxylate decomposition on $\gamma\text{-Al}_2\text{O}_3$ is expected to be slow at Co FTS temperature ($200\text{-}230^\circ\text{C}$).

Thermal decomposition of acetate (to 700°C in He) deposits polymeric carbon on $\gamma\text{-Al}_2\text{O}_3$. This was found using TPO-MS which showed a high-

temperature CO₂ peak (~450°C), which is in a comparable temperature range assigned to polymeric carbon on spent Co/Pt/Al₂O₃ FTS catalyst (~400°C) [2]. The amount of carbon deposited (~0.1 wt%) is a small fraction of the quantity of acetate that is adsorbed at saturation coverage (i.e. 4wt% measured by TGA).

Carbon formation due to acid decomposition over Co/Pt/Al₂O₃ catalyst

Thermal stability of adsorbed acetic acid on γ -Al₂O₃ is significantly influenced by the presence of Co metal. The reaction of acetic acid with reduced Co/Pt/Al₂O₃ catalyst at model FTS conditions (H₂/CO, 1 bar_(a) at 230°C) not only results in adsorption of acid on the γ -Al₂O₃ support (IR), but also results in carbon formation on the catalyst (TPH-MS). The TPH-MS profile of acid-treated catalyst exhibits a methane peak (at ~295°C), which is in the temperature range assigned to surface carbidic species (atomic carbon) on spent catalyst by Pinard *et al.* [17] (Table 4.4). Therefore, acid decomposition over Co/Pt/ γ -Al₂O₃ catalyst, under synthesis gas at FTS temperature, deposits predominantly atomic carbon

Table 4.4: Carbon compounds on Co/Al₂O₃ catalyst from the present study compared to that in the literature.

T (hyd) (°C)	This study	T (hyd) (°C)	Carbon species Pinard et al. [17]
295	Atomic carbon: formed via acetic acid decomposition over Co/Pt/Al ₂ O ₃ FTS catalyst.	280	Atomic carbon on spent Co/Ru/Al ₂ O ₃ FTS catalyst
545	Polymeric carbon: formed by thermal decomposition of acetate over pure γ -Al ₂ O ₃ .	585	Polymeric carbon on spent catalyst

TPH-MS experiments reported were conducted using 10 vol% H₂.

Chapter 4

Polymeric carbon was not significant on the acetic acid-treated catalyst and was only observed in the thermal decomposition of acid-treated $\gamma\text{-Al}_2\text{O}_3$ (TPH-MS methane peak at $\sim 545^\circ\text{C}$, Table 4.4). This suggests that the Co metal changes the thermal stability and/or decomposition of carboxylate adsorbed on $\gamma\text{-Al}_2\text{O}_3$ support. A possible mechanism is the activation of hydrogen on the Co metal surface which migrates onto the $\gamma\text{-Al}_2\text{O}_3$ support (spill-over), enabling carboxylate decomposition at lower temperature. A similar mechanism was postulated by Pestman *et al.* where hydrogen is activated on platinum and migrates onto an oxidic support surface [37].

Previous studies have reported that atomic carbon on spent Co FTS catalyst, originates from surface carbidic species or hydrocarbons on Co [2,17]. The present study indicates that atomic carbon can also be deposited on Co/Pt/ Al_2O_3 FTS catalyst due to carboxylate decomposition.

The current understanding on carbon formation as a Co FTS catalyst deactivation mechanism

Moodley *et al.* previously found that the build-up of polymeric carbon on spent Co/Pt/ Al_2O_3 FTS catalyst is correlated with a loss of available metal surface area [2]. Therefore, polymeric carbon is expected to contribute to FTS catalyst deactivation by blocking active metal sites.

Ciobîcă *et al.* investigated using theoretical calculations if atomic carbon causes surface reconstruction on both the fcc-Co(100) and fcc-Co(111) phases [38]. However, the high carbon coverages (0.5 ML) required for the reconstruction to occur are not expected at typical FTS temperatures on a close-packed surface where hydrogen is available [8]. Therefore, carbon

formation is not envisaged to cause a surface reconstruction which might drive catalyst deactivation.

Furthermore, the impact of cobalt carbide formation on the deactivation of a Co/Pt/Al₂O₃ FTS catalyst was found to be negligible by Claeys *et al.*, in studies utilizing an *in-situ* magnetometer [39]. Only a small percentage (~5-10%) of the available metal was deduced to form carbide (Co₂C) at FTS conditions, and particularly at atypical or rather extreme conditions such as low syngas (H₂/CO) ratio.

In the current study, acetic acid decomposition over the metal surface is found to produce predominantly atomic carbon. Compared to polymeric carbon, atomic carbon can be more readily hydrogenated at FTS temperature. Therefore, the contribution of carboxylate decomposition to FTS catalyst deactivation is expected to be limited (dependent on operating conditions as high concentrations of acids could result in more severe carbon deposition).

On the basis of findings in the present study, carboxylic acid decomposition is excluded as a source of polymeric carbon during Co-catalyzed FTS. Therefore, the source of polymeric carbon is envisaged to be that proposed by Weststrate *et al.* whereby side reactions to FTS occur, resulting in acetylenic surface intermediates which either react with each other to form non-aromatic polymeric carbon species or undergo cyclo-polymerization to form aromatic polymeric carbon species [8].

The effect of acid co-feeding on FTS catalyst deactivation

The impact of carboxylic acid on Co/Pt/Al₂O₃ catalyst deactivation was directly measured by co-feeding acetic acid to a continuous stirred-tank reactor operated at commercially relevant FTS conditions. Co-feeding of acetic acid (~20-200 ppm) over 24 days did not result in enhanced catalyst deactivation.

The adsorption of carboxylate on γ -Al₂O₃ does not cause deterioration of the structural integrity of γ -Al₂O₃ (as determined by SEM and BET). However, strongly adsorbed carboxylates do imply that the support is essentially modified during FTS. This finding could be significant since, for example, the support could become more hydrophobic due to carboxylate adsorption or the support pores could become plugged by longer chain compounds. These hypotheses can be investigated using different supports e.g. SiO₂ and TiO₂, which not only have different hydrophobicity and acidity compared to Al₂O₃, but also different acid adsorption and decomposition sites.

4.5. Conclusions

Adsorbed oxygenates detected on spent Co/ γ -Al₂O₃ FTS catalyst are located on the γ -Al₂O₃ support. The formation of a metal-carboxylate compound is not detected and deduced to be unlikely since acetic acid decomposes at low temperature on a Co metal surface. Both short (acetate) and longer chain (octanoate) carboxylates are chemisorbed on

pure $\gamma\text{-Al}_2\text{O}_3$ and are thermally stable at Co FTS temperature under synthesis gas. Acetic acid competes with water for adsorption on $\gamma\text{-Al}_2\text{O}_3$. Thermal decomposition of adsorbed acetate on pure $\gamma\text{-Al}_2\text{O}_3$ produces polymeric carbon, however the thermal stability is significantly influenced by the presence of Co metal. This is demonstrated when acetic acid vapor is contacted with reduced Co/Pt/ Al_2O_3 catalyst, at model FTS conditions (i.e. 1 bar_(a) $\text{H}_2/\text{CO}:2/1$ at 230°C) and deposits predominantly atomic carbon on the catalyst. Co-feeding of excess acetic acid during FTS does not enhance Co/Pt/ Al_2O_3 catalyst deactivation. Carboxylic acids can cause atomic carbon formation on Co/ $\gamma\text{-Al}_2\text{O}_3$ catalyst during FTS and result in strongly adsorbed carboxylates on $\gamma\text{-Al}_2\text{O}_3$ support, but these factors do not significantly impact catalyst deactivation.

4.6. Appendix

4.6.1. IR background spectra

Table 4.5: List of background spectra used for the respective IR measurements

Figure	IR spectrum	IR background spectrum
2	spent catalyst (5 and 90 DOL)	reduced and wax encapsulated fresh catalyst
2	spent catalyst (5 and 90 DOL) H ₂ -treated to 280°C	reduced and wax encapsulated fresh catalyst H ₂ -treated to 280°C
2	reduced and wax encapsulated fresh catalyst H ₂ -treated to 280°C	reduced catalyst that is passivated by controlled exposure to air in the reactor
3	Acetic acid adsorbed on γ -Al ₂ O ₃	γ -Al ₂ O ₃
3	Octanoic acid adsorbed on γ -Al ₂ O ₃	γ -Al ₂ O ₃
9	γ -Al ₂ O ₃ acetic acid treated at 230°C in H ₂ /CO	γ -Al ₂ O ₃
9	reduced catalyst acetic acid treated at 230°C in H ₂ /CO	reduced catalyst passivated by controlled exposure to air in the reactor

4.6.2. BET surface area measurements

Table 4.6: BET surface area measurements of γ -Al₂O₃ and acetate/ γ -Al₂O₃.

Sample	BET surface area (m ² /g)	Pore volume (cm ³ /g)
γ -Al ₂ O ₃	142 ± 0.15	0.45
acetate/ γ -Al ₂ O ₃	148 ± 2.3	0.47

4.6.3. XPS survey spectra

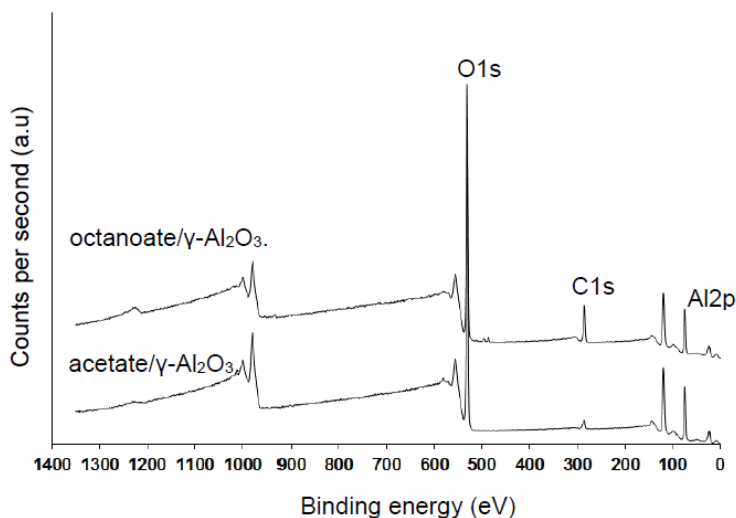


Figure 4.16: XPS survey spectra of acetate and octanoate adsorbed on γ - Al_2O_3 , showing only the expected signals of $\text{Al}2\text{p}$, $\text{C}1\text{s}$, $\text{O}1\text{s}$ and the corresponding Auger peaks.

4.6.4. TP-MS spectra

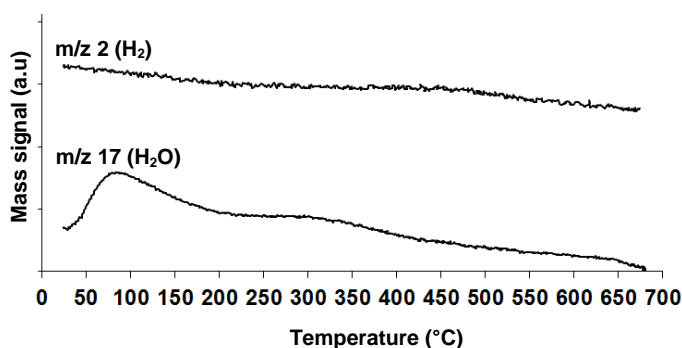


Figure 4.17: TPD-MS spectra of pure γ - Al_2O_3 , showing the expected peak for H_2O desorption and no significant increase in the H_2 signal with increasing temperature.

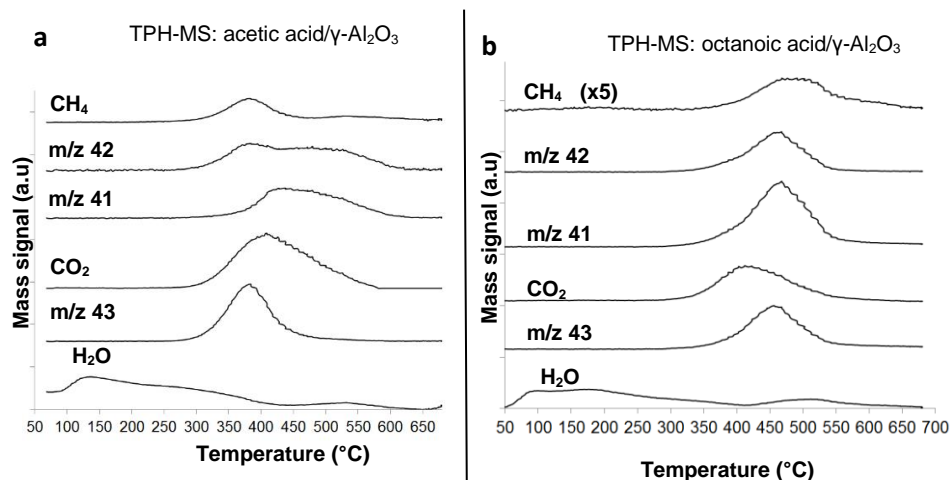


Figure 4.18: TPH-MS spectra of (a) acetic acid and (b) octanoic acid adsorbed on γ -Al₂O₃, showing that the temperature of the spectral peaks are unchanged under a hydrogen atmosphere.

4.6.5. Determination of the quantity of carbon deposited using TPO-MS calibration

Various masses of NaHCO₃ were used in TPO-MS experiments to produce CO₂ *via* Equation 4.4 [40]. This thermal decomposition reaction takes place between 70-200°C while the subsequent decomposition (Equation 4.5) takes place at 1000°C. Thus, the calibration experiments were carried out at 250°C to fully complete the initial decomposition reaction but avoid the latter.



From the initial NaHCO_3 masses used in TPO-MS measurements, the theoretical quantity of CO_2 produced can be calculated and correlated with CO_2 (m/z 44) peak areas in a TPO calibration plot (Figure 4.19). TPO-MS is carried out directly after a TPD-MS experiment using acetate/ $\gamma\text{-Al}_2\text{O}_3$ (Figure 4.11). The resulting CO_2 (m/z 44) peak area from this experiment can then be used to obtain the quantity of CO_2 (derived from the TPO calibration plot) which provides the quantity of carbon deposited (Table 4.7).

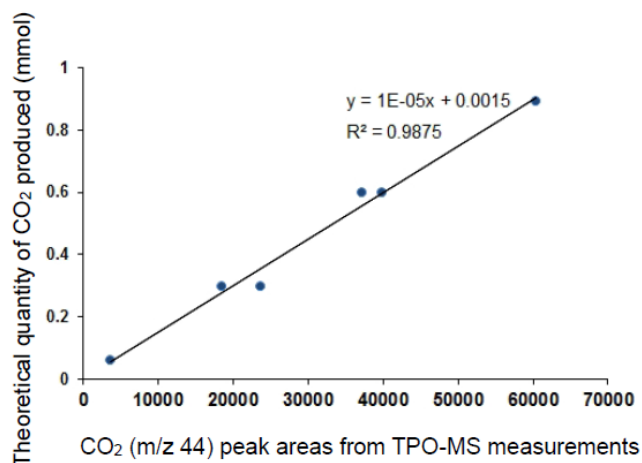


Figure 4.19: Calibration curve of CO_2 peak area vs theoretical quantity of CO_2 produced with increasing masses of NaHCO_3 used in TPO-MS experiments.

Table 4.7: Determination of quantity of carbon deposited on $\gamma\text{-Al}_2\text{O}_3$ after TPD-TPO treatment.

sample	Peak area ^a	$n\text{CO}_2$ (mmol) ^b	$m\text{C}$ (mg)	$m\text{C}/m\text{Sample}$ wt(%)
acetate/ $\gamma\text{-Al}_2\text{O}_3$ after TPD-TPO	725	0.0087	0.1	0.1

^a from TPO-MS experiments (Figure 4.11)

^b from the TPO-MS calibration plot (Figure 4.19)

4.6.6. The effect of acid co-feeding on FTS catalyst deactivation

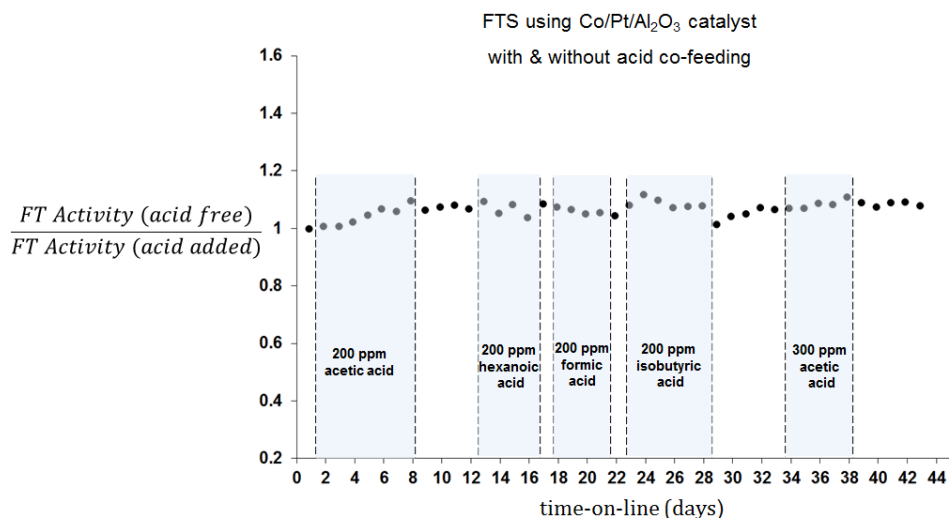


Figure 4.20: FTS testing of a Co/Pt/Al₂O₃ catalyst in a continuous stirred-tank reactor (volume 1L) operated at 230°C, ~20 bar, (H₂+CO) conversion between 50-70% (constant conversion was targeted), feed gas composition of ~50 vol% H₂, 30 vol% CO and 20% inert gas (Ar), reactor water partial pressure of ~4-6 bar. An HPLC pump was used to flow (~0.1 mol/h) acids in ethanol mixtures directly into the reactor using a separate inlet feed line. Activity was first calculated as mol(CO converted)/g(catalyst)/h and then the ratio “FT Activity (acid-free) / FT Activity (acid added)” was determined.

4.7. References

- [1] D. J. Moodley, J. van de Loosdrecht, A. M. Saib, J. W. Niemantsverdriet, *Prepr. Pap.-Am. Chem. Soc., Div. Petr. Chem.* 53 (2008) 122-125.
- [2] D. J. Moodley, J. van de Loosdrecht, A. M. Saib, M. J. Overett, A. K. Datye, J. W. Niemantsverdriet, *Appl. Catal. A* 354 (2009) 102-110.
- [3] D. -K. Lee, J. -H. Lee, S. -K. Ihm, *Appl. Catal.* 36 (1988) 199-207.
- [4] V. Gruver, R. Young, J. Engman, H. J. Robota, *Prepr. Pap.-Am. Chem. Soc., Div. Pet. Chem.* 50 (2005) 164-166.
- [5] M. K. Niemela, A. O. I. Krause, *Catal. Lett.* 42 (1996) 161-166.
- [6] G. Boskovic, K. J. Smith, *Catal. Today* 37 (1997) 25.
- [7] D. Pena, A. Griboval-Constant, V. Lecocq, F. Diehl, A. Y. Khodakov, *Catal. Today* 215 (2013) 43-51.
- [8] C. J. Weststrate, I. M. Ciobica, A. M. Saib, D. J. Moodley, J. W. Niemantsverdriet, *Catal. Today* 228 (2014) 106–112.
- [9] C. J. Weststrate, A. C. Kizilkaya, E. T. R. Rossen, M. W. G. M. Verhoeven, I.M. Ciobica, A. M. Saib, J. W. Niemantsverdriet, *J. Phys. Chem. C* 116 (2012) 11575–11583.
- [10] A. P. Steynberg, M. E. Dry (Eds), *Fischer-Tropsch technology*, Elsevier, Amsterdam, 152, 2004.
- [11] F. P. Di Sanzo, *Anal. Chem.* 53 (1981) 1911-1914.
- [12] J. van de Loosdrecht, F. G. Botes, I. M. Ciobica, A. Ferreira, P. Gibson, D. J. Moodley, A. M. Saib, J. L. Visagie, C. J. Weststrate, J. W. Niemantsverdriet, *Fischer-Tropsch synthesis: catalysts and chemistry*, In J. Reedijk & K. Poepelmeier (Eds.), *Comprehensive Inorganic Chemistry II (Second Edition): from elements to applications*, Elsevier, Amsterdam, 2013, 525-557.
- [13] P. Di Sanzo, J. L. Lane, P. M. Bergquist, S. A. Mooney, B. G. Wu, *J. of Chrom. A*, 281 (1983) 101-108.
- [14] R. R. Anderson, C. M. White, *J. High Resol. Chromatogr.* 17 (1994) 245–250.
- [15] R. J. J. Nel A. de Klerk, *Ind. Eng. Chem. Res.* 46 (2007) 3558–3565.

Chapter 4

- [16] D. Pena, A. Griboval-Constant, C. Lancelot, M. Quijada, N. Visez, O. Stephan, V. Lecocq, F. Diehl, A. Y. Khodakov, *Catal. Today* 228 (2014) 65-76.
- [17] L. Pinard, P. Bichon, A. Popov, J. L. Lemberton, C. Canaff, F. Mauge, P. Bazin, E. Falabella S. -Aguiar, P. Magnoux, *Appl. Catal. A: Gen.* 406 (2011) 73.
- [18] M. A. Hasan, M. I. Zaki, L. Pasupulety, *Appl. Catal. A: Gen.* 243 (2003) 81–92
- [19] M. I. Zaki, M. A. Hasan, F. A. Al-Sagheer, L. Pasupulety, *Langmuir* 16 (2000) 430-436.
- [20] M. I. Zaki, N. Sheppard, *J. Catal.* 80 (1983) 114-122.
- [21] G. A. M. Hussein, N. Sheppard, M. I. Zaki, R. B. Fahim, *J. Chem. Soc., Faraday Trans. I* 57 (1990) 367.
- [22] D. Wang, D. Montane, E. Chornet, *Appl. Catal. A: Gen.* 143 (1996) 245-270.
- [23] X. Hu, G. Lu, *Appl. Catal. B* 99 (2010) 289–297.
- [24] B. Zhang, X. Tang, Y. Li, W. Cai, Y. Xu, W. Shen, *Catal. Commun.* 7 (2006) 367-372.
- [25] D.L. Trimm, *Catal. Today* 49 (1999) 3-10.
- [26] E. C. Vagia, A. A. Lemonidou, *Int. J. Hydrogen Energy* 32 (2007) 212-223.
- [27] P. J. van Berge, J. van de Loosdrecht, J. L. Visagie, United States Patent 6,806,226 (2004), to Sasol.
- [28] P. J. van Berge, J. van de Loosdrecht, E. Caricato, S. Barradas, B.H. Sigwebela, United States Patent 6,455,462 (2002), to Sasol.
- [29] P. J. van Berge, J. van de Loosdrecht, E. Caricato, S. Barradas, United States Patent 6,638,889 (2004), to Sasol.
- [30] R. L. Espinoza, J. L. Visagie, P. J. van Berge, F. H. Bolder, United States Patent 5,733,839 (1998), to Sasol.
- [31] A. Potter, J. L. Ritter, *J. Phys. Chem.* 58 (1954) 1040-1042.
- [32] J. F. Moulder, W.F. Stickle, P.E. Sobol, K. D. Bomben, *Handbook of X-ray Photoelectron Spectroscopy*, J. Chastain (Ed), Perkin-Elmer Corporation Physical Electronics Division, Minnesota, 1995.
- [33] K. Nakamoto, *Infrared Spectra of Inorganic and Coordination Compounds*, Wiley/Interscience, London, 1970, pp. 220–224.

- [34] I. R. Hill, I. W. Levin, *J. Chem. Phys.* 70 (1979) 2
- [35] A. M. Saib, D. J. Moodley, I. M. Ciobîcă, M. M. Hauman, B. H. Sigwebela, C. J. Weststrate, J. W. Niemantsverdriet, J. van de Loosdrecht, *Catal. Today* 154 (2010) 271–282.
- [36] S. Rajadurai, *Catal. Rev. -Sci. Eng.* 36 (1994) 385-403.
- [37] R. Pestman, R. M. Koster, J. A. Z. Pieterse, V. Ponc. *J. Catal.* 168 (1997) 255-264.
- [38] I. M. Ciobîcă, R.A. van Santen, P.J. van Berge, J. van de Loosdrecht, *Surf. Sci.* 602 (2008) 17–27.
- [39] M. Claeys, M. E. Dry, E. van Steen, E. du Plessis, P. J. van Berge, A. M. Saib, D. J. Moodley, *J. Catal.* 318 (2014) 193-202.
- [40] M. Maciejewski, A. Baiker, *Thermochimica Acta*, 295 (1997) 95-105.

5

Acetic acid adsorption on γ -Al₂O₃ (110) & (100) surfaces: A Density Functional Theory & Infrared Spectroscopy study

5.1. Introduction

The role of carboxylic acids in cobalt Fischer-Tropsch synthesis (FTS) catalyst deactivation has been investigated and the results discussed in Chapter 4 of this thesis. Adsorbed oxygenates were detected on spent Co/ γ -Al₂O₃ FTS catalyst using infrared (IR) spectroscopy and deduced to be located on the γ -Al₂O₃ support. Carboxylate compounds were found to be chemisorbed on pure γ -Al₂O₃ and thermally stable at Co FTS temperature under synthesis gas. In fact, carboxylates could only be removed above 300°C, which is significantly higher than that of Co FTS temperature (200-230°C). The reason for the strong adsorption of carboxylate molecules was envisaged to be due to strong interaction of the nucleophilic carboxylate (COO⁻) group with aluminum cations (Al³⁺) on the γ -Al₂O₃ surface.

Raybaud *et al.* showed from molecular dynamics studies that a crystallographic non-spinel monoclinic description for γ -Al₂O₃ is a viable model for theoretical studies [1]. This model provided good agreement with an experimentally determined non-cubic spinel γ -Al₂O₃ XRD structure and has been used extensively as a model for Density Functional Theory (DFT) studies [2-12]. Previous studies using neutron diffraction analysis have shown that the γ -Al₂O₃ surface termination consists of 83% of the (110) surface, while the (100) surface comprises the remaining 17% [13]. In addition, electron microscopy studies showed that the (110) surface is the predominantly observed surface, with significantly lower presence of the (100) and (111) surfaces [14]. Recently, the γ -Al₂O₃ model was used in an adsorption study of an oxygenate on the (100) and (110) surfaces [15]. Isopropanol was found to interact with the γ -Al₂O₃ surface *via* its hydroxyl

group. Dissociative and molecular adsorption of isopropanol was identified on the dehydrated (100) surface, while molecular adsorbed isopropanol was found to be thermodynamically most competitive on the (110) surface [15].

5.2. Research objective

The aim of the present study is to describe the strong interaction between a carboxylate compound, acetic acid, and two representative γ -Al₂O₃ surfaces. Vibrational frequencies were obtained by carrying out normal mode analyses on the most stable DFT optimized configurations. These frequencies were then compared to measured IR data. This enabled a determination of the precise adsorption structure of acetic acid adsorbed on γ -Al₂O₃. Determination of surface residence times of acetic acid on the γ -Al₂O₃ surfaces, and comparison to adsorption of water, is used to provide further insight into experimental findings.

The main objectives of the study include:

- (i) Identification of the most stable adsorption structure of acetic acid on the dehydrated γ -Al₂O₃ (110) & (100) surfaces.
- (ii) Comparison of IR measured and DFT calculated vibrational frequencies of acetic acid adsorbed on γ -Al₂O₃
- (iii) Determination of surface residence times of acetic acid adsorbed on the dehydrated γ -Al₂O₃ (100) & (110) surfaces.
- (iv) Determination of comparative adsorption between acetic acid & water on the dehydrated γ -Al₂O₃ (100) & (110) surfaces.

5.3. Calculation Methodology

5.3.1. Preparation and IR measurement of acetic acid adsorbed on γ -Al₂O₃

Acetic acid was adsorbed on γ -Al₂O₃ by adding (10 ml) of an aqueous acetic acid solution (5 vol%, room temperature) to γ -Al₂O₃ (2g) which was pre-dried at 120°C for 10 mins. The resulting suspension was stirred (1 min) before the excess solution was filtered off and the sample dried (for 10 min) at 120 °C in air. The sample of acetic acid adsorbed on γ -Al₂O₃ was measured using attenuated total reflectance infrared spectroscopy (ATR-IR) recorded using a Nicolet Smart Golden gate instrument equipped with a diamond crystal (cutoff at 800 cm⁻¹). Measurements were carried out in transmission mode using the appropriate background with a resolution of 2 cm⁻¹ over 128 scans.

5.3.2. Geometry optimization parameters

All density functional theory (DFT) calculations were performed using the Vienna ab initio simulation package (VASP 4.6). The exchange-correlation energy was calculated using the Perdew-Wang (PW91) generalized gradient approximation (GGA) functional, together with projector augmented wave (PAW) method. The VASP plane wave basis set cut-off energy of 425 eV was used. Brillouin zone integration was achieved by summation over a Monkhorst-Pack mesh of k-points using a k-point grid of 3x3x1 for the respective a, b and c unit cell parameters for both the (100) and (110) γ -Al₂O₃ unit cell slabs. For all calculations, Gaussian smearing was employed with $\sigma = 0.05$ eV. A vacuum spacing of 12 Å was set

between two periodically repeating slabs. The energy convergence criteria for self-consistent field (SCF) optimization was set to 1×10^{-4} eV, while ionic relaxation was performed according to a conjugate gradient optimization algorithm. Structural optimization continued until the forces on unconstrained atoms fell below 0.02 eV/\AA .

Calculations were carried out using four layer periodic slab models for the p(2x1) and p(1x1) slabs, containing 16 Al₂O₃ units, for the (100) and (110) surfaces respectively.⁶ The surface layer of the slab and adsorbed molecules were fully relaxed for the calculations.

The γ -Al₂O₃ (100) surface unit cell ($a = 1.12 \text{ nm}$, $b = 0.84 \text{ nm}$, surface area = 0.94 nm^2) contained a slab thickness of 0.67 nm . For optimization, atoms in the bottom 0.23 nm of the slab were constrained to their bulk optimized positions, while all remaining atoms and adsorbates were allowed to fully relax during optimizations. The γ -Al₂O₃ (110) surface unit cell ($a = 0.81 \text{ nm}$, $b = 0.84 \text{ nm}$, surface area = 0.68 nm^2) contained a slab thickness of 1.0 nm . The atoms situated in the bottom 0.44 nm of the slab were constrained to their bulk optimized positions, while all remaining atoms including adsorbates were allowed to fully relax during optimization.

5.3.3. Vibration analysis

The most stable optimized geometries were subjected to a normal mode analysis within the frozen phonon approximation. The Hessian matrix for each structure was constructed using finite differences by perturbing all

⁶ Dehydrated alumina slab models were developed by Werner Janse van Rensburg at Sasol Technology, South Africa.

surface and adsorbate atoms, in the top 0.25 nm of the slab, by 0.02 Å in the direction of each Cartesian coordinate. All atoms situated in the bottom 0.42 nm of the (100) surface slab and 0.77 nm of the (110) slab were kept fixed to their optimized positions for normal mode analysis. Diagonalization of the mass-weighted Hessian matrix for each geometry yielded the associated vibrational stretches within the harmonic approximation, from which zero-point energy corrections to calculated total electronic energies have been determined. Accelrys Materials Studio 6.1 software was used for visualization purposes.

5.3.4. Adsorption energy calculations

Acetic acid adsorption energies were calculated according to Equation 5.1.

$$E_{\text{ads}} = [E_{\text{acid/alumina}} - E_{\text{alumina}} - \eta E_{\text{acid}}] / \eta \quad (\text{Equation 5.1})$$

- E_{ads} refers to the average adsorption energy (i.e. enthalpy at 0K) for an acetic acid molecule adsorbed on the $\gamma\text{-Al}_2\text{O}_3$ surface, the more negative the value the more favorable the adsorption.
- $E_{\text{acid/alumina}}$ is the zero-point corrected energy for an adsorption structure of acetic acid adsorbed on $\gamma\text{-Al}_2\text{O}_3$
- E_{alumina} is the zero-point corrected energy of the $\gamma\text{-Al}_2\text{O}_3$ surface
- η denotes the number of acid molecules per surface unit cell in the adsorption structure of acetic acid adsorbed on $\gamma\text{-Al}_2\text{O}_3$

- E_{acid} is the zero-point corrected energy of a free acid molecule in the gas phase

5.3.5. Surface residence time calculations

Acetic acid surface residence times, (τ), were calculated according to Equation 5.2 [16].

$$\tau = \tau_o e^{\frac{-E(\text{ads})}{RT}} \quad (\text{Equation 5.2})$$

- τ_o is oscillation time in the adsorbed state ($\sim 10^{-13}$ s [17])
- E_{ads} refers to the average adsorption energy (i.e. enthalpy at 0K) for an acetic acid molecule adsorbed on the γ -Al₂O₃ surface (determined using Equation 1).
- R is the gas constant
- T is the absolute temperature (i.e. Co FTS temperature of 500K)

5.3.6. γ -Al₂O₃ surface models

5.3.6.1. γ -Al₂O₃ (110) surface model

The γ -Al₂O₃ model used in the present study is based on the orientation within the non-spinel monoclinic γ -Al₂O₃ structure developed by Raybaud *et al.* [1,18]. Figure 5.1 shows the top and side views of the dehydrated γ -Al₂O₃ (110) unit cell representation, which exposes a total surface area of 0.68 nm² (unit cell lengths of a=0.81 nm, b=0.84 nm). Four tri-coordinated O atoms, O(6), O(10), O(11), O(12) and two equivalent di-coordinated O atoms, O(4) and O(5), are exposed at the surface.

One tri-coordinated Al(III) atom, Al(1), and three tetra-coordinated Al(IV) atoms, Al(2) as well as equivalent Al(3) & Al(4) atoms, are exposed at the surface. Al(1) forms a planar AlO₃ surface with O(1), O(4) & O(5). Subsurface layers consist of Al atoms with two octahedral centres, one penta-coordinated Al(V) atom and one tetra-coordinated Al(IV) atom. Acetic acid adsorption was investigated on all Al and O atoms exposed at the surface.

Acetic acid adsorption on $\gamma\text{-Al}_2\text{O}_3$ (110) & (100) surfaces...

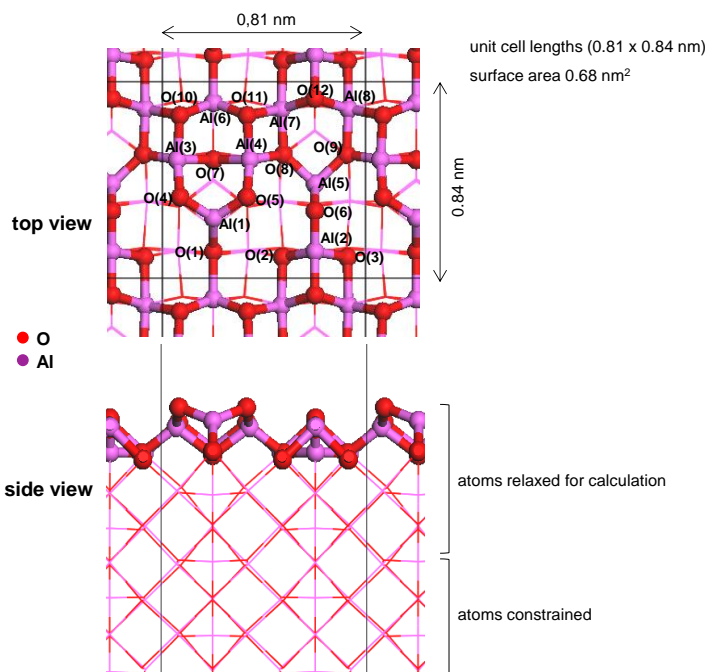


Figure 5.1: Top and side views of the optimized $\gamma\text{-Al}_2\text{O}_3$ (110) surface model.

5.3.6.2. $\gamma\text{-Al}_2\text{O}_3$ (100) surface model

Figure 5.2 shows the top and side views of the dehydrated $\gamma\text{-Al}_2\text{O}_3$ (100) unit cell representation which exposes a total surface area of 0.94 nm² (unit cell lengths of $a=1.12$ & $b=0.84$ nm).

Twelve tri-coordinated O atoms are exposed at the surface. Atoms O(1), O(2), O(5) and O(6) are equivalent, atoms O(3), O(4), O(7) and O(8) are equivalent and also atoms O(9), O(11), O(10) and O(12) are equivalent.

Four penta-coordinated aluminum Al(V) atoms Al(1), Al(2), Al(3) & Al(4) are exposed at the surface. Atoms Al(1) & Al(3) are equivalent and also atoms Al(2) & Al(4) are equivalent. Four equivalent tetra-coordinated Al(IV) atoms Al(5), Al(6), Al(8) & Al(9) are also exposed at the surface. Two equivalent tetra-coordinated Al(IV) atoms, Al(7) & Al(10), are positioned subsurface. The subsurface positioned aluminum atoms are not available for adsorption, therefore, all remaining Al sites and O sites exposed at the surface were investigated for acetic acid adsorption.

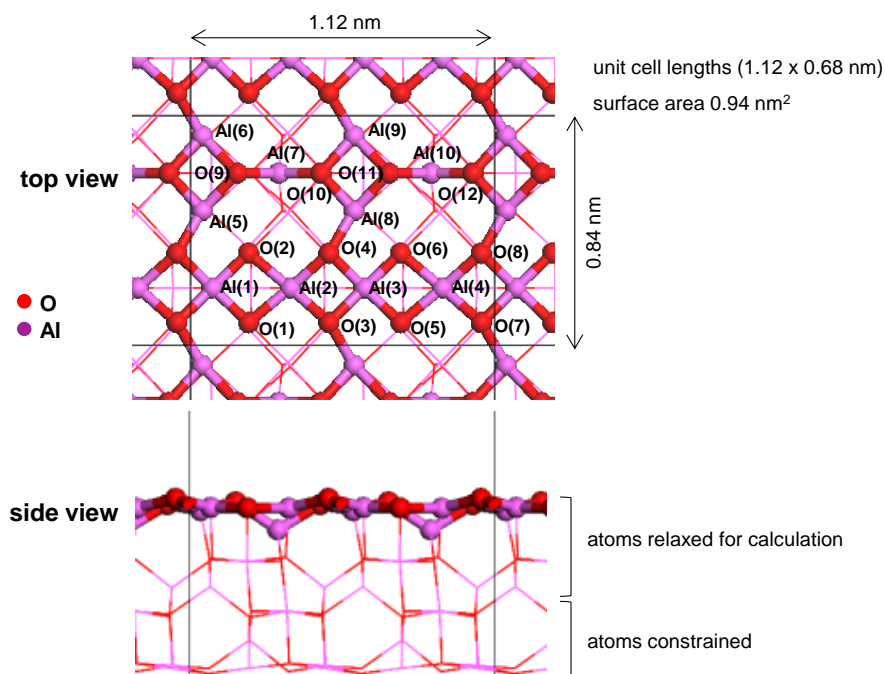


Figure 5.2: Top and side view of the optimized γ - Al_2O_3 (100) surface model.

5.4. Results

Acetic acid adsorption, on all Al and O atoms exposed, was investigated to identify the most stable adsorption structures of acetic acid on the γ -Al₂O₃ (100) and (110) surfaces. The following results section compares various modes of acetic acid adsorption on the different Al sites, including an investigation of adsorption at higher acid coverages.

5.4.1. Acetic acid adsorption on the γ -Al₂O₃ (110) surface

Figure 5.3 shows four optimized configurations on the γ -Al₂O₃ (110) surface when acetic acid undergoes both molecular and dissociative adsorption as well as adsorption at a higher coverage.

The largest acetic acid adsorption energy (-354 kJ/mol) is obtained when (i) two O atoms of the acid are coordinated to two Al atoms, Al(1) and Al(2) and (ii) the H atom of the acid has dissociated from the acid molecule to be coordinated to an O atom, O(12), on the γ -Al₂O₃ (110) surface. This is shown by the most stable adsorption structure, 110-Al(1,2)-O(12), in Figure 5.3. Coordination of only one O atom of the acid to an Al atom as shown by configuration 110-Al(1)-O(10), results in less favorable adsorption (by a difference of 130 kJ/mol). Furthermore, coordination of only one O atom and in the case that the H atom is not dissociated from the acid molecule, as shown by configuration 110-Al(2), results in the least favorable adsorption (by a difference of 208 kJ/mol). Therefore, dissociative adsorption of acetic acid, *via* coordination of two O atoms to two Al atoms

Chapter 5

on the dehydrated $\gamma\text{-Al}_2\text{O}_3$ (100) surface, provides the most stable adsorption structure.

The adsorption of acetic acid at a higher coverage on the dehydrated $\gamma\text{-Al}_2\text{O}_3$ (110) surface was investigated by increasing the number of acetic acid molecules in the unit cell. For the (110) surface, only two acid molecules are dissociatively adsorbed in a higher coverage configuration (110-Al(1:4)-O(5,12), Figure 5.3) since only 4 Al sites are exposed at the surface. For the case of the (100) surface, 8 Al sites are exposed at the surface and therefore adsorption of up to 4 molecules is investigated (discussed in the next section).

Acetic acid adsorption at higher coverage on the $\gamma\text{-Al}_2\text{O}_3$ (110) surface is found to be a favorable adsorption structure (110-Al(1:4)-O(5,12), -278 kJ/mol, Figure 5.3). However, the adsorption of a consecutive acetic acid molecule becomes less favorable as the coverage increases (shown by the calculation of adsorption energy per consecutive molecule in Table 5.1). The adsorption energy of a second consecutive acid molecule decreases by 70 kJ/mol (from -354 to -284 kJ/mol) when the surface already contains one acid molecule (Table 5.1). Therefore, acetic acid adsorption becomes less favorable with increasing acetic acid coverage on the $\gamma\text{-Al}_2\text{O}_3$ (110) surface, probably until an eventual coverage limit is reached.

Acetic acid adsorption on $\gamma\text{-Al}_2\text{O}_3$ (110) & (100) surfaces...

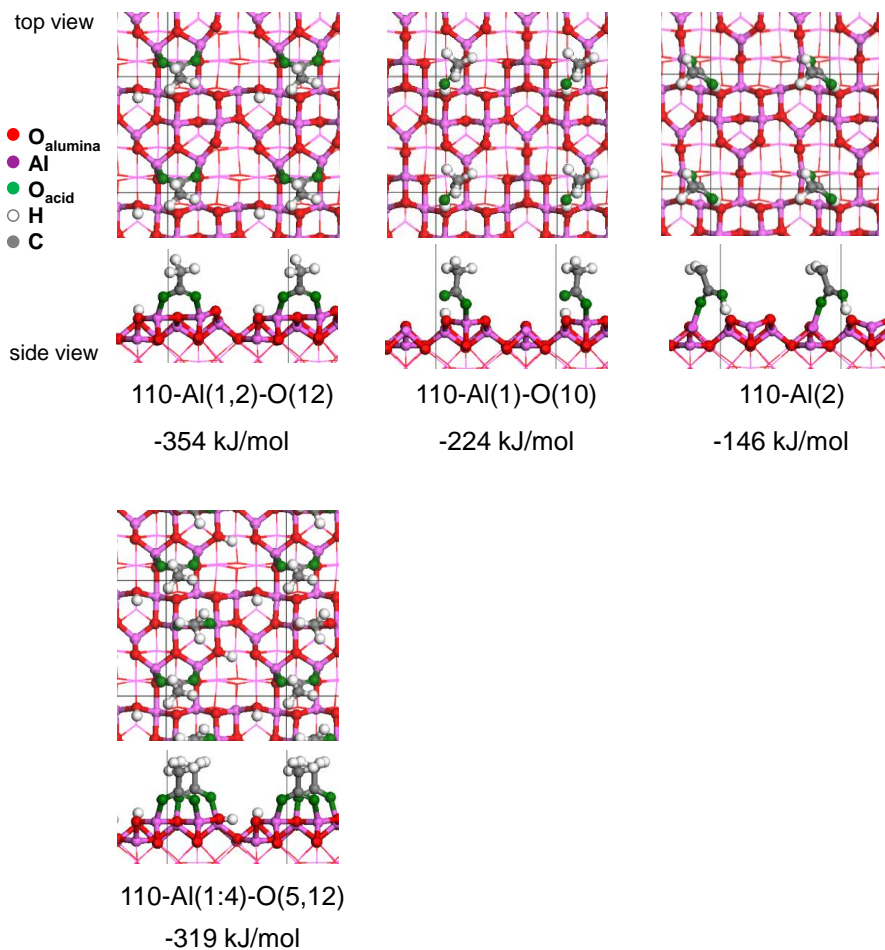


Figure 5.3: Optimized adsorption configurations of acetic acid on the dehydrated $\gamma\text{-Al}_2\text{O}_3$ (110) surface.

Table 5.1: Calculated adsorption energies of consecutive acid molecules on the (110) surface

Adsorption structure ^a	Acid coverage ^b (molecules/nm ²)	E _{ads} / molecule (kJ/mol)	E _{ads} / consecutive molecule ^c (kJ/mol)
110-Al(1,2)-O(12)	1.5	-354	-
110-Al(1:4)-O(5,12)	2.9	-319	-284

^a from Figure 5.3

^b Acid coverage = no. of acetic acid molecules / 0.68 nm² of γ -Al₂O₃

^c E_{ads}/consecutive molecule = [no. of molecules * E_{ads/molecule}]^{higher coverage} - [no. of molecules * E_{ads/molecule}]^{lower coverage}

5.4.2. Acetic acid adsorption on the γ -Al₂O₃ (100) surface

Figure 5.4 shows six optimized configurations of acetic acid on the dehydrated γ -Al₂O₃ (100) surface using the various modes of adsorption.

The largest acetic acid adsorption energy (-198 kJ/mol) is obtained when (i) two O atoms of the acid are coordinated to two Al atoms, Al(1) and Al(2) and (ii) the H atom of the acid has dissociated from the acid molecule to be coordinated to an O atom, O(9) on the γ -Al₂O₃ (100) surface. This is shown by the most stable adsorption structure, 100-Al(1,2)-O(9), in Figure 5.4. This adsorption mode of acetic acid also resulted in the most stable structure on the γ -Al₂O₃ (110) surface (Figure 5.3).

As was the case on the (110) surface, coordination of only one O atom of the acid to an Al atom, as shown by configuration 100-Al(2)-O(4), results in less favorable adsorption (by a difference of 40 kJ/mol). Furthermore, coordination of only one O atom and in the case that the H atom is not dissociated from the acid molecule, as shown by configuration 100-Al(2),

results in the least favorable adsorption (by a difference of 147 kJ/mol). Therefore, as is the case on the (110) surface, dissociative adsorption of acetic acid on the dehydrated γ -Al₂O₃ (100) surface provides the most stable adsorption structure,

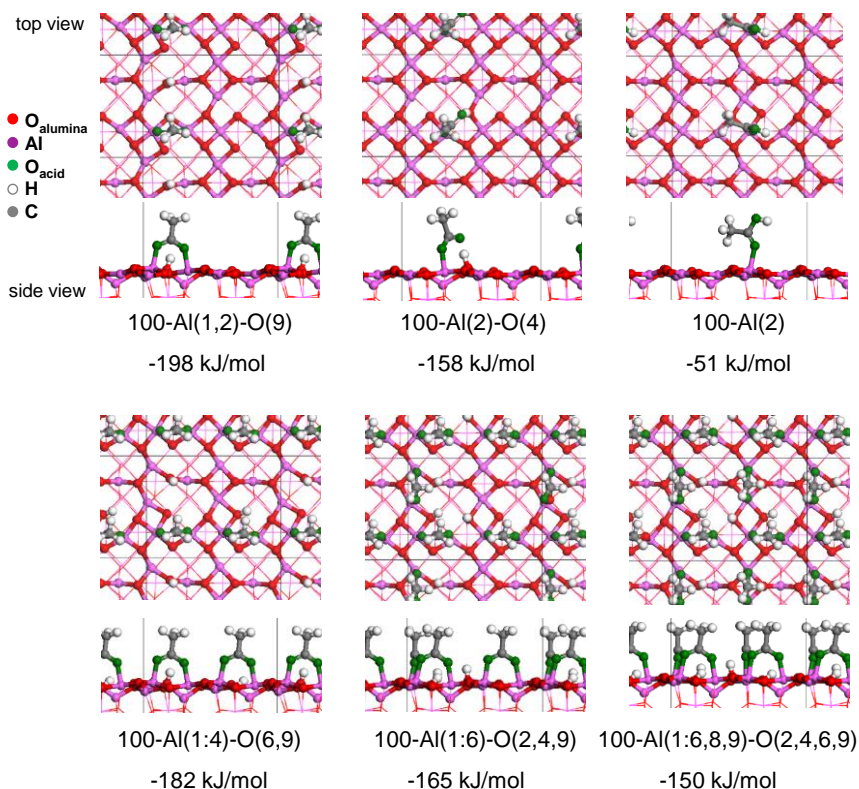


Figure 5.4: Optimized adsorption configurations of acetic acid on the dehydrated γ -Al₂O₃ (100) surface.

For the case of dissociative adsorption with only one O atom coordinated (100-Al(2)-O(4)), the Al(2) site is found to be the most stable site, as adsorption on the Al(1) site is less favorable by 40 kJ/mol (configuration

Chapter 5

100-Al(1)-O(2) in Appendix Figure 5.8). This finding is in agreement with reported energy levels of the surface Lewis acid sites on the (100) surface i.e. the site with the relatively higher Lewis acidity results in more favorable adsorption [15,18].

The adsorption of acetic acid at higher coverages was also investigated on the dehydrated γ -Al₂O₃ (100) surface. Structures, containing 2, 3 and 4 acetic acid molecules, that are dissociatively adsorbed, are shown by configurations 100-Al(1:4)-O(6,9), 100-Al(1:6)-O(2,4,9) and 100-Al(1:6,8,9)-O(2,4,6,9) in Figure 5.4 respectively.

Adsorption structures containing higher coverages are also found to be favorable adsorption structures (e.g. 4 acid molecules, E_{ads} : -150 kJ/mol, Figure 5.4). However, the adsorption of a consecutive acetic acid molecule becomes less favorable as the coverage increases (Table 5.2). For instance, the adsorption energy of a consecutive acid molecule decreases by 32 kJ/mol (=198-166 kJ/mol, Table 5.2) when the surface already contains one acid molecule and decreases by 60 kJ/mol (=165-105 kJ/mol, Table 5.2) when the surface already contains three acid molecules.

In order to estimate the acid saturation coverage, adsorption energy (per consecutive acetic acid molecule adsorbed) as a function of coverage is plotted in Figure 5.5. The higher coverage case of 4.3 molecules/nm² utilizes all Al sites (8) exposed on the (100) surface due to dissociative adsorption of acetic acid molecules. Therefore, further acid adsorption (of a 5th consecutive acid molecule) probably occurs *via* molecular adsorption, which is a significantly weaker adsorption mode. Molecular adsorption of acid was found to result in significantly smaller acetic acid adsorption

energy (100-Al(2), -51 kJ/mol, Figure 5.4). This molecular adsorption case is added to the plot (Figure 5.5) at a coverage of 5.1 molecules/nm² (although calculated at a coverage of 1.1 molecules/nm², it is assumed that molecular adsorption will exhibit the same adsorption energy at a coverage of 5.1 molecules/nm² i.e. -51 kJ/mol). Figure 5.5 suggests that the adsorption of acetic acid becomes significantly less favorable beyond a coverage of 4.3 molecules/nm². In fact, fitting a polynomial functional to all five data points suggests that acetic acid adsorption may become endothermic at a coverage above ~5 molecules/nm².

Table 5.2: Calculated adsorption energies of consecutive acid molecules on the (100) surface

Adsorption structure ^a	Acid coverage ^b (molecules/nm ²)	E _{ads} / molecule (kJ/mol)	E _{ads} / consecutive molecule ^c (kJ/mol)
100-Al(1,2)-O(9)	1.1	-198	-
100-Al(1:4)-O(6,9),	2.1	-182	-166
100-Al(1:6)-O(2,4,9)	3.2	-165	-131
100-Al(1:6,8,9)-O(2,4,6,9)	4.3	-150	-105

^a from Figure 5.4

^b Acid coverage = no. of acetic acid molecules / 0.94 nm² of γ -Al₂O₃

^c E_{ads}/consecutive molecule = [no. of molecules * E_{ads/molecule}]^{higher coverage} - [no. of molecules * E_{ads/molecule}]^{lower coverage}

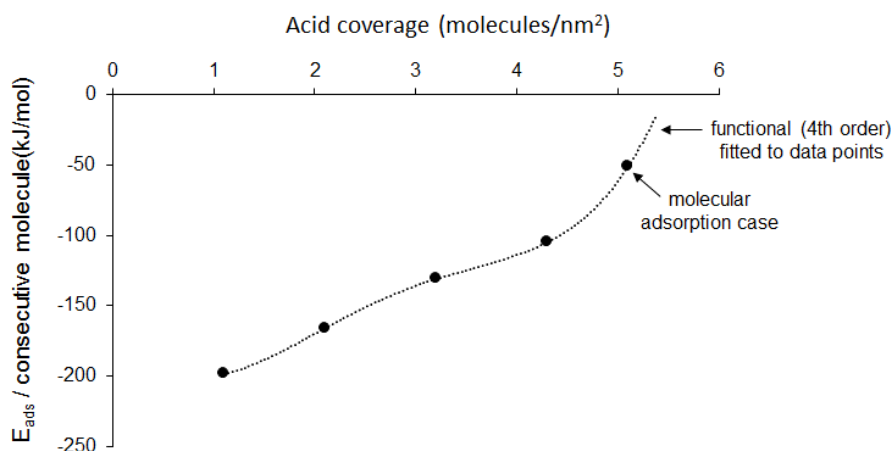


Figure 5.5: Plot of acetic acid adsorption energy (per consecutive acid molecule) vs acid coverage on the γ -Al₂O₃ (100) surface. The five data points are fitted with a polynomial function ($y = 2.5x^4 - 27.9x^3 + 107.6x^2 - 145.4$).

These findings imply that the adsorption of a consecutive acid molecule becomes less favorable, as the surface becomes fully occupied. Molecules could begin to repel each other as the surface becomes occupied due to lateral electronic interactions or induced steric hinderance between molecules. Although the Al sites are fully occupied at a coverage of 4.3 molecules/nm², the saturation coverage on the dehydrated γ -Al₂O₃ (100) surface is deduced to be ~5 molecules/nm².

5.4.3. Acetic acid adsorbed on $\gamma\text{-Al}_2\text{O}_3$: Comparison of IR & DFT results

In Chapter 4, the adsorption of acetic acid on $\gamma\text{-Al}_2\text{O}_3$ was studied in detail experimentally. IR indicated that acetic acid undergoes dissociative adsorption on $\gamma\text{-Al}_2\text{O}_3$, forming an acetate species (Equation 5.3) [19].

(Equation 5.3)

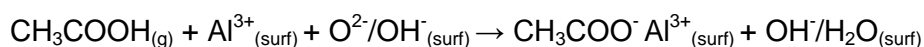


Figure 5.6 shows the IR absorption spectrum of acetate adsorbed on $\gamma\text{-Al}_2\text{O}_3$ (sample prepared experimentally as described in section 5.3.1), which exhibits IR vibrational frequencies that are in agreement with literature reported values [19,20]. Absorption peaks at ~ 1572 & 1469 cm^{-1} are attributed to anti-symmetric ($\nu_a\text{COO}^-$) and symmetric ($\nu_s\text{COO}^-$) carboxylate vibrations, while peaks at 1422 & 1339 cm^{-1} are attributed to δCH_3 vibrations, and peaks at 1053 & 1026 cm^{-1} are attributed to $\rho\text{r}(\text{CH}_3)$ vibrations [19,20].

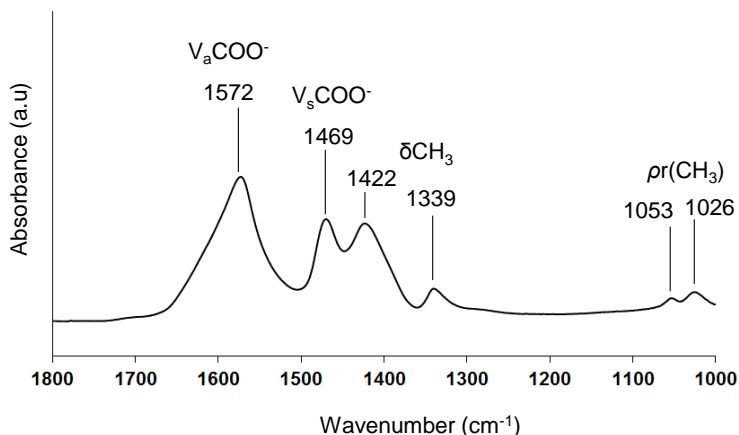


Figure 5.6: Infrared spectrum of acetic acid adsorbed on $\gamma\text{-Al}_2\text{O}_3$.

In the present chapter, the most stable adsorption structures of acetic acid on $\gamma\text{-Al}_2\text{O}_3$ (100) & (110) surfaces were determined using DFT calculations and subsequently vibrational analyses (described in section 5.3.3) were carried out on these structures. In order to elucidate the precise adsorption structure of acetate adsorbed on $\gamma\text{-Al}_2\text{O}_3$, DFT calculated vibrational frequencies are compared to those obtained using IR (Figure 5.6).

5.4.3.1. IR & DFT vibrational frequencies on the $\gamma\text{-Al}_2\text{O}_3$ (110) surface

Table 5.3 compares the IR measured vibrations to DFT calculated vibrational frequencies of chemisorption configurations on the $\gamma\text{-Al}_2\text{O}_3$ (110) surface. Close correlation between IR measured and DFT calculated vibrational frequencies is found for the configuration determined to be the most favorable adsorption structure on the $\gamma\text{-Al}_2\text{O}_3$ (110) surface (110-Al(1,2)-O(12), Figure 5.3). The antisymmetric carboxylate stretch ($\nu_a\text{COO}^-$) is measured at $\sim 1572\text{ cm}^{-1}$ by IR and the DFT calculated value, for configuration 110-Al(1,2)-O(12), is $\sim 1571\text{ cm}^{-1}$. In addition, the symmetric carboxylate stretch ($\nu_s\text{COO}^-$), rotational methyl stretch (δCH_3) as well as rocking methyl vibrations ($\rho_r(\text{CH}_3)$) are all within $\pm 15\text{ cm}^{-1}$ difference between IR measured and DFT calculated values. This indicates a remarkably close correlation between the DFT calculated adsorption structure and that measured experimentally using IR.

Table 5.3: Comparison of IR and DFT calculated vibrational frequencies of adsorbed acetic acid on the γ -Al₂O₃ (110) surface.

Vibrational mode	IR vibration (cm ⁻¹)	DFT calculated vibration		
		110-Al(1,2)-O(12)	110-Al(1:4)-O(5,12)	110-Al(2)
$\nu_a\text{COO}^-$	1572	1571	1572, 1601	1598
$\nu_s\text{COO}^-$	1469	1473	1479, 1442	1442
δCH_3	1422, 1339	1417,1349	1425,1416,1350,1343	1428, 1392
$\rho_r(\text{CH}_3)$	1053, 1026	1038, 1028	1027,1021,1037,1032	1067, 1037

Vibrational frequencies are also comparable for the case of higher acetic acid coverage on the γ -Al₂O₃ (110) surface. Chemisorption configuration 110-Al(1:4)-O(5,12) indicates two antisymmetric (~1572, 1601 cm⁻¹) and two symmetric (~1479,1442 cm⁻¹) carboxylate vibrations, since two acid molecules are adsorbed on the surface, of which both sets of vibrations are comparable to IR measured vibrations (Table 5.3). In this case, the adsorbed acids are coordinated *via* two O atoms to two Al atoms on the γ -Al₂O₃ (110) surface and H is dissociated from the acid molecule. This is also the mode of coordination for the lower coverage case, 110-Al(1,2)-O(12). Therefore, close correlation between IR and DFT calculated vibrational frequencies are obtained in adsorption structures which specifically fit the aforementioned criteria (i.e. a dissociative mode of adsorption).

For the molecular adsorption configuration, (110)-Al(2), the IR measured and DFT calculated vibrations are also comparable. For this configuration,

only one O atom is coordinated to an Al atom on the surface and the H atom is not dissociated from the acid molecule. However, in this case, the H atom of the acid molecule is stabilised by the electronic interaction with the O atom, O(10), on the γ -Al₂O₃ (110) surface (Figure 5.3). Therefore, the strong interaction between the H atom of the acid and the O atom on the surface results in the comparable IR measured and DFT calculated vibrations.

5.4.3.2. IR & DFT vibrational frequencies on the γ -Al₂O₃ (100) surface

Table 5.4 compares the IR measured vibrations to DFT calculated vibrational frequencies of chemisorption configurations on the γ -Al₂O₃ (100) surface. As was the case on the (110) surface, close correlation to IR values is found for configuration 100-Al(1,2)-O(9), which was determined to be the most stable adsorption structure on the γ -Al₂O₃ (100) surface (Figure 5.4). In this case, the IR measured antisymmetric carboxylate stretch ($\nu_a\text{COO}^-$) is found at $\sim 1572\text{ cm}^{-1}$ and the DFT calculated value is $\sim 1582\text{ cm}^{-1}$. In addition, the symmetric carboxylate stretch ($\nu_s\text{COO}^-$), rotational methyl stretch (δCH_3) as well as rocking methyl vibrations ($\rho_r(\text{CH}_3)$) are all within $\pm 15\text{ cm}^{-1}$ difference between IR the measured and DFT calculated values. This, once again, indicates a remarkably close correlation between the DFT calculated adsorption structure and that measured experimentally using IR.

Table 5.4: Comparison of IR and DFT calculated vibrational frequencies of adsorbed acetic acid on the γ -Al₂O₃ (100) surface.

Vibrational mode	IR vibration (cm ⁻¹)	DFT calculated vibration		
		100-Al(1,2)-O(9)	100-Al(1:4)-O(6,9)	100-Al(2)
$\nu_a\text{COO}^-$	1572	1582	1606, 1578	1793
$\nu_s\text{COO}^-$	1469	1466	1472, 1466	1488
δCH_3	1422, 1339	1408, 1352	1425,1422,1349,1346	1405, 1346
$\rho r(\text{CH}_3)$	1053, 1026	1039, 1018	1022,1020,1039,1038	1037, 1017

Vibrational frequencies are also comparable for the case of higher acetic acid coverage on the γ -Al₂O₃ (100) surface. Chemisorption configuration 100-Al(1:4)-O(6,9) indicates two antisymmetric (~1606, 1578 cm⁻¹) and two symmetric (~1472,1466 cm⁻¹) carboxylate vibrations, of which both sets of vibrations are comparable to IR measured vibrations (Table 5.4). These findings suggest that close correlation between IR and DFT calculated vibrational frequencies are obtained in adsorption structures which specifically fit the criteria of dissociative adsorption on both γ -Al₂O₃ (100) and (110) surfaces.

Significant difference to IR vibrational frequencies (± 220 cm⁻¹ for the $\nu_a\text{COO}^-$ vibration) is found for configuration 100-Al(2), which was determined to have the least favorable adsorption of acetic acid on the γ -Al₂O₃ (100) surface (Figure 5.4). This implies that molecular adsorption of acetic acid on the (100) surface is an imprecise description of the experimentally measured adsorption structure. This in contrast to the findings on the γ -Al₂O₃ (110) surface (Table 5.3), where this coordination

mode showed comparable IR and DFT calculated vibrations. On the $\gamma\text{-Al}_2\text{O}_3$ (100) surface, the H atom of the acid molecule is directed away from the surface (Figure 5.4), and is therefore not stabilized by electronic interaction with an O atom on $\gamma\text{-Al}_2\text{O}_3$ as is the case with the (110) surface. This explains the correlation between IR measured and DFT calculated vibrations for molecular adsorption on the $\gamma\text{-Al}_2\text{O}_3$ (110) surface, and the reason for no correlation on the (100) surface.

5.4.4. Surface residence times of acetic acid molecules on the $\gamma\text{-Al}_2\text{O}_3$ (100) & (110) surfaces

In order to determine the length of time that an acid molecule remains adsorbed on the $\gamma\text{-Al}_2\text{O}_3$ surface at FTS temperature, the surface residence times of an acetic acid molecule on both the $\gamma\text{-Al}_2\text{O}_3$ (100) & (110) surfaces is determined (as described in section 5.3.5). Surface residence times, for configurations with the largest and smallest acetic acid adsorption energy on the $\gamma\text{-Al}_2\text{O}_3$ (100) & (110) surfaces, is compared in Table 5.5. Dissociative adsorption on the (110) surface, results in a residence time of $\sim 3 \times 10^{20}$ h, while the relatively weaker molecular adsorption case, results in a residence time of $\sim 5 \times 10^{-2}$ h. Similarly on the (100) surface, dissociative adsorption results in a significantly longer residence time of $\sim 10^4$ h, compared to molecular adsorption ($\sim 6 \times 10^{-12}$ h). Therefore, acetic acid molecules which are bound *via* dissociative adsorption, at FTS temperature (500K), remain adsorbed on the $\gamma\text{-Al}_2\text{O}_3$ surface for significantly long periods of time ($\sim 3 \times 10^{16}$ years in the case of dissociative adsorption on the 110 surface).

Table 5.5: Surface residence times of acetic acid adsorbed on γ -Al₂O₃ (100) & (110) surfaces.

Adsorption structure ^a	Acid coverage (molecules/nm ²)	E _{ads} / molecule (kJ/mol)	Surface residence time ^a (h)
110-Al(1,2)-O(12)	1.5	-354	~ 3 x 10 ²⁰
110-Al(2)	1.5	-146	~ 5 x 10 ⁻²
100-Al(1,2)-O(9)	1.1	-198	~ 10 ⁴ h
100-Al(2)	1.1	-51	~ 6 x 10 ⁻¹²

^acalculated according to Equation 5.2 (section 5.3.5).

5.4.4. Adsorption of water on γ -Al₂O₃ (100) & (110) surfaces

The adsorption of water on the γ -Al₂O₃ (100) & (110) surfaces was investigated and compared to the adsorption strength of acetic acid on the respective surfaces. Figure 5.7 shows the most stable optimized configurations, 100-Al(2)_{OH}-O(4) & 110-Al(3,4)_{OH}-O(4), for one water molecule adsorbed on both dehydrated γ -Al₂O₃ (100) & (110) surfaces respectively. The water molecule undergoes dissociative adsorption on both surfaces. On the (100) surface, the OH group of the water molecule is coordinated to an Al site (Al(2)) on the surface, and the H atom is coordinated to an O atom, O(4). On the (110) surface, the OH group of the water molecule is adsorbed as a bridging species over two Al atoms (Al(3,4) sites), while the H atom is coordinated to an O atom, O(4).

The adsorption energy of a water molecule (-101 kJ/mol, Figure 5.7) is smaller than that of an acetic acid molecule (-198 kJ/mol, Figure 5.4) on the (100) surface (by a difference of 97 kJ/mol). Similarly, the adsorption energy of water (-189 kJ/mol, Figure 5.7) is smaller than that of acetic acid

Chapter 5

(-354 kJ/mol, Figure 5.3) on the (110) surface (by a difference of 165 kJ/mol). The comparatively more exothermic adsorption of acetic acid on both surfaces provides evidence that acetic acid competes with water for adsorption sites on the dehydrated γ - Al_2O_3 surfaces.

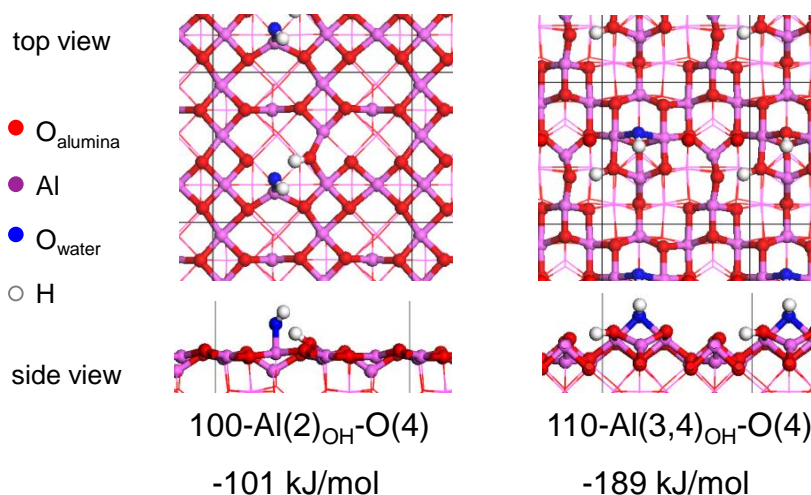


Figure 5.7: Optimized adsorption configurations of water on the dehydrated γ - Al_2O_3 (100) and (110) surfaces.

5.5. Discussion

The precise chemisorption configuration of acetic acid adsorbed on a γ - Al_2O_3 surface is determined by identifying the most stable adsorption structures on the γ - Al_2O_3 (110) and (100) surfaces and comparing DFT calculated vibrations to experimental results (IR). The surface residence times of strongly adsorbed acetic acid, on both γ - Al_2O_3 surfaces, is determined. In addition, the strength of adsorption of acetic acid is compared to that of water on the γ - Al_2O_3 surfaces.

Acetic acid adsorption on two practically representative γ -Al₂O₃ surfaces, the (110) and (100) surfaces, is studied using DFT. Acetic acid favored dissociative adsorption on both γ -Al₂O₃ (100) and (110) surfaces. The largest acetic acid adsorption energy is obtained when (i) two O atoms of the acid are coordinated to two Al atoms on surface and (ii) the H atom of the acid has dissociated from the acid molecule to be coordinated to an O atom on the surface.

Adsorption of acetic acid at higher coverages are also favorable on both γ -Al₂O₃ (100) and (110) surfaces. However, the adsorption of a consecutive acetic acid molecule becomes increasingly less favorable as the coverage increases. For the (100) surface, coverages consisting of up to 4 acid molecules is investigated since this surface exposes more Al atoms (8) in the unit cell compared to the (110) surface (4 Al atoms). Adsorption of acetic acid becomes significantly less favorable beyond a coverage of 4.3 molecules/nm². In fact, acetic acid adsorption is deduced to be endothermic above a coverage of ~5 molecules/nm², which is an indication of saturation coverage on this dehydrated γ -Al₂O₃ (100) surface. This estimation of saturation coverage is reasonable since it is comparable to an experimentally determined saturation coverage. Experimentally, the saturation coverage of acetic acid on is found to contain ~3 molecules of acetate and ~7 molecules of water per nm² of γ -Al₂O₃ (using thermogravimetric data analyses in Chapter 4). This experimentally determined coverage is obtained for acetic acid which is adsorbed on a hydrated γ -Al₂O₃ surface (in which case water molecules occupy some sites on the γ -Al₂O₃ surface). This could be the reason for the difference between the theoretical (~5 molecules/nm²) and experimentally (~3 molecules/nm²) determined acid saturation coverage.

Chapter 5

Close correlation between IR measured and DFT calculated vibrational frequencies is found for the adsorption structures determined to be the most stable (largest acetic acid adsorption energy) on both $\gamma\text{-Al}_2\text{O}_3$ (100) and (110) surfaces. Furthermore, adsorption structures containing acetic acid at higher coverage also shows comparable vibrational frequencies to that of IR and is attributed to the comparable coordination mode of acetic acid in both the lower and higher coverage cases (i.e. a dissociative adsorption configuration).

Surface residence times, for configurations with the largest acetic acid adsorption energy, showed that dissociative adsorption results in residence times of $\sim 3 \times 10^{20}$ h and $\sim 10^4$ h on the $\gamma\text{-Al}_2\text{O}_3$ (110) & (100) surfaces respectively. Therefore, acetic acid remains adsorbed on the $\gamma\text{-Al}_2\text{O}_3$ surface, (at FTS temperature of 500K), for significantly long periods of time ($\sim 3 \times 10^{16}$ years in the case of the 110 surface). In Chapter 4, strongly adsorbed oxygenates were detected on spent Co/Pt/ $\gamma\text{-Al}_2\text{O}_3$ FTS catalyst using infrared (IR) spectroscopy and deduced to be located on the $\gamma\text{-Al}_2\text{O}_3$ support. The spent catalyst samples were obtained from the FTS reactor after 5 and 90 days-on-line, which is shorter than the calculated surface residence times of a strongly adsorbed acetic acid molecule on both the $\gamma\text{-Al}_2\text{O}_3$ surfaces. These findings suggest that an oxygenate molecule, such a carboxylic acid, remains strongly adsorbed on the $\gamma\text{-Al}_2\text{O}_3$ support during the FTS reaction and explains why oxygenates are detected on the spent catalyst after long periods of time-on-line.

An adsorbed water molecule is found to undergo dissociative adsorption on both $\gamma\text{-Al}_2\text{O}_3$ (100) and (110) surfaces. The adsorption of acetic acid is more exothermic than that of water on both dehydrated $\gamma\text{-Al}_2\text{O}_3$ (100) &

(110) surfaces. Interestingly, Feng *et al.* found the reverse to be true for isopropanol adsorption [15]. Water adsorption was reported to be more competitive than isopropanol adsorption on both γ -Al₂O₃ (100) & (110) surfaces. In their study, dissociative and molecular adsorption of isopropanol was identified on the dehydrated (100) surface, while molecular adsorbed isopropanol was found to be thermodynamically most competitive on the (110) surface [15]. These findings suggest that the functional groups of the oxygenate molecule play an important role in determining the strength of adsorption on the γ -Al₂O₃ surface. The larger adsorption energy of a carboxylate molecule compared to an alcohol is probably due to the carboxyl group which strongly interacts with Lewis acidic Al sites and the H atom which can be extracted by basic O atoms on the surface.

The finding that acetic acid adsorption is comparatively more exothermic than water on both surfaces, provides supporting evidence to experimental findings. Experimentally, adsorbed acetate (determined using IR, Figure 5.6) was prepared by impregnating γ -Al₂O₃ with an aqueous solution of acetic acid. Furthermore, acetate molecules were deduced to displace water molecules on pure γ -Al₂O₃ (determined using thermogravimetric data analyses in Chapter 4). These findings imply that acetic acid competes with water for adsorption sites on the γ -Al₂O₃ surface. Cobalt-catalyzed low temperature Fischer-Tropsch synthesis (FTS) is typically operated under several bars of water partial pressure [21], which suggests that the γ -Al₂O₃ surface is significantly hydrated during the reaction. The present study provides both experimental and theoretical evidence that a carboxylic acid (i.e. acetic acid) competes with water and strongly adsorbs on a hydrated γ -Al₂O₃ surface. This provides further evidence that oxygenates can be adsorbed on the support of Co FTS catalyst.

The present study investigated acetic acid adsorption on dehydrated γ - Al_2O_3 surfaces (at 0K). Previous studies have shown that the γ - Al_2O_3 (100) & (110) surfaces contain 8.8 & 8.9-11.8 OH/nm² at 500K respectively [15,18]. Thus, acetic acid adsorption on hydrated γ - Al_2O_3 surfaces should be investigated to compare the strength of acetic acid adsorption with increasing levels of hydration. The coordination mode of acetic acid resulting in the largest adsorption energy on a hydrated alumina surface can then be compared to that on the dehydrated surface. This would elucidate whether acetic acid coordinates (i) to alumina cations (i) *via* a hydroxyl group on the alumina surface or (iii) to both alumina cations and hydrogen atoms of hydroxyl groups on the hydrated alumina surface.

5.6. Conclusion

Acetic acid is strongly adsorbed *via* dissociative adsorption on γ - Al_2O_3 (100) and (110) surfaces, forming an acetate species. Close correlation between IR measured and DFT calculated vibrational frequencies indicate that this is the precise coordination mode of acetic acid on the γ - Al_2O_3 surface. Determination of surface residence times, suggests that acetic acid remains strongly adsorbed on γ - Al_2O_3 for significantly long periods of time. Furthermore, acetic acid competes with water and strongly adsorbs on a hydrated γ - Al_2O_3 surface. These findings support experimental findings that adsorbed oxygenates detected on spent Co/ γ - Al_2O_3 FTS catalyst, are most likely due to strongly bound carboxylic acids located on the γ - Al_2O_3 support.

5.7. Appendix

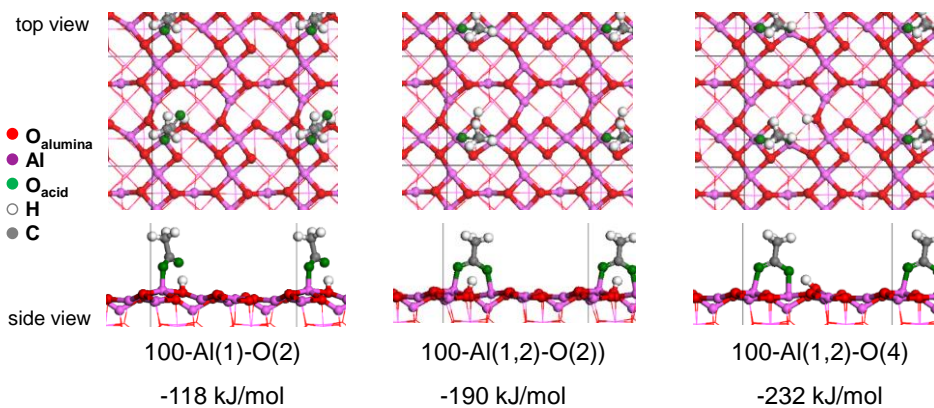


Figure 5.8: Optimized adsorption configurations of acetic acid on the dehydrated γ -Al₂O₃ (100) surface.

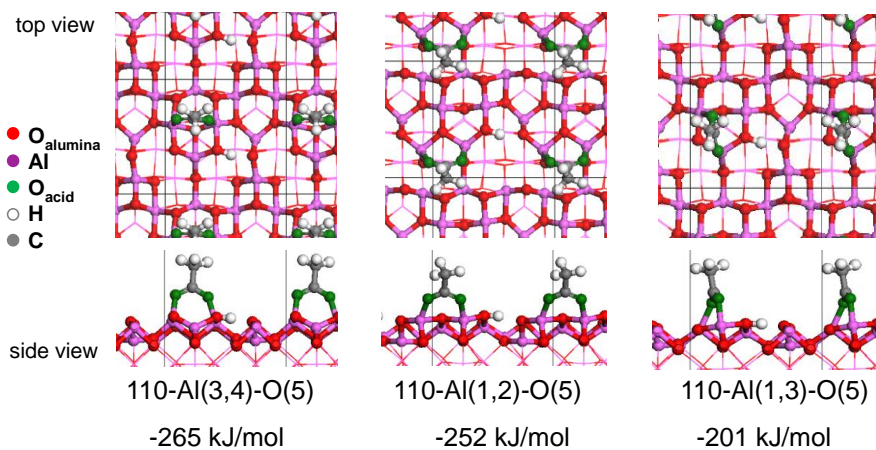


Figure 5.9: Optimized adsorption configurations of acetic acid on the dehydrated γ -Al₂O₃ (110) surface.

Chapter 5

Table 5.6: Comparison of IR and DFT calculated vibrational frequencies of adsorbed acetic acid on the γ -Al₂O₃ (100) surface.

Vibrational mode	IR vibration (cm ⁻¹)	DFT calculated vibration	
		100-Al(1,2)-O(4)	100-Al(1,2)-O(2)
$\nu_a\text{COO}^-$	1572	1580	1590
$\nu_s\text{COO}^-$	1469	1462	1465
δCH_3	1422, 1339	1409, 1350	1431, 1414
$\rho r(\text{CH}_3)$	1053, 1026	1040, 1020	1009, 1020

Table 5.7: Comparison of IR and DFT calculated vibrational frequencies of adsorbed acetic acid on the γ -Al₂O₃ (110) surface.

Vibrational mode	IR vibration (cm ⁻¹)	DFT calculated vibration	
		110-Al(3,4)-O(5)	110-Al(1,3)-O(5)
$\nu_a\text{COO}^-$	1572	1600	1508
$\nu_s\text{COO}^-$	1469	1474	1445
δCH_3	1422, 1339	1426, 1349	1425, 1335
$\rho r(\text{CH}_3)$	1053, 1026	1026, 1035	1050, 1037

5.8. References

- [1] X. Krokidis, P. Raybaud, A.-E. Gobichon, B. Rebours, P. Euzen, H. J. Toulhout, *Phys. Chem. B* 105 (2001) 5121.
- [2] S. J. Wilson, *J. Solid State Chem.* 30 (1979) 247.
- [3] N. A. Deskins, D. Mei, M. Dupuis, *Surf. Sci.* 603 (2009) 2793.
- [4] A. Motta, I. L. Fragala, T. J. Marks, *J. Am. Chem. Soc.* 130 (2008) 16533.
- [5] J. Handzlik, P. Sautet, *J. Catal.* 256 (2008) 1.
- [6] J. H. Kwak, D. Mei, C. -W. Yi, D. H. Kim, C. H. F. Peden, L. F. Allard, J. Szanyi, *J. Catal.* 261 (2009) 17.
- [7] M. Valero, P. Raybaud, P. Sautet, *J. Phys. Chem. B* 110 (2006) 1759.
- [8] J. Joubert, F. Delbecq, C. Thieuleux, M. Taoufik, F. Blanc, C. Coperet, J. Thivolle-Cazat, J.-M. Basset, P. Sautet, *Organometallics* 26 (2007) 3329.
- [9] M. Digne, P. Raybaud, P. Sautet, D. Guillaume, H. Toulhout, *J. Am. Chem. Soc.* 130 (2008) 11030.
- [10] M. Digne, P. Raybaud, P. Sautet, D. Guillaume, H. Toulhout, *Phys. Chem. Chem. Phys.* 9 (2007) 2577.
- [11] J. Joubert, A. Salameh, V. Krakoviack, F. Delbecq, P. Sautet, C. Coperet, J.-M. Basset, *J. Phys. Chem. B* 110 (2006) 23944.
- [12] C. Chizallet, P. Raybaud, *Angew. Chem. Int. Ed.* 48 (2009) 2891.
- [13] J. P. Beaufils, Y. Barbaux, *J. Chim. Phys.* 78 (1981) 347.
- [14] P. Nortier, P. Fourre, A.B. Mohammed Saad, O. Saur, J.C. Lavally, *Appl. Catal.* 61 (1990) 141.
- [15] G. Feng, C-F. Huo, C-M. Deng, L Huang, Y-W. Li, J. Wang, H. Jiao, *J. Mol Catal. A: Chem* 304 (2009) 58–64.
- [16] Z. Frenkel, *Physik*, 26, (1924) 117.
- [17] M. H. Hablanian, *High-Vacuum Technology, A practical Guide*, 2nd Ed, Marcel Dekker Inc, New York, 1997, 27
- [18] M. Digne, P. Sautet, P. Raybaud, P. Euzen, H. Toulhoat, *J. Catal.* 226 (2004) 54.

Chapter 5

- [19] M. A. Hasan, M.I. Zaki, L. Pasupulety, *Appl. Catal. A*, 243 (2003) 81–92.
- [20] K. Nakamoto, *Infrared Spectra of Inorganic and Coordination Compounds*, Wiley/Interscience, London, 1970, pp. 220–224.
- [21] J. van de Loosdrecht, F. G. Botes, I. M. Ciobica, A. Ferreira, P. Gibson, D. J. Moodley, A. M. Saib, J. L. Visagie, C. J. Weststrate, J. W. Niemantsverdriet, Fischer-Tropsch synthesis: catalysts and chemistry, In J. Reedijk & K. Poeppelmeier (Eds.), *Comprehensive Inorganic Chemistry II (Second Edition): from elements to applications* Elsevier, Amsterdam, 2013, 525-557.

6

Conclusions and outlook

6.1. Introduction

Cobalt catalysts are preferred for the gas-to-liquids process in large-scale commercial Fischer-Tropsch synthesis (FTS) plants. As is the challenge faced with many catalysts, the Co FTS catalyst deactivates with time on line [1]. The economics of the gas-to-liquids process is strongly dependent on the stability of the catalyst. Understanding catalyst deactivation mechanisms is crucially important because the insight gained can be used to improve catalyst stability and inspire rational design of future catalysts.

Cobalt is active for FTS in the metallic state [2]. Loss of active metal surface area, leading to deactivation, could occur in number of different ways, including (i) poisoning by sulphur and/or nitrogen compounds, (ii) oxidation of the active cobalt metal, (iii) cobalt-support compound formation, (iv) surface reconstruction, (v) carbon deposition and (vi) sintering of cobalt crystallites [1,3,4]. Of these postulated mechanisms, carbon deposition and sintering is deduced to be particularly important under typical Co FTS conditions [1].

The industrial catalyst is often too complex to obtain 'atomic level' structural, morphological and compositional detail of a catalytic process. Planar model catalysts provide well-defined, controllable and convenient representations of real catalysts. Highly informative techniques, such x-ray photoelectron spectroscopy (XPS) and transmission electron microscopy (TEM), are often not easily applied to industrial catalysts, but well-suited to model catalysts with flat surfaces and nanoscale variations in height [5].

In this thesis, a model catalyst is exposed to realistic Co FTS temperature and pressure and characterized using TEM and XPS. In this way, the dominant sintering mechanism during Co-catalysed FTS is elucidated.

Model systems were further utilized in a study of carbon formation during Co FTS. Model compounds as well as real catalyst samples are exposed to model FTS conditions and characterized using temperature-programmed techniques coupled with mass spectrometry (TP-MS). This was done to ascertain whether carboxylic acids deposit carbon that is detrimental for FTS activity and subsequently cause catalyst deactivation.

6.2. Objective of this chapter

The objective of this chapter is to evaluate the results presented in this thesis in the context of the Co FTS catalyst deactivation research field. Future work to progress the understanding on the respective research topics is proposed and in some cases is based on preliminary experimental results.

6.3. Ostwald ripening on a planar Co/SiO₂ model catalyst exposed to model Fischer-Tropsch synthesis conditions

Loss of metal surface area, commonly referred to as 'sintering', has been established as a mechanism of Co FTS catalyst deactivation [1]. To our knowledge, direct evidence of the mechanism of loss of metal surface area during Co FTS has not been previously reported.

The planar Co/SiO₂ model catalyst is used to uncover the mechanism of loss of metal surface area at the single-particle level (Chapter 3). A novel feature of this work is the exposure of the model catalyst to Fischer-Tropsch synthesis (FTS) conditions of pressure (20 bar_(a)), temperature

(230°C) and gas atmosphere (dry H₂/CO, low conversion) using a custom-designed high pressure treatment cell. Another unique feature of the work is the employment of the planar model support, SiO₂/Si₃N₄, which is custom-made for TEM analysis and is compatible with the technique employed to mimic industrial catalyst preparation i.e. spin-coating deposition. The planar model support enables TEM measurement of the same area of the support before and after exposure to FTS conditions (i.e. identical location TEM is employed).

6.3.1 Conclusions on the loss of metal surface area

In the literature, a particle migration and coalescence mechanism has been proposed for the loss of metal surface area during Co-catalyzed FTS [6,7]. However, these conclusions were based on indirect evidence, using the change in shape of the particle size distribution from the fresh to the spent catalyst. In the present study, the dominant mechanism for the loss of metal surface is directly observed using the model catalyst in TEM studies (i.e. identical location TEM). Loss of metal surface area is found to proceed *via* an atomic migration (Ostwald ripening) mechanism. The TEM micrographs of the same area before and after FTS show (i) rapid loss (within 10h) of most smaller particles (≤ 4 nm Co metal), (ii) a decrease in size of somewhat larger particles (size decreases from ~ 5 nm to 2nm) and (iii) all remaining particles are immobile during the reaction. Complementary x-ray photoelectron spectroscopy (XPS) analyses confirmed the loss of metal surface area after exposure to FTS conditions. An additional finding is that loss of metal surface area requires the presence of CO in combination with H₂ gas. This led to the conclusion that the mechanism of loss of metal

surface area proceeds *via* a mobile cobalt-subcarbonyl species that is transported *via* diffusion over the support surface from the smaller to relatively larger particles.

Industrial catalysts typically exhibit a wide particle size distribution of the active phase. For FTS on such a catalyst, loss of metal surface area alone does not necessarily mean loss of activity, due to the size-dependent reactivity of Co in FTS. For instance, Bezemer *et al.* reported that particles smaller than 6-8nm exhibit low activity [8] and hence their loss would not greatly affect the observed FTS activity. In the present study, the loss of ~4nm particles was observed within the reaction time of 10h, while some particles of ~5nm were observed to decrease in size. This implies that particles larger than 5nm, which may be optimum for FTS activity, could become smaller with longer reaction times. Therefore, atomic migration of cobalt could contribute to catalyst deactivation.

Experimental details needs to be carefully considered when generalizing the loss of metal surface area that is found in a specific reaction environment. Therefore, it is proposed that the influence of additional factors should be investigated further, in particular (i) the effect of higher water partial pressure during FTS (ii) the influence of support substrate roughness, defect density and chemical nature (iii) the influence of promoters and (iv) reaction time.

In the present study, although realistic pressures, synthesis gas ratio and temperature is used, the conversion is negligible due to the small quantity of Co present on the flat model sample and the relatively high reactant flow (i.e. a very high space velocity). The largest consequence of this is that the water partial pressure is unrealistically low (~4-6 bar of water partial

pressure is expected during commercial operation of FTS [1]). Previous studies have shown that higher water partial pressures can indeed cause an increase in loss of metal surface area [9,10]. The effect of higher water partial pressure can be carried out as future work on this topic by modifying our current high-pressure cell experimental set-up such that several bars of water are co-fed during exposure of the model catalyst to FTS conditions.

6.3.2. Outlook: the effect of promoter & reaction time

Co FTS catalysts typically contain a promoter to aid reduction of the cobalt oxide that is present after catalyst preparation. Pt is among the frequently used promoters employed in Co/Al₂O₃ FTS catalysts. To study the factors of promoter and longer reaction time simultaneously, a planar Co/Pt/SiO₂ model catalyst (Co:Pt molar ratio of 50:1) was prepared and exposed to model FTS conditions (20 bar_a, dry H₂/CO (2/1), 230°C) for 120h. This is significantly longer than the reaction time used for the promoter-free case discussed in Chapter 3 (i.e. 10h). Identical location TEM is carried out before and after exposure to FTS conditions. The TEM results obtained from this single experiment are shown in Figure 6.1. These images allow for several interesting observations. The micrographs show that (i) some smaller particles of ~4nm are lost, (ii) particles which remain are immobile, (iii) some particles have decreased in size (for instance, from ~7nm to 3nm and (iv) some particles have decreased in size (from ~6nm) leaving behind tiny features of (~ 1nm) and (iv) some, but not all particles which are in close proximity to each other (blue circles, Figure 6.1), appear to be merging.

Although these results were obtained in a single experiment and need to be reproduced to validate this data, some interesting observations can be made. Firstly, the dominant mechanism of loss of metal surface area, during this reaction at longer time, is still observed to be Ostwald ripening. As was the case with the 10h experiments, smaller particles are lost, some particles are observed to decrease in size and remaining particles are observed to be immobile during the reaction (Figure 6.1). These findings are indicative of an Ostwald ripening mechanism. The random movement of particles over the surface resulting in collision and merging of particles is not observed. Therefore, a particle migration and coalescence mechanism is not significant under the reaction conditions used.

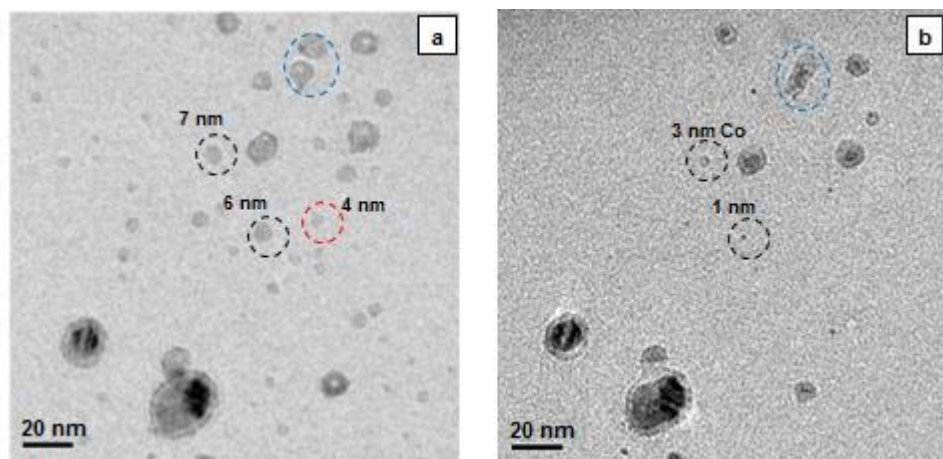


Figure 6.1: TEM images of Co/Pt/SiO₂ model catalyst (a) reduced-passivated and (b) after exposure to FTS conditions (230°C, 20 bar H₂/CO (2/1) for 120h) followed by passivation. The black circles indicate particles which have decreased in size, red circles indicates particles which are completely lost and blue circles indicate particles which appear to be merging.

Chapter 6

Furthermore, the longer reaction time (120h) has affected relatively larger particles (up to ~7nm Co metal size) (Figure 6.1). This specific result is of particular importance since it demonstrates that not only smaller particles sizes, but also larger particles are affected by atomic migration during FTS.

Interestingly, some particles decrease in size and in each case leaves behind a very small feature (~1nm) after exposure to FTS conditions (Figure 6.1). These are possibly very small Co particles, but are more likely to be Pt particles as these features are not observed in the Pt-free case (discussed in Chapter 3). In the case that these small particles are Pt, this presents a particularly interesting observation since it implies that atomic Co species (Co sub-carbonyls) are mobile during FTS, but Pt atoms are less mobile and do not easily migrate over the support surface.

The merging of two particles is an interesting observation as well. Firstly, the process resulting in this merging is slow, since it is only halfway complete after 120h (Figure 6.1b). Secondly, cobalt is observed at the same location (i.e. immobile during the reaction), therefore the neck formation indicates atomic transport between the two stationary particles (blues circle in Figure 6.1b). Although, such particle morphologies are typically interpreted as the occurrence of a particle migration and coalescence mechanism, the present study provides evidence that it is the result of atomic rather than particle migration.

The findings from the experiment described in the present section warrants further investigation into the impact of time and promoter on the loss of metal surface area during Co FTS, as several interesting and relevant observations are made.

6.3.3. Outlook: the effect of support nature

Future work on the loss of metal surface area during FTS should also include an investigation into the influence of support material. An Al_2O_3 model support provides a relevant comparison to the commercial $\text{Co}/\text{Al}_2\text{O}_3$ cobalt catalyst. This topic was briefly explored by depositing a thin film of Al_2O_3 (~3nm thickness) on the $\text{SiO}_2/\text{Si}(100)$ substrate using atomic layer deposition (ALD).

Cobalt oxide nanoparticles were deposited onto the planar $\text{Al}_2\text{O}_3/\text{SiO}_2/\text{Si}(100)$ model support by spin-coating of a cobalt nitrate polymer mixture followed by calcination (similar to the procedure followed for the $\text{SiO}_2/\text{Si}(100)$ case). Two typical TEM images of the $\text{Co}/\text{Al}_2\text{O}_3/\text{SiO}_2/\text{Si}(100)$ model catalyst in the reduced and passivated form are shown in Figure 6.2. The cobalt nanoparticles exhibit no significant agglomeration and particles sizes range between 5-20 nm (as was the case on the $\text{SiO}_2/\text{Si}(100)$ support). Therefore, this model catalyst, containing an alumina substrate, would be suitable for further use in a sintering study. Challenges in utilizing this model catalyst in sintering studies include a lower extent of reduction on the alumina substrate as there could be greater metal-support interaction compared to the silica substrate. This also means that the disappearance of particles due to the formation of cobalt-aluminate compounds [11] needs to be considered, unlike the case of the planar Co/SiO_2 model support, where metal-support compounds formation was found to be negligible (Chapter 3 section 3.3.1.3)

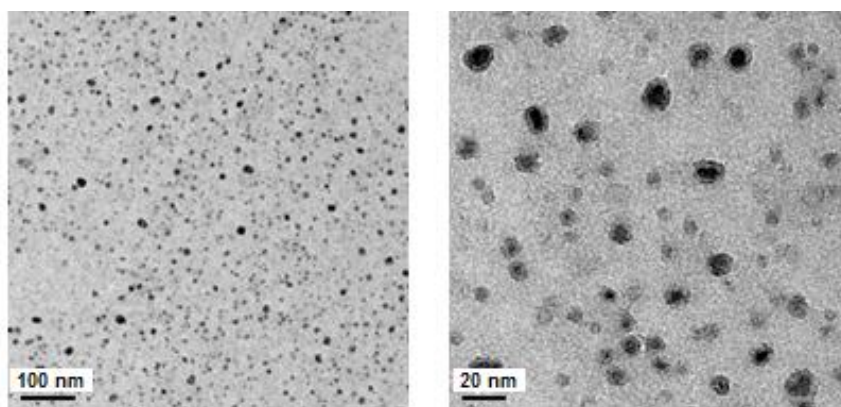


Figure 6.2: TEM images of the reduced and passivated Co/Al₂O₃/SiO₂/Si(100) model catalyst.

6.3.4. Outlook: the effect of particle size and distribution

For the sintering study described in Chapter 3, cobalt oxide nanoparticles are prepared by spin-coating of a polymer mixture containing cobalt nitrate onto the model support, followed by calcination. This procedure produces a wide distribution of particle sizes and interparticle distances. An alternative method to prepare the model catalyst is to pre-form the cobalt (oxide) nanoparticles in a colloidal solution and then spin-coat the particles onto the model support. To investigate this method, cobalt oxide (Co₃O₄) nanoparticles were synthesized in a colloidal solution by the procedure described by Chou *et al.* [12]. These pre-formed particles were then deposited on the SiO₂/Si(100) support by spin-coating. Figure 6.3 shows the TEM images of the resulting model catalyst with nanoparticles directly deposited (Figure 6.3 (a)) and after a reduction followed by a passivation treatment (Figure 6.3 (b)). The pre-formed particles have irregular shapes in the calcined state, but change (as expected) to a more uniform spherical

shape after reduction. The nanoparticles appear as shell-type structures after reduction then passivation, but this is a consequence of a harsh passivation, which causes partial re-oxidation of the particles. The particle size in the reduced, passivated form is ~8-10 nm (i.e. with the passivation layer included).

The important result is that a narrower particle size distribution is observed and the interparticle spacing appears to have good uniformity. This implies that this model catalyst, containing pre-formed nanoparticles, can be used in a sintering study which focuses on the effect of particle size, particle size distribution and inter-particle spacing.

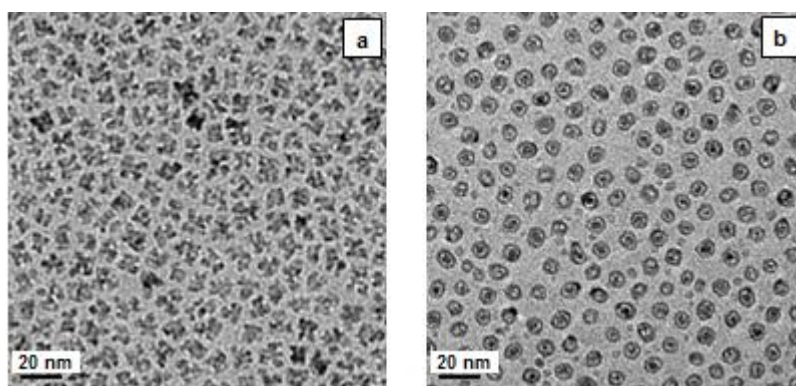


Figure 6.3: Pre-formed cobalt oxide nanoparticles on the model $\text{SiO}_2/\text{Si}(100)$ support (a) directly deposited and (b) after reduction then passivation.

6.4. The role of carboxylic acids in Co Fischer-Tropsch synthesis catalyst deactivation

Polymeric carbon deposited on Co/Al₂O₃ catalyst can negatively impact FTS activity [13]. Oxygenate compounds, such as carboxylic acids, ketones and esters are produced as side products during FTS. To our knowledge, oxygenates have not previously been investigated as potential precursors for polymeric carbon on Co FTS catalyst.

Previous studies have reported that spent Co/Al₂O₃ FTS catalyst contain oxygenated compounds, such as carboxylic acids and alcohols (determined using infrared (IR) spectroscopy) [14,15]. Oxygenated compounds were deduced to be adsorbed on the γ -Al₂O₃ support (using IR) [14].

Chapter 4 describes the potential contribution of FTS-produced carboxylic acids to Co FTS catalyst deactivation. Specifically, carbon deposition due to acid decomposition on Co/Pt/ γ -Al₂O₃ FTS catalyst has been studied and the location of adsorbed oxygenate on spent catalyst has been identified. Finally, to directly observe the impact of acids on deactivation, acid has been co-fed during FTS using a Co/Pt/Al₂O₃ catalyst in a continuous-stirred tank reactor (CSTR) operated at commercially relevant conditions.

Chapter 5 describes the chemisorption of a carboxylate compound, acetic acid, on two representative γ -Al₂O₃ surfaces using Density Functional Theory (DFT). DFT calculated vibrational frequencies are compared to measured IR data to determine the precise adsorption structure. Determination of surface residence times and comparison of adsorption strength of acetic acid and water on the two most abundant γ -Al₂O₃ surfaces, (100) and (110), provides insight into the strong adsorption of carboxylate on the γ -Al₂O₃ support.

6.4.1. Conclusions on the role of carboxylic acids in Co Fischer-Tropsch synthesis catalyst deactivation

Adsorbed oxygenates detected on spent Co/ γ -Al₂O₃ FTS catalyst are predominantly located on the γ -Al₂O₃ support. The formation of a metal-carboxylate compound is not detected (using IR) and is in fact unlikely, since acetic acid decomposes at low temperature on a Co metal surface (inferred from ultra-high vacuum single crystal experiments).

Both short (acetate) and longer chain (octanoate) carboxylates are chemisorbed on pure γ -Al₂O₃ and are thermally stable at Co FTS temperature under synthesis gas (IR and XPS analyses). Comparison of DFT calculated to IR measured vibrational frequencies indicates that the most stable chemisorption structure of acetic acid on the γ -Al₂O₃ surface is dissociative (i.e. an acetate species is formed *via* coordination of both oxygen atoms of the acid to two aluminium ions on the support). These chemisorption structures correspond to high adsorption energies (-354 kJ/mol on the γ -Al₂O₃ (110) surface) and significantly long surface residence times for an adsorbed acetic acid molecule ($\sim 3 \times 10^{16}$ years predicted for the case of adsorption on the 110 surface). These theoretical findings support experimental findings, since carboxylates (both acetate and octanoate) decompose, rather than desorb, above 300°C on pure γ -Al₂O₃ (determined using temperature-programmed techniques coupled with mass spectrometry (TP-MS)). These findings suggest that carboxylates are practically irreversibly adsorbed on the γ -Al₂O₃ support of the catalyst during FTS (i.e. at temperature of ~ 200 -230°C under synthesis gas).

Chapter 6

Acetic acid adsorbs on $\gamma\text{-Al}_2\text{O}_3$ in an aqueous medium (IR), which implies that the acid competes with water for adsorption on $\gamma\text{-Al}_2\text{O}_3$. Further evidence for this is provided by thermogravimetric analyses (TGA) data, where a lower water coverage is found on $\gamma\text{-Al}_2\text{O}_3$ with acetate adsorbed compared to pure $\gamma\text{-Al}_2\text{O}_3$ (i.e. ~ 3 acid molecules displace 6 water molecules per nm^2 of $\gamma\text{-Al}_2\text{O}_3$). DFT calculations confirmed this competitive adsorption since the adsorption of acetic acid is found to be more exothermic than that of water on both $\gamma\text{-Al}_2\text{O}_3$ (110) and (100) surfaces. Therefore, the theoretical and experimental findings imply that acetic acid chemisorbs on a hydrated $\gamma\text{-Al}_2\text{O}_3$ surface, which is the expected state of the surface during FTS. The strength of adsorption of a carboxylate and the long residence time of an acid molecule on the $\gamma\text{-Al}_2\text{O}_3$ surface, explains why oxygenated compounds are detected on spent Co FTS catalyst (both 5 and 90 day old samples).

Thermal decomposition of acetic acid over reduced Co/Pt/ Al_2O_3 catalyst, at model FTS conditions (i.e. 1 bar_(a) $\text{H}_2/\text{CO}:2/1$ at 230°C), deposits predominantly atomic carbon on the catalyst (TPH-MS). Atomic carbon is more easily hydrogenated during FTS, unlike polymeric carbon which was previously found to be detrimental for FTS activity [11]. Interestingly, acetic acid decomposed over pure $\gamma\text{-Al}_2\text{O}_3$ does produce polymeric carbon (TPH-MS), but requires temperatures significantly above that of Co FTS. This implies that in the case of the model experiment using Co/Pt/ Al_2O_3 catalyst, atomic carbon formation is mostly due to acid decomposition over the metal surface. In fact, single crystal experiments showed that acetic acid decomposes at low temperature (120°C) over a Co(0001) surface, producing surface carbon. These findings imply that either (i) the interaction of acetic acid and cobalt metal dominates (probably dependent on the

metal loading of the sample) or (ii) the Co metal changes the thermal stability and/or decomposition pathway of carboxylate adsorbed on $\gamma\text{-Al}_2\text{O}_3$ support. A possible mechanism for the latter case is the activation of hydrogen on the Co metal surface which migrates onto the $\gamma\text{-Al}_2\text{O}_3$ support (H_2 spill-over), enabling carboxylate decomposition at lower temperatures.

Co-feeding of excess acetic acid, to either fresh or spent catalyst, during FTS did not enhance Co/Pt/ Al_2O_3 catalyst deactivation. Although it was found that carboxylic acids can cause atomic carbon deposition (presumably on the cobalt surface) and they are chemisorbed on $\gamma\text{-Al}_2\text{O}_3$ support, this does not significantly impact Co FTS catalyst deactivation.

6.4.2. Outlook: effect of oxygenate molecule and reaction time

Although the present study provides evidence that carboxylic acids do not significantly impact catalyst deactivation, further considerations need to be taken into account. These include (i) the reaction time of the co-feeding experiments, (ii) the type of oxygenate molecule studied for carbon formation and during co-feeding experiments and (iii) the impact of adsorbed carboxylate on the hydrophobicity of the $\gamma\text{-Al}_2\text{O}_3$ support.

Findings from the present study do not exclude the possibility that the atomic carbon, formed due to carboxylate decomposition, transforms into detrimental carbon with time during FTS. This can only be tested by carrying out acid co-feeding experiments during FTS over extensively long reaction times (i.e. months) and incorporating atypical or upset conditions (such as high temperatures and low H_2/CO ratio) during the experiments.

Furthermore, different oxygenate molecules should be used in studies of deposition of polymeric carbon on cobalt catalyst and in co-feeding experiments. Carboxylic acids contain functional groups which strongly coordinate to alumina support and explains why oxygenate compounds are observed on spent Co FTS catalyst. The detection of these oxygenates, and the fact that acetic acid is typically found in the highest concentration in Co FTS, is the reason that acetic acid was used in the model studies and acid co-feeding experiments of the present study. However, other oxygenated compounds, albeit typically found in low concentrations, could be the precursors for polymeric carbon. For instance, esters, ketones and long chain carboxylic acids are also produced during FTS and could decompose over the cobalt catalyst leading to polymeric carbon formation. Even small amounts of polymeric carbon formed from these species can lead to deactivation, especially if they preferentially adsorb on metal sites that are critical for FTS activity.

6.4.3. Outlook: Probing changes in hydrophobicity due to carboxylate adsorption

Adsorbed oxygenates detected on spent Co/ γ -Al₂O₃ FTS catalyst are found to be located on the γ -Al₂O₃ support. The chemisorption of these compounds suggests that the support is essentially modified during FTS. For instance, octanoic acid adsorbed on γ -Al₂O₃ changes the support surface from hydrophilic to hydrophobic. The carboxylate group of the acid coordinates to the Al cations of the support, while the long, α -polar alkyl group does not interact with the support surface and extends inside the support pore. This could change the local polarity at the support surface

and consequently the interaction of the support with water. This hypothesis was tested by studying the affinity of an octanoate-modified $\gamma\text{-Al}_2\text{O}_3$ sample toward solvents of different polarity (see footnote⁷). This was compared with the affinity of pure $\gamma\text{-Al}_2\text{O}_3$ toward the respective solvents.

Figure 6.4 shows photographs as well as schematic representations, of fresh $\gamma\text{-Al}_2\text{O}_3$ (Figure 6.4a) and octanoate-modified $\gamma\text{-Al}_2\text{O}_3$ (Figure 6.4b) in physical mixtures of water (hydrophilic phase) and hexane (hydrophobic phase). The support particles are hydrophilic before any acid modification (Figure 6.4a), and are therefore observed to be in the water phase and not in the non-polar hexane phase. However, upon modification by octanoic acid (Figure 6.4b), the $\gamma\text{-Al}_2\text{O}_3$ particles have an increased affinity for the hydrophobic solvent as they appear to be suspended in the hexane phase. These images show that the $\gamma\text{-Al}_2\text{O}_3$ has changed from hydrophilic to hydrophobic due to carboxylate adsorption.

Similar experiments were carried out using fresh Co/Pt/ $\gamma\text{-Al}_2\text{O}_3$ FTS catalyst (Figure 6.4c) and spent catalyst that underwent a wax extraction procedure (as described by Moodley *et al.*) [13] (Figure 6.4d). As determined in Chapter 4, spent catalyst contains strongly adsorbed oxygenated compounds, such as carboxylic acids, located on the $\gamma\text{-Al}_2\text{O}_3$ support. Figure 6.4 shows that the spent catalyst exhibits an increased hydrophobicity compared to fresh catalyst, which suggests that the catalyst changes from hydrophilic to hydrophobic when oxygenates are adsorbed during FTS. A further consideration in this case is that the residual wax in the pores of the

⁷ Hydrophobicity experiments carried out by C.J. Weststrate at the Eindhoven University of Technology.

Chapter 6

spent catalyst (remaining after wax extraction) contributes to this observation of increased hydrophobicity.

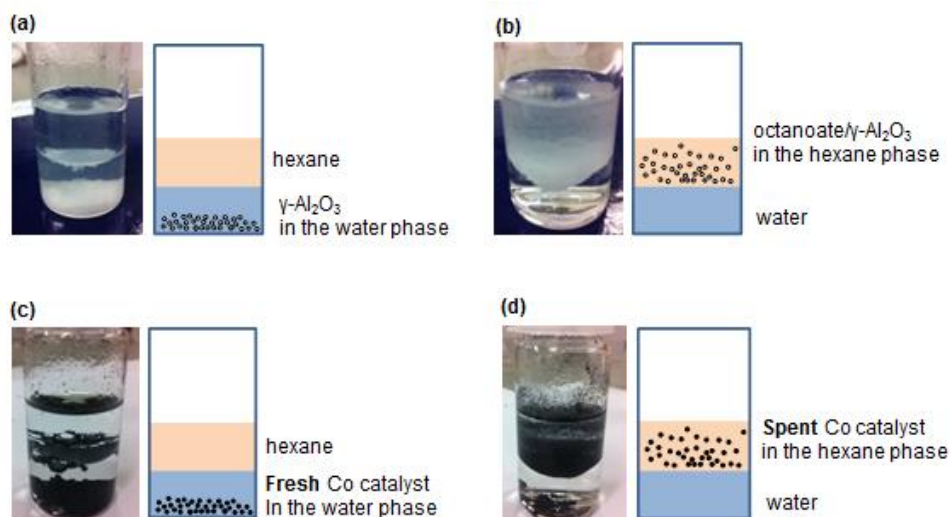


Figure 6.4: Images with schematic representations of physical mixtures of hexane and water containing (a) γ -Al₂O₃, (b) octanoate/ γ -Al₂O₃, (c) fresh Co/Pt/ γ -Al₂O₃ catalyst and (d) spent wax-extracted Co/Pt/ γ -Al₂O₃ catalyst.

These experiments imply that oxygenates adsorbed on the catalyst support during FTS (as well as residual wax), results in a support with increased hydrophobicity. Consequently, the local water partial pressure as 'seen' by the Co particle could decrease due to carboxylate adsorption during FTS. The increased hydrophobicity may also induce effects on the diffusion of FTS products into and out of support pores. Hydrocarbons could experience longer residence times in support pores, since they would have an affinity toward a hydrophobic environment. This build of hydrocarbons

could then lead to pore blocking, induce product or reactant gas diffusion limitations and in this way impact FTS performance. Experiments to test these hypotheses include (i) impregnating the catalyst with long chain carboxylates (e.g. octanoic acid) then observing the impact on FTS performance and (ii) co-feeding longer chain carboxylates during FTS.

6.5. Concluding remarks on fundamental understanding of cobalt Fischer-Tropsch synthesis catalyst deactivation

The research questions addressed in this thesis originate from challenges currently faced during commercial operation of Co-catalysed FTS. Specifically, fundamental understanding on two catalyst deactivation pathways has been obtained. Planar model catalyst systems, well suited to advanced spectroscopic and microscopic techniques, are exposed to commercially relevant reaction conditions and the findings translated back to identify solutions to the challenges faced when using industrial catalysts.

In this thesis, two important mechanisms of Co FTS catalyst deactivation are studied i.e. (i) sintering of small crystallites leading to the loss of metal surface area and (ii) deposition of polymeric carbon from FTS-produced carboxylic acids leading to the blocking of active metal sites. For both deactivation studies, the use of model systems was vital to achieve the presented fundamental insight into these catalyst deactivation mechanisms. For the study on sintering, the planar support combined with TEM provided direct evidence for atomic migration (Ostwald ripening), rather than particle migration and coalescence, as the dominant mechanism when cobalt crystallites are exposed to FTS conditions. This enabled a proposal for the design of future catalysts such that sintering and consequently catalyst

deactivation can be reduced. For the case of carbon deposition, the characterization of model systems, containing the support or the metal surface in isolation, was combined with findings from catalyst testing under relevant conditions. This led to the conclusions that carboxylic acids are precursors for atomic rather polymeric carbon and do not significantly contribute to Co FTS catalyst deactivation.

6.6. References

- [1] A. M. Saib, D. J. Moodley, I. M. Ciobîcă, M. M. Hauman, B. H. Sigwebela, C. J. Weststrate, J. W. Niemantsverdriet, J. van de Loosdrecht, *Catal. Today* 154 (2010) 271–282.
- [2] A. Y. Khodakov, W. Chu, P. Fongarland, *Chem. Rev.* 107 (2007) 1692–1744.
- [3] N. E. Tsakoumis, M. Rønning, Ø. Borg, E. Rytter, A. Holmen, *Catal. Today*, 154 (2010) 162-182.
- [4] J. van de Loosdrecht, B. Balzhinimaev, J. -A. Dalmon, J. W. Niemantsverdriet, S. V. Tsybulya, A. M. Saib, P. J. van Berge, J. L. Visagie, *Catal. Today* 123 (2007) 293-302.
- [5] P. C. Thüne, J. W. Niemantsverdriet, *Surf. Sci.* 603 (2009) 1756–1762.
- [6] M. Sadeqzadeh, J. Hong, P. Fongarland, D. Curulla-Ferré, F. Luck, J. Bousquet, D. Schweich, A. Y. Khodakov, *Ind. Eng. Chem. Res.* 51 (2012) 11955-11964.
- [7] N. E. Tsakoumis, R. Dehghan-Niri, M. Rønning, J. C. Walmsley, Ø. Borg, E. Rytter, A. Holmen, *Appl. Catal. A* 479 (2014) 59-69.
- [8] G. L. Bezemer, J. H Bitter, H. P. C. E Kuipers, H. Oosterbeek, J. E Holewijn, X. Xu, F. Kapteijn, A. J. Van Dillen, , K. P. De Jong, *J. Am. Chem. Soc.* 128 (2006) 3956-3964.
- [9] C. J. Bertole, C. A. Mims, G. Kiss, *J. Catal.* 210 (2002) 84-96.

- [10] G. L. Bezemer, T. J. Remans, A. P. van Bavel, A. I. Dugulan, *J. Am. Chem. Soc.* 132 (2010) 8540-8541.
- [11] D. J. Moodley, A. M. Saib, J. van de Loosdrecht, C. A. Welker-Nieuwoudt, B. H. Sigwebela, J. W. Niemantsverdriet, *Catal. Today* 171 (2011) 192-200.
- [12] N. H. Chou, P. N. Ross, A. T. Bell, T. Don Tilley, *ChemSusChem* 4 (2011) 1566-1569.
- [13] D. J. Moodley, J. van de Loosdrecht, A. M. Saib, M. J. Overett, A. K. Datye, J. W. Niemantsverdriet, *Appl. Catal. A.* 354 (2009) 102-110.
- [14] L. Pinard, P. Bichon, A. Popov, J. L. Lemberon, C. Canaff, F. Mauge, P. Bazin, E. Falabella S. -Aguiar, P. Magnoux, *Appl. Catal. A: Gen.* 406 (2011) 73-80.
- [15] D. Pena, A. Griboval-Constant, C. Lancelot, M. Quijada, N. Visez, O. Stephan, V. Lecocq, F. Diehl, A. Y. Khodakov, *Catal. Today* 228 (2014) 65-76.

Summary

Fundamental understanding of cobalt Fischer-Tropsch synthesis catalyst deactivation

Co is the preferred metal for the gas-to-liquids process in large-scale commercial Fischer-Tropsch synthesis (FTS) plants. As is the challenge faced with many catalysts, the Co FTS catalyst deactivates with time on line. This is a significant problem since the economics of the gas-to-liquids process is strongly dependent on the stability of the catalyst. Understanding catalyst deactivation mechanisms is crucially important because the insight gained can be used to improve catalyst stability and inspire rational design of future catalysts.

There are a number of postulated deactivation mechanisms of Co FTS catalysts including (i) poisoning (which can be minimized by using a clean gas feed), (ii) oxidation (which can be prevented by tuning of particle size and reaction conditions), (iii) cobalt-support compound formation (which does not impact particle sizes optimum for FTS) and (iv) carbon-induced surface reconstruction (which requires a high carbon coverage that is not expected during FTS). This thesis provides fundamental understanding on specifically two deactivation mechanisms of Co FTS catalysts i.e. sintering and carbon formation.

Sintering is generally referred to as (thermally induced) catalyst deactivation caused by a loss of active metal surface area. The loss of catalyst active surface area is a result of loss and/or growth of the nanoparticles into which the active metal phase is dispersed. The principal mechanisms of sintering on supported catalysts are (i) particle migration and coalescence and (ii) atomic migration also referred to as Ostwald ripening. To our knowledge, direct evidence of the sintering mechanism during Co FTS has not been reported in the literature

We use a planar Co/SiO₂ model catalyst to uncover the sintering mechanism at the single-particle level. The model catalyst is exposed to FTS conditions of pressure (20 bar_a), temperature (230°C) and gas atmosphere (dry H₂/CO, low conversion) using a custom-designed high pressure treatment cell. Loss of metal surface area is found to proceed *via* an atomic migration (Ostwald ripening) mechanism. TEM micrographs of the same area before and after FTS show (i) rapid loss (within 10h) of most smaller particles (≤ 4 nm Co metal), (ii) a decrease in size of some larger particles (size decreases from ~ 5 nm to 2nm) and (iii) all remaining particles are immobile during the reaction. Complementary x-ray photoelectron spectroscopy (XPS) analyses confirmed the loss of metal surface area after exposure to FTS conditions. Metal-support compound formation (excluded using *in-situ* XPS analyses) as well as the formation of volatile species (excluded using Rutherford backscattering data) were excluded as reasons for the measured loss of metal surface area. The mechanism of loss of metal surface area is deduced to proceed *via* a mobile cobalt-subcarbonyl species that is transported *via* diffusion over the support surface from the smaller to relatively larger particles. Longer FTS reaction times (> 10h) are deduced to affect relatively larger particle sizes, which are optimum for FTS

Summary

activity, *via* Ostwald ripening. Therefore, atomic migration of cobalt could contribute to catalyst deactivation during Co-catalyzed FTS.

Our findings suggest that loss of metal surface area can be reduced by lowering the driving force for sintering and slowing down the diffusion of mobile Co species. One method can be to prepare fresh catalyst particles with a highly uniform particle size distribution (ideally with the optimal size for target FTS performance). Loss of metal surface area could also be slowed down by maximizing the inter-particle distances during the catalyst preparation step.

Polymeric carbon deposited on Co FTS catalyst can negatively impact FTS activity. Carbon on spent Co/Al₂O₃ FTS catalyst has been found to contain oxygenated compounds such as alcohols and carboxylic acids. Oxygenated compounds could therefore be potential precursors for carbon deposited on Co FTS catalyst. This carbon could be a result of oxygenate decomposition over the metal or support surface. Oxygenates could also be strongly adsorbed on Al₂O₃ support or form metal-carboxylate compounds and consequently affect Co FTS catalyst performance.

We studied the impact of FTS-produced carboxylic acids on catalyst deactivation. Thermal decomposition of acetic acid over reduced Co/Pt/Al₂O₃ catalyst, at model FTS conditions (i.e. 1 bar_(a) H₂/CO:2/1 at 230°C), deposits predominantly atomic carbon on the catalyst (determined using temperature-programmed hydrogenation coupled with mass spectrometry (TPH-MS)). Adsorbed oxygenates detected on spent Co/Pt/γ-Al₂O₃ FTS catalyst are deduced to be located on the γ-Al₂O₃ support. Both short (acetate) and longer chain (octanoate) carboxylates are chemisorbed on pure γ-Al₂O₃ and are thermally stable at Co FTS

temperature under synthesis gas (determined using infrared (IR) spectroscopy and XPS analyses). Co-feeding of excess acetic acid, to either fresh or spent catalyst, during FTS in continuous stirred tank reactor (CSTR) at relevant reaction conditions (20 bar_(a) H₂/CO:2/1 at 230°C), did not enhance Co/Pt/ γ -Al₂O₃ catalyst deactivation.

On the basis of findings in this thesis, carboxylic acid decomposition is excluded as a source of polymeric carbon during Co-catalyzed FTS. Acetic acid decomposition over the metal surface is found to produce predominantly atomic carbon. Compared to polymeric carbon, atomic carbon can be more readily hydrogenated at FTS temperature. Therefore, the contribution of carboxylate decomposition to FTS catalyst deactivation is expected to be limited (dependent on operating conditions as high concentrations of acids could possibly result in more severe carbon deposition).

The finding that oxygenates are chemisorbed on γ -Al₂O₃ support suggests that the support is essentially modified during FTS. For instance, octanoic acid adsorbed on γ -Al₂O₃ changes the support surface from hydrophilic to hydrophobic. Consequently, the local water partial pressure as 'seen' by the Co particle could decrease due to carboxylate adsorption during FTS. The increased hydrophobicity may also induce effects on the diffusion of FTS products into and out of support pores. Hydrocarbons could experience longer residence times in support pores, since they would have an affinity toward a hydrophobic environment. This build-up of hydrocarbons could then lead to pore blocking, induce product or reactant gas diffusion limitations and in this way impact FTS performance. Future experiments to test these hypotheses include (i) impregnating the catalyst with long chain carboxylates (e.g. octanoic acid) then observing the impact

Summary

on FTS performance and (ii) co-feeding long chain carboxylates during FTS.

Quantum chemistry can be used to study a number of chemical and molecular systems in order to make predictions on the equilibrium structures of molecules, transition states and reaction pathways. Specifically, Density Functional Theory (DFT) provides the solution to fundamental equations that describe the quantum behavior of atoms and molecules.

Since carboxylate compounds were found to be chemisorbed on pure $\gamma\text{-Al}_2\text{O}_3$ and thermally stable at Co FTS temperature, the reason for the strong adsorption was studied using DFT. Carboxylate molecules were envisaged to strongly interact, *via* the nucleophilic carboxylate (COO^-) group, with aluminum cations (Al^{3+}) on the $\gamma\text{-Al}_2\text{O}_3$ surface.

We use DFT to describe the interaction between acetic acid and two representative alumina surfaces i.e. the $\gamma\text{-Al}_2\text{O}_3$ (100) and (110) surfaces. Vibrational frequencies determined using DFT calculations are compared to those measured using IR. The most stable chemisorption structure of acetic acid on the $\gamma\text{-Al}_2\text{O}_3$ surface is found to be dissociative (i.e. an acetate species is formed *via* coordination of both oxygen atoms of the acid to two aluminum ions on the support). These chemisorption structures correspond to high adsorption energies and significantly long surface residence times for an adsorbed acetic acid molecule. These findings suggest that carboxylates are practically irreversibly adsorbed on $\gamma\text{-Al}_2\text{O}_3$ support. Theoretical and experimental findings (thermogravimetric analyses (TGA) data) imply that acetic acid chemisorbs on a hydrated $\gamma\text{-Al}_2\text{O}_3$ surface, which is the expected state of the surface during FTS. The strength of

adsorption of a carboxylate and the long residence time of an acid molecule on the γ -Al₂O₃ surface, explains why oxygenated compounds are detected on spent Co FTS catalyst using IR (i.e. both 5 and 90 day old spent samples).

Finally, we have summarized some important results in future research (described in Chapter 6). The major conclusions for this thesis are that (i) Ostwald ripening of cobalt nanoparticles is the dominant mechanism of loss of metal surface area when the planar Co/SiO₂ model catalyst is exposed to low-conversion FTS conditions, (ii) acetic acid is strongly adsorbed *via* dissociative adsorption on two representative γ -Al₂O₃ surfaces (i.e. the (100) and (110) surfaces), forming an acetate species and (iii) carboxylic acids cause atomic carbon formation on Co/ γ -Al₂O₃ FTS catalyst and result in strongly adsorbed carboxylates on γ -Al₂O₃ support, but these factors do not significantly impact catalyst deactivation.

Acknowledgments

Finally, I have arrived at the conclusion of the PhD thesis. Supervisors, colleagues, friends and family have all, in one way or another, contributed to making this possible. Thank you, sincerely, to all of you.

To my promotor, Hans, thank you for the support, guidance, and all round first class advice throughout my PhD time. You always encouraged personal and scientific improvement and I will take away important personal and work values from the example that you set. I feel honored to have graduated as a scientist from your research group. All the best with your new company in the future.

To my supervisor, Kees-Jan, I am indebted to you for your support during my PhD time. I am proud to see the application of my ideas in my work and this is because you encouraged me to explore my potential. I did this while also developing as a scientist through our critical discussions. Working with you was a privilege, and I share the successful completion of this PhD with you.

To our TU/e research group principal technician, Tiny, thank you for assisting in building the experimental set-ups used in my project. I learned a great deal of technical skill from you and you always provided much appreciated encouragement in conducting experiments.

To my project advisor and Sasol work colleague, Ionel, thank you for your time and effort in our DFT study. Thank you also for providing me with workspace in the Sasol office, where we had many valuable discussions about work and enjoyable talks about life in general. Thank you to my work colleague Werner, I am grateful to you for sharing your expertise on the DFT project and for the continuous support.

To my previous Sasol research group leader, Abdool, thank you for your support. You were instrumental in me joining Sasol, you then oversaw my development as a scientist, and then showed confidence in me by enabling my secondment to TU/e. I am grateful for your support when Rowena moved to Eindhoven. I was driven during my PhD as my objective was always to do a great job for both our benefit.

Thanks to Denzil for your support in my secondment and settling back into life in South Africa. Thanks to Philip and Jan for your support in the last few months while I was completing the thesis in South Africa and for all the IP advice.

Acknowledgments

Thanks to my TU/e research group members Jasper, Gilbère, Başar, Ali, Hans.F & Huapeng for enjoyable interactions inside and outside the laboratory. Remco, thanks for your assistance with 'our' reactor set-up. Oluş, thanks for your collaboration on the DFT work. Zhenghang, thanks for the breaks to go out to celebrate the important dates. Yibin, thanks for the talks about doing our best in our work and wish you the best for your project. Ajin, thank you for generously allowing me to use your IR set-up, giving valuable PhD advice and I will always remember our trip to Barca. Emad, we started PhD in the same week, worked in the same office and lived for three years in the same building. Thank you for your friendship and I look forward to good trips in the future. Thanks to Peng and Michel for the use of the TP-MS set-up. Thanks to Paul for his assistance with the TEM set-up.

Thank you, Therese-Anne and Susan, for assisting in getting me settled into academic life in Eindhoven, and to José and Agnes for assistance over the last year of my PhD. Thank you to my Sasol international HR consultant, Ruth, for her support & encouragement during my PhD time and in my relocation to and from Eindhoven.

I would gratefully like to acknowledge members of my defense committee – prof.dr. J.W. Niemantsverdriet, dr C.J. Weststrate, prof.dr. A.K. Datye, prof.dr. A.O.I. Krause, prof.dr.ir. E.J.M. Hensen, dr. J. van de Loosdrecht and prof.dr.ir. J.C. Schouten for kindly accepting our invitation and taking the time to evaluate the Ph.D thesis.

Thank you to my family and friends who have continued to support me. Thanks to Mokgolela, Nishlan and Terence for all your help in making sure things were ok back in South Africa. Thanks to my aunts, uncles and cousins for always being there for me. Thanks to my parents Rani and Peggie and sister, Dashnee for your undying support and for being a motivation to succeed, not only during this PhD time, but also throughout my life. This would all not be possible without your support. To my wife, Rowena, I will be forever grateful for your support and for always being the person I can count on, thank you for being the rock that I needed to complete this PhD.

Deshen

Sasolburg, South Africa, 2015

List of publications

Journal publications

- D. Kistamurthy, A.M. Saib, D.J. Moodley, J.W. Niemantsverdriet, C.J. Weststrate, *Ostwald ripening on a planar Co/SiO₂ catalyst exposed to model Fischer-Tropsch synthesis conditions*, J.Catal, accepted.

Oral presentations at conferences

- D. Kistamurthy, C. J. Weststrate, J. W. Niemantsverdriet, A. M. Saib, D. J. Moodley, *Cobalt sintering at Fischer-Tropsch synthesis conditions*, Netherlands Catalysis & Chemistry Conference XV, Noordwijkerhout, The Netherlands, March 10-12, 2014.
- D. Kistamurthy, C. J. Weststrate, J. W. Niemantsverdriet, A. M. Saib, D. J. Moodley, *Cobalt sintering at Fischer-Tropsch synthesis conditions*, Catalysis Society of South Africa Conference, Johannesburg, South Africa, November 10-12, 2014.

Poster presentations at conferences

- D. Kistamurthy, C. J. Weststrate, J. W. Niemantsverdriet, A. M. Saib, D. J. Moodley, *Cobalt sintering at Fischer-Tropsch synthesis conditions*, Netherlands Catalysis & Chemistry Conference XIV, Noordwijkerhout, The Netherlands, March 11-13, 2013.

List of publications

- D. Kistamurthy, C. J. Weststrate, J. W. Niemantsverdriet, A. M. Saib, D. J. Moodley, *Cobalt sintering at Fischer-Tropsch synthesis conditions*, Faraday Discussion 162, Fabrication, Structure and Reactivity of Anchored Nanoparticles, Berlin, Germany, April 10-12, 2013.
- D. Kistamurthy, C. J. Weststrate, J. W. Niemantsverdriet, A. M. Saib, D. J. Moodley, *Cobalt sintering at Fischer-Tropsch synthesis conditions*, European Graduate Summerschool, Rolduc abbey, The Netherlands, June 23-26, 2013.
- D. Kistamurthy, C. J. Weststrate, J. W. Niemantsverdriet, A. M. Saib, D. J. Moodley, *Cobalt sintering at Fischer-Tropsch synthesis conditions*, SUNCAT Center for Interface Science and Catalysis Summerschool, California, United States of America, August 25-30, 2013.

Curriculum vitae

Deshen Kistamurthy was born on 31st December 1984, in Durban, South Africa. He received academic scholarship to attend Grosvenor boys high school in Durban and later relocated to East London, South Africa where he matriculated with distinction from Selborne College in 2002.

He received academic scholarship to study at the University of Cape Town, South Africa, where he graduated with a Bachelor of Science degree Honours with distinction in 2007. He received a bursary from Sasol, South Africa and graduated with a Master of Science degree (Chemistry), in the field of platinum-catalyzed hydroformylation, in 2009. He joined Sasol Technology, South Africa in 2010 and was employed in the research and development of cobalt-catalyzed Fischer-Tropsch synthesis. He was seconded to Technische Universiteit Eindhoven, The Netherlands in 2011, where he commenced his Ph.D degree under the supervision of prof. dr. J.W. Niemantsverdriet and dr C.J. Weststrate at the Laboratory for Physical Chemistry of Surfaces research group. His Ph.D topic was 'Fundamental understanding of cobalt Fischer-Tropsch synthesis catalyst deactivation' of which the most relevant findings are described in this thesis.